

Color Transparency of Nuclear Matter
to Hard Scattered Hadrons
and the Nucleon Spectral Functions

A Thesis

*Submitted to the Faculty of the Graduate School
of the University of Minnesota*

by

Guang Yin Fang

*In Partial Fulfillment of the Requirements
for the Degree of
Doctor of Philosophy*

April 1989

21876

© Guang Yin Fang 1989

FERMILAB
LIBRARY

TABLE OF CONTENTS

LIST OF FIGURES	iii
LIST OF TABLES	v
ACKNOWLEDGEMENTS	vi
ABSTRACT	vii
Chapter 1 INTRODUCTION	1
Chapter 2 REVIEW OF THEORIES ON EXCLUSIVE INTERACTIONS	11
2.1 The small hadron model	13
2.2 The large hadron model	23
2.3 The phenomenological models and the experimental status of exclusive interactions	30
2.4 Nuclear transparency to hard scattered hadrons	37
2.5 Fermi motion of nucleons inside a nucleus and its effects	41
Chapter 3 THE APPARATUS	46
3.1 Beam line	48
3.2 Target assembly	51
3.3 Beam Cherenkov counters	55
3.4 Spectrometer	61
3.5 Trigger	67
3.6 Data acquisition	72
3.6.1 PWC data acquisition	72
3.6.2 DWC data acquisition	74
Chapter 4 THE DATA ANALYSIS	75
4.1 TDC calibration and alignment	77
4.2 Event reconstruction	83
4.2.1 Spectrometer reconstruction	86
4.2.2 Side arm reconstruction	92
4.3 Particle identification	93
4.3.1 Beam identification	93
4.3.2 Spectrometer particle identification	96
4.4 Event identification	97
Chapter 5 THE RESULTS AND DISCUSSIONS	104
5.1 Proton transparency	106
5.1.1 General description	106
5.1.2 Energy dependence of the proton transparency and its interpretations	125
5.1.3 A dependence of the proton transparency	135
5.1.4 Errors and uncertainties on proton transparency	143
5.2 Pion transparency	153
5.3 Nucleon spectral functions	158

FINAL COMMENTS	168	
APPENDICES	171	
A.1	Perturbation theory in the infinite momentum frame	171
A.2	Monte Carlo simulations	178
A.2.1	Cross section simulation	178
A.2.2	Simulation of the background process $pp \rightarrow p\Delta$	181
A.2.3	Simulation of the absorption by the nuclear matter	182
BIBLIOGRAPHY	186	

LIST OF FIGURES

- 1.1 Cross sections for some sample exclusive interactions
- 1.2 Cross section for $pp \rightarrow pp$

- 2.1 Factorization of a pp scattering process
- 2.2 Born diagrams for the hard scattering sub-process in $pp \rightarrow pp$
- 2.3 Schematic view of the shrinking of a hadron that participates a hard scattering process
- 2.4 The two constituent system
- 2.5 Landshoff picture for a $\pi\pi$ scattering
- 2.6 Sample Sudakov suppression diagrams
- 2.7 Comparison between the theory and the data on pion form factor
- 2.8 Comparison between the theory and the data on proton form factor
- 2.9 Cross sections for two photon processes
- 2.10 pp cross section as a function of s after factorizing out the power law factor
- 2.11 Asymmetry for the polarized proton scattering
- 2.12 Sample momentum spectrum measured by low energy electron quasi elastic scattering
- 2.13 Fermi momentum as a function of A

- 3.1 The beam line
- 3.2 The beam momentum dispersion
- 3.3 Schematic view of the target assembly
- 3.4 Schematic view of a ring image of the Cherenkov light focused by a spherical mirror
- 3.5 Calibration curve for CDR1 and CDR2 at 6 Gev
- 3.6 Calibration curve for CDR3 and CDR4 at 6 Gev
- 3.7 Plan view of the detector
- 3.8 Resolution of a typical drift plane in the spectrometer
- 3.9 Schematic of the hodoscope trigger matrix
- 3.10 The trigger logic

- 4.1 Sample TDC plot
- 4.2 The vertex distribution of the elastic events
- 4.3 The track fitting schematic
- 4.4 P_{fy} distribution of the quasi elastic events from Al target at 6 Gev
- 4.5 P_{fz} distribution of the elastic events from the polyethylene target

- 5.1 The Moniz distribution
- 5.2 Monte Carlo generated Moniz distribution comparing with the data
- 5.3 Proton transparency as a function of the effective energy for the aluminum target

- 5.4 Proton transparency as a function of the effective energy for the carbon target
- 5.5 Proton transparency as a function of the incident energy for all targets
- 5.6 Comparison between the Ralston model prediction and the data
- 5.7 A dependence of the proton transparency
- 5.8 Schematic view of the off-shell scattering
- 5.9 Schematic view of the scattering off protons from different energy levels
- 5.10 The simulated inclusive decay of $pp \rightarrow p\Delta$
- 5.11 p_{fz} distribution for the pion scattering events off the aluminum target at 6 Gev
- 5.12 Pion transparency as a function of the incident energy.
- 5.13 The spectral function for lithium
- 5.14 The spectral function for carbon
- 5.15 The spectral function for aluminum
- 5.16 The spectral function for copper
- 5.17 The spectral function for lead

LIST OF TABLES

- 3.1 Parameters of the target segments
- 3.2 Parameters of the Cherenkov counters
- 3.3 The chamber parameters
- 4.1 The pre-selection cuts
- 4.2 The truth table of the beam identification
- 5.1 Event distribution for pp scattering off Al target at 6 Gev
- 5.2 Event distribution for pp scattering off Al target at 10 Gev
- 5.3 Event distribution for pp scattering off Al target at 12 Gev
- 5.4 Event distribution for pp scattering off C target at 6 Gev
- 5.5 Event distribution for pp scattering off C target at 10 Gev
- 5.6 Event distribution for pp scattering off C target at 12 Gev
- 5.7 Number of pp events within the central region for all targets at 6 Gev
- 5.8 Number of pp events within the central region for all targets at 10 Gev
- 5.9 Number of pp events within the central region for Al and C targets at 12 Gev
- 5.10 Number of πp events within the central region for all Targets at 6 Gev
- 5.11 Number of πp events within the central region for all targets at 10 Gev

Acknowledgements

Many people contributed towards the completion of E834. D. S. Barton, G. M. Bunce, A. C. Carroll, S. Gushue and Y. I. Makdisi from Brookhaven National Laboratory; J. J. Russel from Southeastern Massachusetts University; H. Courant, K Heller, M. L. Marshak from University of Minnesota, S. Heppelman from Pen State University and M. Shupe from University of Arizona were collaborators on E834. I would like to thank all of them for their help and contributions. I would also like to thank the AGS staff and Minnesota technical staff for their help with the experiment.

I would especially like to express my gratitude to my advisor Marvin Marshak for his guidance and support during my whole graduate career at Minnesota. I have enjoyed many instructive and helpful discussions with A. Carroll, K. Heller and S. Heppelman. It has been great pleasure to study and work at Minnesota.

Finally I would like to thank my wife, Xiuhua Zhou, whose encouragement and patience play important part in the completion of this thesis.

Abstract

The cross sections for fixed wide angle exclusive interactions have been known to scale. Namely, the energy dependence of the cross sections can be obtained simply by counting the total number of valence quarks in the initial and the final state particles. The model of S. Brodsky and G. Farrar predicts this scaling behavior by assuming that the scattering hadrons shrink to anomalously small configurations at the point of interaction, while that of V. Landshoff accounts for the scaling by assuming that the interaction goes through large distance, independent constituent collisions. One way of differentiating between the two models is by measuring hadron nucleon scattering cross sections off nuclear targets: if the hadrons are indeed small, as assumed by the small hadron model, there must be some time interval before and after the interaction in which the hadrons remain small. During this period the color fields surrounding the hadrons should be weaker than those in the interior of a normal hadron. Thus, the interactions between these hadrons and the medium should be weaker. This means that the quasi elastic scattering cross section between a hadron and a proton from the nucleus at high momentum transfer should be higher than what has been observed at low energies, and should increase with energy. To test these hypotheses, an experimental program was carried out at Brookhaven National Laboratory, Long Island, New York, in which pp and πp quasi elastic scattering cross sections off lithium, carbon, aluminum, copper and lead, and off hydrogen were observed simultaneously at beam energies of 6 and 10 Gev. In

addition scattering was also observed for carbon and aluminum targets at 12 Gev. The detector consisted of a single arm spectrometer supplemented by an array of wire chambers to determine the directions of the recoil particles. The transparency, defined as the ratio of the hadron proton scattering cross section off the nuclear target to that off the hydrogen target was determined. The results supported the idea of transparency quite well in going from 6 to 10 Gev. However a sudden drop in the transparency at 12 Gev was also seen, which could not be reconciled with the short distance scattering model. Ideas that account for the data well will be discussed. In addition the data will also be presented in the context of the nucleon spectral functions.

Chapter One Introduction

The cross sections for fixed wide angle exclusive interactions, interactions in which all the particles in the final state are detected ($A+B \rightarrow C+D$) have been known to scale at high energies:

$$\frac{d\sigma}{dt} \propto s^{-(n-2)} \quad (1.1)$$

where $n = \sum n_i$, n_i is the number of valence quarks in particle i and the sum runs over all the particles in the initial and the final states. Eq. 1.1 is one form, applicable in the exclusive interactions, of the more general scaling laws, known as the dimensional-counting or constituent-counting rules, discovered independently at about the same time by S. Brodsky and G. Farrar (Bro 1973, 1975), and by Matveev, Murdyan and Tavheldize (Mat 1973). A common feature of these rules is that in each process only minimum number of constituents needs to be counted.

The counting rules were derived based on some simple dimensional arguments: in a scale invariant interaction the only distance scale present is $(\sqrt{s})^{-1}$; if there are a total of n fields participating in the interaction, the Feynman amplitude M_n has a dimension of L^{n-4} when

the conventional normalization of states $\langle p|p' \rangle = 2E\delta^3(\mathbf{p}-\mathbf{p}')$ is used;

therefore M_n must be proportional to $(\sqrt{s})^{4-n}$. The dimensional-counting rules have been confirmed by rigorous Perturbative Quantum Chromodynamics (PQCD) calculations based on the assumptions that the scattering amplitude of an exclusive interaction that involves large momentum transfer between physical hadrons factorizes into a "hard" part, which describes the subprocess in which high momentum quanta are exchanged between the minimum constituent Fock states, and a "soft" part, referred to as short distance wave functions, which represents the probabilities that the physical hadrons containing such minimum constituents Fock states. The constituent scattering sub-processes are assumed calculable by the lowest order PQCD, and the wave functions are considered deducible from the large distance behavior of the hadrons.

Experimental support for the scaling laws has been seen in a variety of processes including hadronic, photonic, semi-leptonic and purely leptonic interactions. Fig. 1.1 and fig. 1.2 show some examples. It can be seen from the plots that at high energies the data agree fairly well with the scaling law predictions in all the processes plotted. Given the lack of our knowledge on the complicated nature of the confinement, a mechanism that is used to explain the fact that no free colored states have ever been observed in nature, and our lack of ability to calculate the binding processes by which the constituents form physical hadrons which are the ultimate objects we deal with experimentally, it is quite remarkable that such simple rules work so well at presently

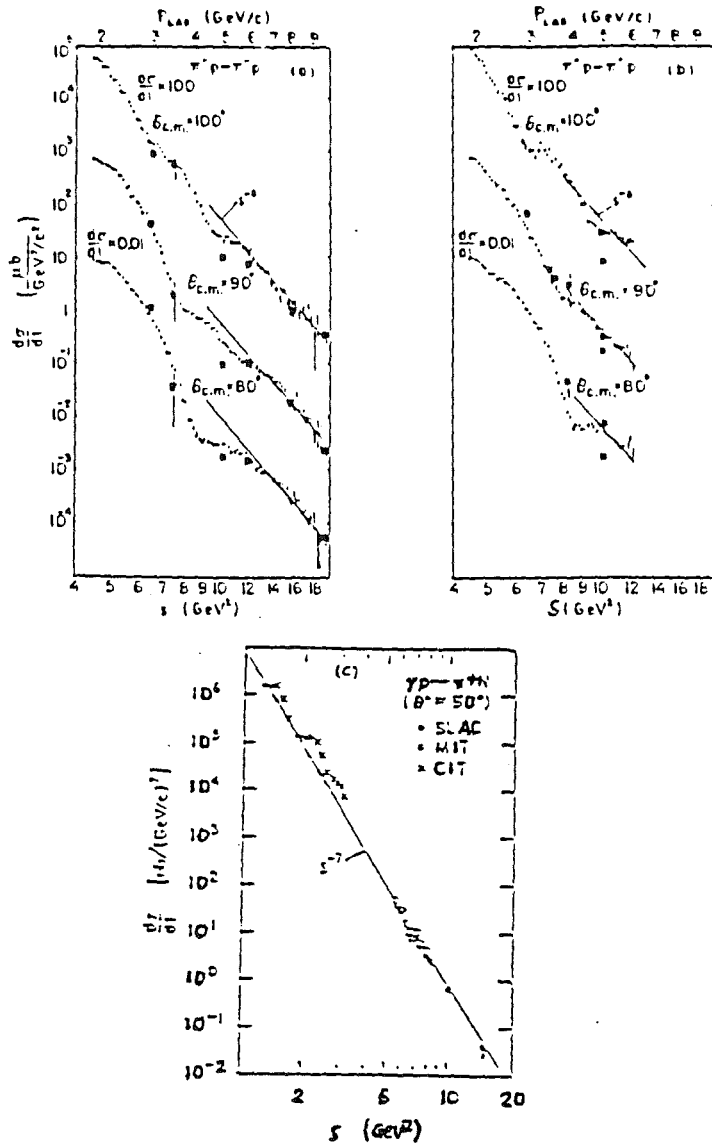


Fig. 1.1 Cross sections for some sample exclusive interactions that show scaling behavior. a) $\pi^- p \rightarrow \pi^- p$, b) $\pi^+ p \rightarrow \pi^+ p$ (Jen 1980), c) $\gamma p \rightarrow \pi p$ (Lep 1980).

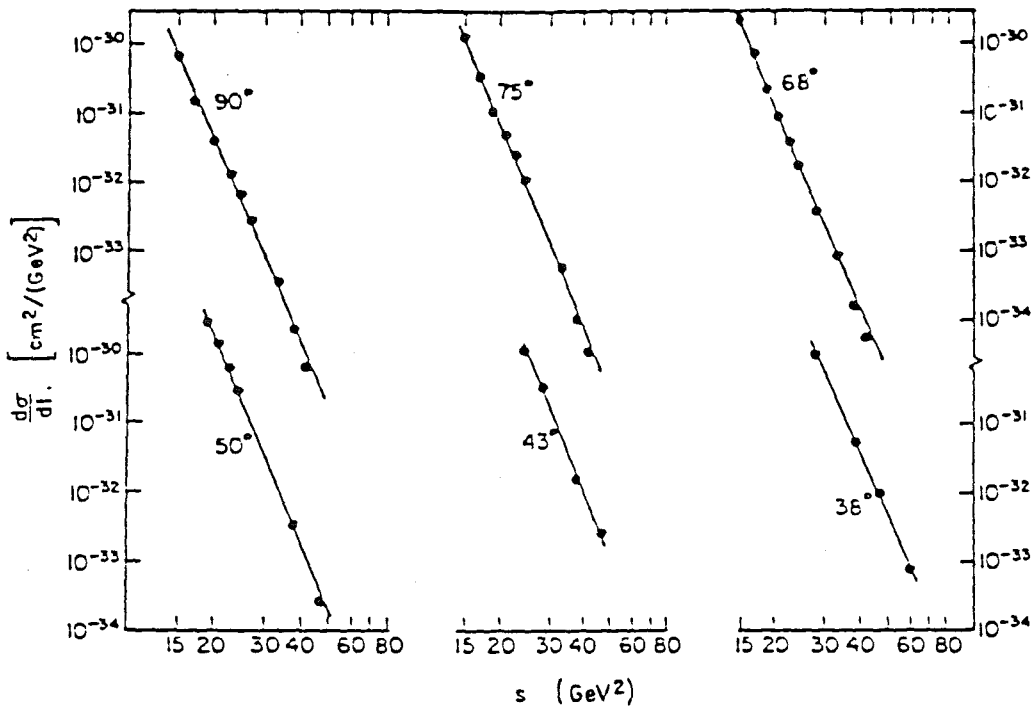


Fig. 1.2 Cross section for $pp \rightarrow pp$ (Lep 1980). The straight lines correspond to s^{-10} fall off.

reachable energies.

Despite the surprising successes of the counting rules, however, our understanding of exclusive interactions is still far from satisfactory. Areas in which theory and experiment can be compared with precision are very few, if any, mainly because the normalizations of exclusive interactions are not calculable and the separations of hard from soft contributions are questionable, to say the best. Isgur and Llewellyn

Smith (Isg 1984) have argued that at presently accessible Q^2 the non perturbative terms dominate in the pion electric form factor and the nucleon magnetic form factors. On the other hand, O. C. Jacob and L. S. Kisslinger (Jac 1986) have arrived at the conclusion that asymptotic terms begin to dominate at $Q^2 \approx 3.5 \text{ Gev}^2$ using a slightly modified procedure. Data on high energy exclusive interactions are scarce and, some times, ambiguous, because of the difficulties associated with the diminishing cross sections and uncertainties in interpreting the data. Existing data, though small in quantity, defies a unified treatment. In particular, data on polarized proton scattering and the decay angular distribution of ρ produced in $\pi p \rightarrow \rho p$ (Hep 1985) seem to indicate that non perturbative effects are not negligible. Thus, the lowest order PQCD treatments are inadequate. Predictions on the energy, angle and helicity distributions for exclusive interactions are largely phenomenological in nature. In addition to the obvious difficulties of having to handle the omnipresent infrared and confinement effects many issues concerning the validity of the theories remain to be resolved:

How well are the wave functions approximated by the minimum Fock states and how do the Fock states couple to the physical hadrons?

Can the masses of the constituents and the internal momenta of the hadrons be completely ignored at presently reachable energies?

Can the constituent scattering amplitudes be well approximated by the lowest order PQCD?

Most of all, are the asymptotic contributions dominant at presently accessible kinematic regions? If not, why are dimension counting rules apparently valid?

Comprehensive and systematic investigations on these issues were suggested (Far 1984). It was in this spirit that a series of experiments were carried out at Brookhaven National Laboratory (Bla 1985, Hep 1985, Bal 1988), in which a number of exclusive cross sections were measured and the decay angular distributions of ρ produced in $\pi p \rightarrow \rho p$ were observed. The present thesis will report a new set of measurements, in which quasi elastic pp and πp scattering off different nuclear targets at several incident energies were observed.

The pp elastic scattering cross sections, shown in fig. 1.2, follow approximately s^{-10} behavior, in agreement with what is predicted by the dimensional-counting rule. The question is what is the underlying mechanism that leads to such a behavior. There are at least two well known models that can account for this behavior almost equally well: the independent constituent scattering model due to Landshoff, and the short distance minimum Fock state scattering model proposed by Brodsky and Farrar. For convenience, hereafter the models will be simplistically referred to as the large and small hadron models respectively, echoing the fact that the hadrons at the point of interaction are considered "large" by the Landshoff model, and "small" in the Brodsky and Farrar model. In the small hadron model the

constituents are believed to be confined at the point of interaction to within a region that is much smaller in size than that of a normal hadron. The cross section is then simply that of a point like scattering modulated by the probabilities of finding the constituents of the initial and final state protons within that small region. The large hadron model, on the other hand, regards the scattering as proceeding through large distance, independent collisions between the constituents of the incoming protons. The scattering angles of the constituents are fine tuned so the final state protons can be formed out of these constituents. The cross section in this picture can be derived from simple phase space arguments.

It was noted by A. Muller (Mul 1982) that the small hadron picture implies the existence of the color transparency. The idea is very simple. If the scattering hadrons are indeed anomalously small at the collision point, as suggested by the small hadron model, there must be some time interval before and after the interaction, in which the hadrons remain small. During this time the color fields surrounding the constituents will be much weaker than those in the interior of a normal hadron. When put into nuclear matter these color neutral objects will experience much weaker absorptions than those felt by normal hadrons, and thus, will have much higher penetrating power. This means that the ratio of the quasi elastic scattering cross section between a hadron and a nucleon from the nucleus to the hydrogen cross section at high momentum transfer will be higher than what has been observed at low

energies. This enhancement in quasi elastic scattering cross section is called color transparency. According to Glauber picture, which has been very successful in explaining the data on low energy hadron nucleus interactions, hadrons entering the nucleus undergo series of interactions with the nuclear matter, rendering quasi elastic scattering likely only through collisions between the incoming hadrons and the nucleons on the surface of the nucleus. Thus, the number of quasi elastic events one sees will be very small, and the ratio of the quasi elastic cross section of hadron nucleon scattering to that of hadron hydrogen scattering, defined as the transparency, will be more or less energy independent for heavy nucleus because only the protons on the surface contribute and the number of surface protons for a given nucleus does not depend on energy. The situation is quite different in the case of small hadron scattering because now the color neutral objects can penetrate through the nuclear matter. The number of elastic events one can see in this case depends very much on the time scale involved in the expansion of the anomalously small objects. If the time it takes for the anomalously small hadrons to expand back to their normal sizes is much longer than that it takes for the particles to exit the nucleus one clearly should see more hard scattered hadrons exiting the nucleus without suffering further interactions. Thus the small hadron model predicts an energy dependent ratio of hadron nucleon cross section to hadron hydrogen cross section because the travel time

of the particle is dilated by the energy of the particle in the lab frame.

There is another piece of interesting physics that can be studied in these type of processes: the high momentum property of the nucleon spectral functions. At very high energies (where the transparency reaches the asymptotic value of 1) the observed quasi elastic pp scattering cross section can approximately be written as:

$$\left(\frac{d\sigma}{dt}\right)_o = \left(\frac{d\sigma}{dt}\right)_f f(p_f) \quad (1.2)$$

where $\left(\frac{d\sigma}{dt}\right)_f$ represents the free particle cross section and $f(p_f)$ is the momentum spectrum of the nuclear protons. Thus, measurements of the quasi elastic cross sections of hN scattering off nuclear targets provide direct measurements of the nuclear spectral functions. The nucleon spectral functions have been measured in low energy electron quasi elastic scattering experiments. The results could be explained fairly well by free Fermi gas model. However there is plenty of evidence that suggests the existence of a high momentum tail. In particular calculations based on nucleon correlations suggest that the tails should extend to at least a few Gev. Up to the present no quasi elastic electron scattering measurements have extended to the tail region because of their low energy nature. With high incident energies

we should be able to probe heretofore inaccessible kinematic regions of the momentum spectrum.

The experiment was carried out at Brookhaven National Laboratory with an existent single arm spectrometer supplemented by an array of wire chambers to measure the directions of the recoil particles. The data reported here include pp and πp scattering off lithium, carbon, aluminum, copper and lead targets at 6 and 10 Gev incident energies at center of mass frame (CMS) angles near 90 degrees. In addition pp scattering off carbon and aluminum at 12 Gev incident energy was also observed. Part of the data has been published (Car, 1988).

The thesis is organized as follows: after this brief introduction we will review some of the theoretical machinery that is related to the understanding of the experiment and the interpretation of the results. A brief description of the apparatus and the concerns for the experiment constitute the next chapter, followed by a description on the data analysis procedures. The next chapter will be devoted to the presentation of the results and discussions. Some final comments on the experiment conclude the thesis.

Chapter two Review of theories on exclusive interactions

In this part we will review some of the theories and models on exclusive interactions. In particular the model of Brodsky and Farrar, and that of Landshoff will be outlined. The idea of color transparency and its manifestations in high energy quasi elastic hadron nucleus scattering processes will be discussed. For completeness a very brief summary of the phenomenological models which were successful, one way or another, in explaining the data on exclusive interaction will be included. A brief discussion on the effects of the internal motion of the protons inside the nucleus will also be given.

Quantum Chromodynamics (QCD) is now widely accepted as the theory that describes the strong interactions among quarks and gluons, which are responsible for the composition of hadrons, as well as hadronic reactions. Through intensive experimental effort over the past two decades an impressive amounts of data including, scaling and scaling violations in deep inelastic lepton scattering, inclusive hadronic annihilation cross sections in e^+e^- collisions, jet cross sections in pp and $p\bar{p}$ collisions, heavy flavor particle life times and the Drell Yan processes. All of these phenomena give solid support to QCD. However almost all of the reliable tests have been from inclusive interactions. Tests of QCD on exclusive processes have been far less accurate and less conclusive. The calculating power of QCD for exclusive

interactions is very limited. One of the difficulties is that high incident energy alone is not sufficient to warrant the use of perturbative expansions. In order for a process to be completely calculable, the interactions involved must be all at high energies. This is not true in most cases in exclusive interactions because of the low energy nature of the interactions related to binding and confinement which play far more important roles in exclusive interactions than in inclusive interactions. Thus, the question of when or under what circumstances perturbative QCD is applicable in exclusive processes is more complicated than one might think, for, even when the momentum exchanges among the physical particles are large, there could still be sub-processes in which the dominant interactions are soft, and thus, non calculable. In addition, the diminishing cross sections make high energy exclusive interaction experiments much more difficult to pursue. Nevertheless, exclusive interactions may provide us some of the most detailed information on the structure of the theory, because these processes always depend in detail on the properties of the interacting systems, in particular, the wave functions of the hadrons.

2.1 The small hadron model in large momentum transfer exclusive interactions (Bro 1980)

In the light cone quantization (A brief description on the light cone quantization will be given in Appendix 1) a composite system of quarks and gluons can be described by an infinite row Fock space vector. For example, a proton can be represented by

$$|p\rangle = \begin{pmatrix} |qqq\rangle \\ |qqqg\rangle \\ |qqq\bar{q}\rangle \\ |qqqgg\rangle \\ \dots \end{pmatrix}$$

and a pion by

$$|\pi\rangle = \begin{pmatrix} |q\bar{q}\rangle \\ |q\bar{q}g\rangle \\ |q\bar{q}q\bar{q}\rangle \\ |q\bar{q}gg\rangle \\ \dots \end{pmatrix}$$

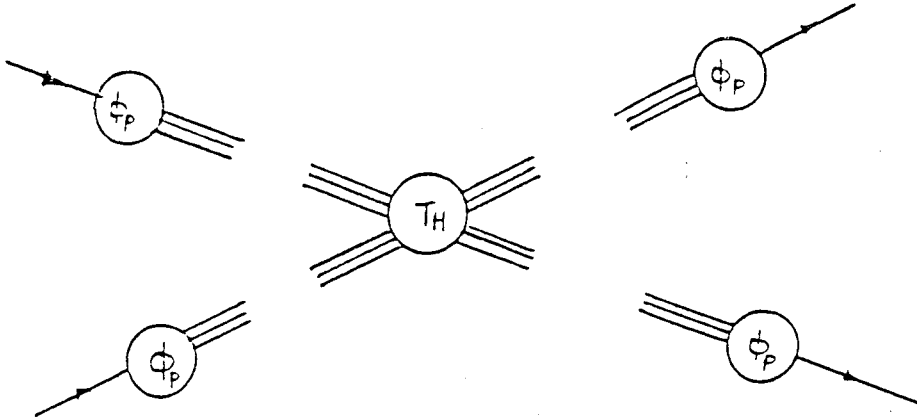


Fig. 2.1 Factorization of a pp scattering process where T_H represents the hard sub-process amplitude and the ϕ 's are the wave functions of the initial and final state protons.

The small hadron model for large momentum transfer exclusive interactions hinges on the ansatz that the transition amplitude factorizes into hard and soft parts, as shown schematically in fig. 2.1:

$$M(AB \rightarrow CD) = \int_0^1 \prod_{i=a,b,c,d} [dx_i] \phi_C^*(x_c, \vec{p}_\perp) \phi_D^*(x_d, \vec{p}_\perp) T_H(x_i, s, \theta_{c.m.}) \phi_A(x_a, \vec{p}_\perp) \phi_B(x_b, \vec{p}_\perp) \quad (2.1)$$

where $T_H(x_i, s, \theta_{c.m.})$ is the hard scattering amplitude between the minimum valence quark states and can be calculated perturbatively. ϕ_i 's are the initial and final state quark distribution functions which represent the probability amplitudes that the longitudinal momenta of the initial and the final state protons are partitioned as given by these x 's and all the quarks moving collinearly up to a scale Q^2 . To the lowest order T_H is the sum of all connected tree diagrams as shown in fig. 2.2 .

The contribution from these tree diagrams is of the form:

$$T_H(x_i, s, \theta_{c.m.}) = \left(\frac{\alpha_s(p_\perp^2)}{\sqrt{s}} \right)^{n-4} f(\theta_{c.m.}) \quad (2.2)$$

and the one loop corrections are suppressed by a factor of α_s .

The wave function ϕ can be calculated by solving the Bethe Salpeter equation and obtaining the evolution equation. To the leading order, $\phi(x_i, Q)$ can be written as:

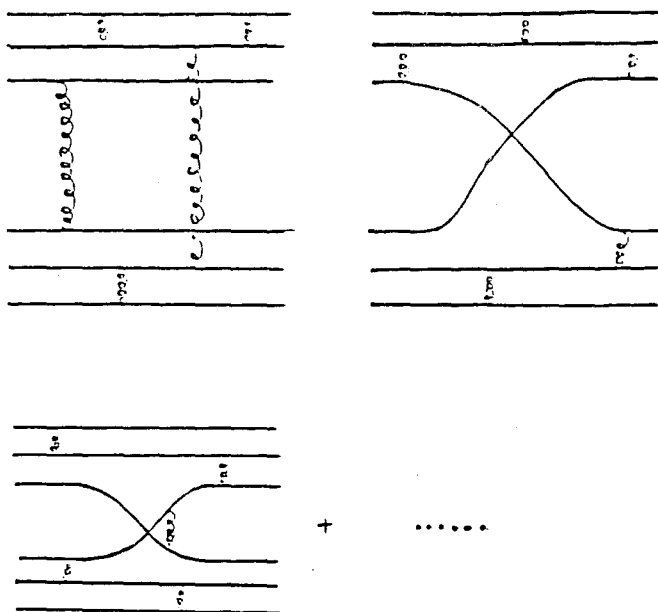


Fig. 2.2 Born diagrams for the hard scattering sub-process.

$$\phi(x_i, Q) = \int^Q \prod_{i=1}^3 d^2 k_{i\perp} \delta^2(\sum \vec{k}_{i\perp}) \psi(x_i, \vec{k}_\perp) \quad (2.3)$$

Differentiate both sides with respect to Q^2 and let

$$\xi = \ln \ln(Q^2/\Lambda^2)$$

$$\phi = x_1 x_2 x_3 \bar{\phi}$$

we get the following evolution equation:

$$x_1 x_2 x_3 \left[\frac{\partial}{\partial \xi} \bar{\phi}(x_i, Q) + \frac{3}{2} \frac{C_F}{\beta} \bar{\phi}(x_i, Q) \right] = \frac{C_F}{\beta} \int_0^1 [dy] V(x_i, y_i) \bar{\phi}(y_i, Q) \quad (2.4)$$

where

$$V(x_i, y_j) = 2x_1 x_2 x_3 \sum_{i \neq j} \theta(y_i - x_i) \delta(x_j - y_j) \frac{y_j}{x_j} \left(\frac{\delta_{h_i, h_j}}{x_i + x_j} + \frac{\Delta}{y_i - x_i} \right)$$

and,

$$C_F = 4/3$$

$$C_B = 2/3$$

$$\Delta = \bar{U}(y_i, Q) - \bar{\phi}(x_i, Q)$$

The solution to the evolution equation is of the form:

$$\phi(x_i, Q) = x_1 x_2 x_3 \sum_{n=0}^{\infty} a_n \left(\ln \frac{Q^2}{\Lambda^2} \right)^{\gamma_n} \phi_n(x_i) \quad (2.5)$$

$$\int \left(\ln \frac{Q^2}{\Lambda^2} \right)^{-2/3\beta} |h| = \frac{1}{2}$$

$$\rightarrow C x_1 x_2 x_3 |$$

$$\int \left(\ln \frac{Q^2}{\Lambda^2} \right)^{-2/\beta} |h| = \frac{3}{2}$$

where h is the helicity of the hadron.

The physical picture that embedded in this description is the following: a hard scattering process with a momentum transfer of q^2 between two hadrons can only occur when the the hadrons shrink to unusually small configurations, called the minimum Fock states, which consist of only the minimum number of constituents that confined to a region with size of the order of $(-q^2)^{-2}$. The distribution functions represent the probability amplitudes that the hadrons contain such configurations, and T_H is the scattering amplitude between these anomalously small objects. This picture is schematically drawn in fig. 2.3. A normal hadron contains various soft sea quarks and gluons. However, due to statistical fluctuations, the valence quarks come close to each other at some times. During this shrinking process, the soft constituents are absorbed, leaving only those with a momentum larger than Q . The power law can easily be derived from qualitative arguments based on such a picture. Consider a two constituent system, the probability for the two constituents staying together can be expressed

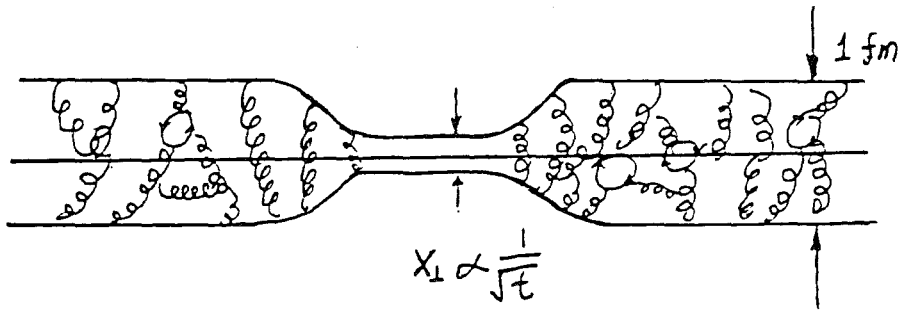


Fig. 2.3 Schematic view of the shrinking of a hadron that participates a hard scattering process.

in terms of two time scales: the time scale that the system stays in normal size τ_0 and the time the system is in the anomalously small configuration τ_Q . From the uncertainty principle, we have roughly: (see fig. 2.4)

$$\tau_0 \approx \frac{2p_+}{\mu^2}, \quad (2.6)$$

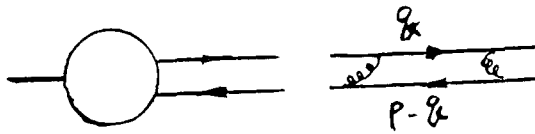


Fig. 2.4 The two constituent system.

$$\begin{aligned}
 \tau_q^{-1} &= -E + E_{p-q} + E_q \\
 &= -\frac{m^2}{2p_+} + \frac{q_+^2}{2(p-q)_+} + \frac{q_+^2}{2q_+} \\
 &= \frac{q_\perp^2}{2p_+} \left(\frac{m^2}{2} + \frac{1}{1-x} + \frac{1}{x} \right) \quad (2.7)
 \end{aligned}$$

when q_\perp is large enough the first term can be neglected. Then we have:

$$r_{q_{\perp}}^{-1} = \frac{q_{\perp}}{2p_{+}} \frac{1}{x(1-x)} \quad (2.8)$$

i.e.,

$$r_{q_{\perp}} = x(1-x) \frac{2p_{+}}{2} \quad (2.9)$$

where p_{+} is the momentum of the two constituent system in the infinite momentum system and m is its mass. $x=q_{+}/p_{+}$ is the fraction of the

longitudinal momentum carried by one of the constituents. So we arrive at the conclusion that the probability of the two constituent system in

the shrunken region $x_{\perp} \rightarrow (q_{\perp})^{-1}$ is simply $r_{q_{\perp}}/r_0 = \frac{\mu^2}{q_{\perp}^2}$.

The probability for a three constituent system to be within the region of the size of Q^{-1} is clearly $(\mu^2/q_{\perp}^2)^2$. For a pp scattering all four protons have to be in this region at the point of interaction so the cross section must be of the form

$$\sigma \sim \left(\frac{1}{q_{\perp}^2}\right)^4 \frac{1}{q_{\perp}^2} \quad (2.10)$$

This leads to a differential cross section

$$\frac{d\sigma}{dt} \sim s^{-10} \quad (2.11)$$

at fixed angles, which is exactly the counting rule.

Now it is easy to see why only minimum valence quark Fock states contribute to the large momentum transfer interaction. From the expression of T_H we see that scattering off any state that contains more constituents will introduce more powers of q^{-2} , since the hard scattering would have to turn more lines by large angles.

2.2 The large hadron model (Lan 1974)

Based on a phase space analysis V. Landshoff (Lan 1974) proposed a model that accounts for the pp elastic scattering data almost equally well. In this model the large momentum scattering between hadrons is assumed to proceed through direct and independent head-on collisions of the constituents of the hadrons. The scattering angles of each constituent is fine-tuned so the final state protons can be formed out of these scattered constituents. With contributions from both the pinch singularity and end point singularity in phase space, the pure Landshoff mechanism gives a power law with a power of 8 for pp elastic scattering comparing to the dimensional counting law of 10. However, as has been pointed out by many researchers, there are additional suppressions, called Sudakov suppressions, which come into play because of the large distance nature of the interactions. Plainly put the suppressions come from the fact that when separated by large distances in strong fields, the colored constituents emit gluons incessantly. This reduces the probability of the incoming protons being in the three constituent states, which in turn means reductions in the hard scattering cross section. We will outline the analysis by A. Mueller (Mue 1981) for pion pion scattering here.

Using the notations in fig. 2.5, the scattering amplitude can be written as:

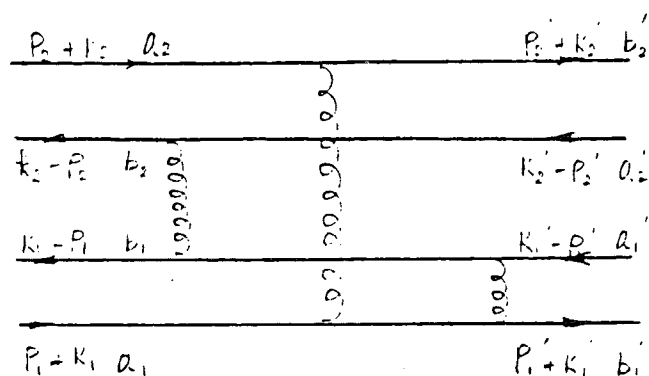


Fig. 2.5 The Landshoff picture for a $\pi\pi$ scattering.

$$H(p, k, p', k') = \frac{1}{16} \sum (\gamma \cdot p_1 \gamma_5)_{a_1 b_1} (\gamma \cdot p_2 \gamma_5)_{a_2 b_2} (\gamma \cdot p_2' \gamma_5)_{a_1' b_1'} (\gamma \cdot p_1' \gamma_5)_{a_2' b_2'} H_{a_1 b_1 \dots a_2' b_2'}(p, k, p', k')$$

(2.12)

where $H_{a_1 b_1 \dots a_2' b_2'}$ is the independent constituent scattering amplitude.

Define the fractions of momenta carried by i th constituent by x_i , $x_i =$

$|\vec{k}_i|/|\vec{p}_i|$, $x_i' = |\vec{k}_i'|/|\vec{p}_i'|$ the cross section can then be written as:

$$\frac{d\sigma}{dt} = \frac{1}{s^2} \left| \int dx_1 dx_2 dx'_1 dx'_2 \right.$$

$$\left. \phi_\pi(x_1, s) \phi_\pi(x_2, s) \phi_\pi(x'_1, s) \phi_\pi(x'_2, s) H(p, p', k, k') + \dots \right|^2 \quad (2.13)$$

Here $s = (2p_1 + 2p_2)^2$, $t = (2p_1 - 2p_2)^2$, $\phi_\pi(x, s)$'s are the renormalization group evolved wave functions, and H is the hard scattering amplitude.

$$H(p, p', k, k') = \frac{g^2}{16} \frac{\text{tr}\{\gamma \cdot p_2 \gamma_5 \gamma_\alpha \gamma \cdot p'_2 \gamma_5 \gamma_\beta\}}{[(p_2 - k_2 - p'_2 + k'_2)^2 + i\epsilon][(p_2 + k_2 - p'_2 - k'_2)^2 + i\epsilon]}$$

$$\times \frac{\text{tr}\{\gamma \cdot p_1 \gamma_5 \gamma_\alpha \gamma \cdot (p'_2 - k'_2 - p_2 + k_2 - p_1 + k_1) \gamma_\lambda \gamma \cdot p'_1 \gamma_5 \gamma_\lambda \gamma \cdot (p_1 + k_1 + p_2 + k_2 - p'_2 - k'_2) \gamma_\beta\}}{[(p_1 + k_1 + p_2 + k_2 - p'_1 - k'_1 - k'_2)^2 + i\epsilon][(p_1 + k_1 + p_2 + k_2 - p'_2 - k'_2)^2 + i\epsilon][(p'_2 - k'_2 - p_2 + k_2 - p_1 + k_1)^2 + i\epsilon]} \quad (2.14)$$

At very high energies, all the masses can be neglected. We find,

$$(p_2 - k_2 - p'_2 + k'_2)^2 = \frac{1}{4} t (1 - x_2) (1 - x'_2) \quad (2.15)$$

$$(p_2+k_2-p_2'-k_2')^2 = \frac{1}{4} t(1+x_2)(1+x_2') \quad (2.16)$$

$$(p_1+k_1+p_2+k_2-p_1'-k_1'-p_2'-k_2')^2 = \frac{1}{8} s[2(x_1-x_1')(x_2-x_2')-(1-\cos\theta)(x_1-x_2)(x_1'-x_2')] \quad (2.17)$$

$$(p_1+k_1+p_2+k_2-p_2'-k_2')^2 = \frac{1}{8} s[2(1+x_1)(x_2-x_2')+(1-\cos\theta)(1+x_2')(x_1-x_2)] \quad (2.18)$$

$$(p_2'-k_2'-p_2+k_2-p_1+k_1)^2 = -\frac{1}{8} s[(2(1-x_1)(x_2-x_2')+(1-\cos\theta)(1-x_2')(x_1-x_2)] \quad (2.19)$$

The product of the two traces is

$$\frac{-s^3}{16} \sin^2\theta [(x_1-x_2')^2+(x_1-x_2)^2] \quad (2.20)$$

so

$$H = \frac{4g^6 \sin^2\theta [(x_1-x_2')^2+(x_1-x_2)^2]}{t^2(1-x_2)^2(1-x_2')^2 [(1-x_2')Y-(x_1-x_2')(x_2-x_2')-i\epsilon] [(1+x_2')Y+(x_1-x_2')(x_2-x_2') +i\epsilon]} \quad (2.21)$$

$$x \frac{1}{[(x_2'-x_1')Y+(x_1-x_2')(x_2-x_2')+i\epsilon]} \quad (2.21)$$

where,

$$Y = x_2 - x_2' + \frac{1}{2}(1 - \cos\theta)(x_1 - x_2) \quad (2.22)$$

It is clear that the cross section would be proportional to s^{-6} if there were no singularities. It can be easily seen that singularity arises when $x_1 = x_2 = x_2'$ such that all three denominators vanish. This is usually referred to as the Landshoff pinch singularity. Another kind of singularity, called the end-point singularity, is associated with the fact that the phase space integral diverges when one of the constituents is allowed to carry all the momentum of the parent pion. These two singularities bring the energy dependence of $\pi\pi$ elastic scattering cross section from s^{-6} to s^{-5} , as shown by a more careful analysis of the cross section near the pinch points by A. Mueller. From the above discussions, we see that pure Landshoff mechanism would give more slowly varying cross sections, which would mean that the Landshoff mechanism dominates at high energies. However, this is not the case. It turns out that there is one more thing that we haven't touched upon yet. It is well known in QED that a charged particle loses its energy by incessantly emitting photons when moving in strong electromagnetic fields. The situation is similar in QCD. When moving in strong color fields, a color charge loses its energy by incessant emission of

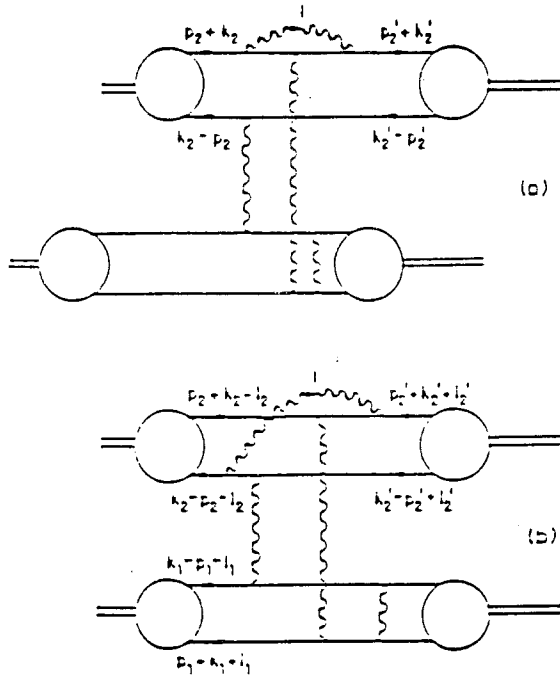


Fig. 2.6 Sample Sudakov suppression diagrams.

gluons. Some sample diagrams are shown in fig. 2.6. Thus, the probability that a color charge remains an isolated color charge is reduced. In an elastic hadron scattering process, this gluon emission reduces the probability for a hadron to be in its minimum constituent state, thus, reducing the scattering cross section. This is called Sudakov suppression, which results in a double log term that modifies the power dependence of the pion pion elastic scattering cross section from 5 to a number close to 6, in agreement with what predicted by the dimensional counting rule.

The measured cross section is close to that predicted by the counting rule, which seems to indicate that the Sudakov suppressions must be in effect assuming that the pinch processes do make important contributions in the hard scattering processes.

2.3 The phenomenological models and the experimental status of exclusive interactions

As we have mentioned before, neither of the two models described above can give detailed information on the angular distributions. A number of phenomenological models have been developed in order to explain various aspects of the experimental results on exclusive interactions. Most notably the constituent interchange model (CIM) of Gunion, Brodsky and Blankenbecler (Gun 1973), the quark rearrangement model of Fishbane and Quigg (Fis 1973), and the statistical models. The CIM assumes that the dominant processes in hard hadronic interactions are the ones in which the hadrons swap valence quarks rather than exchanging gluons. The model, though successful in predicting the scaling behavior and angular distributions for a number of interactions, has difficulties in getting the absolute normalizations right. The rearrangement model, which treats the constituents in a democratic way in deriving the cross sections, assumes that the scattering hadrons pool their constituents together at the interaction point. With the help of three characteristic constants M , B , and D , which represent the probabilities of deassociating a meson, a baryon, and a decuplet baryon respectively, the cross sections can be derived by simply counting the number of ways of collecting the necessary constituents to form a given final state. For example, in pp scattering there are 12 ways to collect the uud quarks necessary to form a proton

from a pool of $uuuudd$ while in pn scattering there are only 9 ways to collect uud quarks necessary to form a neutron from a pool of $uuuddd$. Therefore the ratio of pp elastic cross section to that of pn is $12/9$. However, in treating interactions involving mesons, the model requires more constants to account for the possibilities that a $u\bar{u}$ can annihilate and produce a $d\bar{d}$ or $s\bar{s}$. With these constants and a few more plausible assumptions, the model predicts a number of cross sections for processes involving mesons, e.g., the model predicts a ratio of 1.5 for π^+p elastic scattering to π^-p elastic scattering cross sections. The statistical model differ from all the constituent based models in that it treats the hadronic interactions in terms of available phase space. The model assumes that the interactions proceed through direct resonances. At the collision point, the colliding particles lose part of their energies to internal excitations and form various resonances. These resonances travel along their directions of motion and "boil off" hadrons in proportion to their available phase space, in order to reach thermal equilibrium with their environment. In particular, the model predict an elastic cross section of the form,

$$\frac{d\sigma}{dt} \propto \exp\left(\frac{-\sqrt{s}}{T_0}\right) \quad (2.23)$$

Experimental tests of QCD on exclusive interactions are still largely qualitative or semi quantitative. Comparison between theoretical predictions and the data necessitates the normalizations of the wave functions of the hadrons, which have not been calculated from first principles up to now. However there has been impressive progresses in the last few years. In particular, results from lattice gauge calculations and QCD sum rule analysis have been very encouraging. Using the normalizations from the sum rule analysis, theoretical predictions and the data on pion form factors and nucleon form factors seem to agree quite well, as shown in fig. 2.7 and fig. 2.8 respectively. Another area where PQCD can be directly confronted

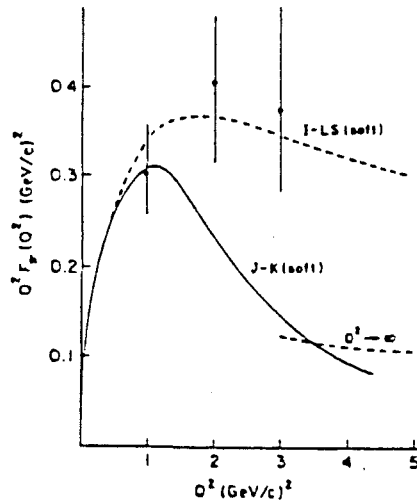


Fig. 2.7 Comparison of between the theory and the data on pion form factor (Bro 1987).

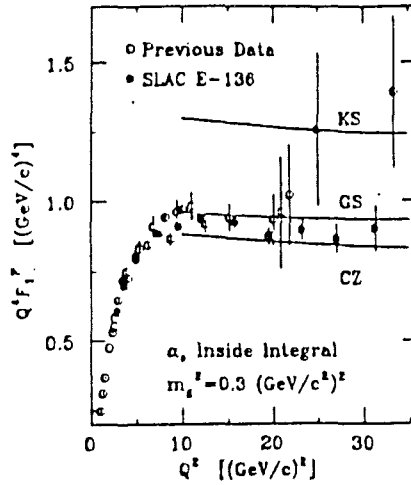


Fig. 2.8 Comparison between the theory and the data on proton form factor (Bro 1987).

with data is the two photon productions of meson pairs, e.g., $\gamma\gamma \rightarrow \pi^+\pi^-$ which, according to Brodsky (Bro,1981), is essentially independent of the wave functions. Fig. 2.9 shows the data from PEP and the corresponding QCD curve. Another way of testing PQCD is by measuring and comparing cross sections for different exclusive interactions. Data from a number of channels seem to agree with the notion of SU(6) wave functions for hadronic interactions (Bal 1988).

As were shown in fig. 1.1 and fig. 1.2, exclusive scattering cross sections all show approximate scaling behavior at high energies. To see

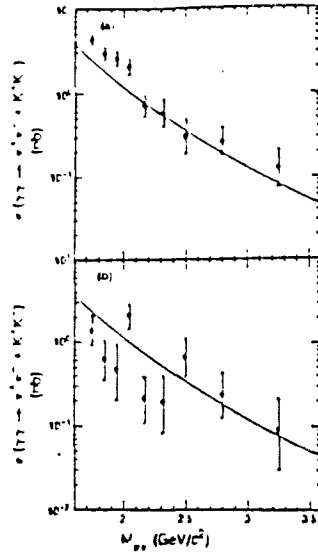


Fig. 2.9 Cross section for two photon processes (Bro 1987).

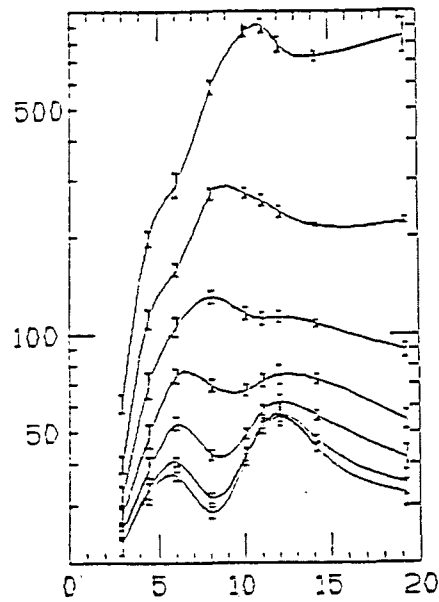


Fig. 2.10 pp cross section as a function of s after factorizing out the power law factor. The lowest curve is for CMS 90 degree scattering.

how well the data scale fig. 2.10 shows a plot of pp scattering cross section $\frac{d\sigma}{dt}$, taking out the scaling factor, as a function of the lab energy, which would be a constant if the scaling law were exact. It can be seen the variations (sometimes referred to as the oscillatory behavior) are within a factor of 2.

The most troublesome area in pp scattering is probably in the spin phenomena. In the lowest order PQCD helicities are conserved in hadronic interactions. Data on the asymmetry parameter A_{NN} from polarized proton scattering experiments, shown in fig. 2.11, can not be

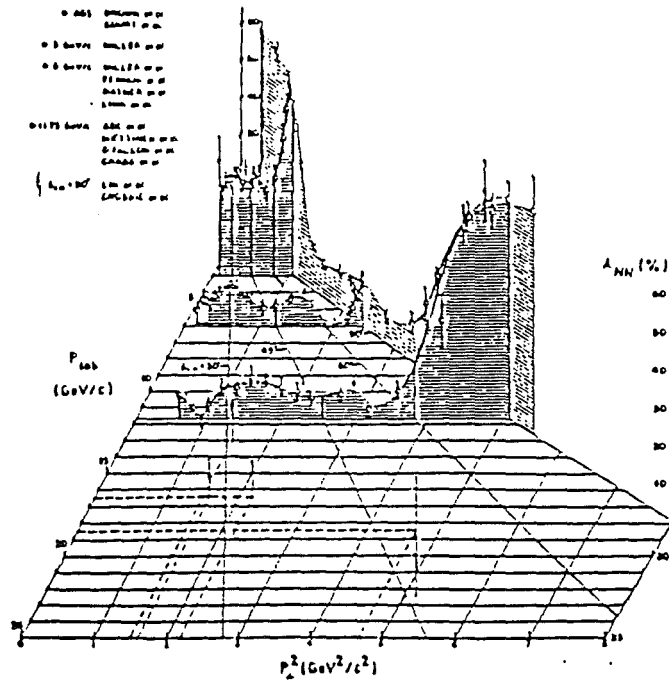


Fig. 2.11 Asymmetry for the polarized proton scattering.

distributions also indicates significant helicity non-conserving contributions. Furthermore, recent results on polarized target structure functions from the EMC group seem to pose more problems. The verdict from the community varies from announcing the death of QCD to warning against over-interpreting the data by Close. It is probably premature to jump at the conclusion that PQCD is wrong just from these results. However, the discrepancies do signify the complexity of exclusive interactions, in that high incident energy alone does not warrant the use of perturbative expansions.

2.4 Nuclear transparency to hard scattered hadrons

Even though the two models described in sections 2.3 and 2.4 lead to similar cross sections for wide angle pp elastic scattering, after taking into consideration the Sudakov suppression for the large hadron model, their underlying processes are quite different. In the small hadron model, the scattering is assumed to proceed through three distinct steps. First, the constituents of the hadrons gather themselves to a small region with a transverse size of the order of Q^{-1} . The anomalously small objects then exchange hard gluons or quarks carrying four momentum of the order of q^2 . Finally the small hadrons expand back to their normal sizes. The large hadron model, on the other hand, assumes that the scattering occurs between normally configured hadrons. The crucial difference between the two models is the distance scale of the interactions. It is claimed (Lep, 1980) that the pinch processes, though existent at low energies, will become less and less important as the energy gets higher and higher because of their large distance nature. As was pointed out in the Introduction, one way of differentiating between the two models is by measuring the quasi elastic scattering cross sections off nuclear targets. If the hadrons are indeed small at the point of interaction, as assumed by the small hadron model, we should be able to observe the color transparency effect. That is, the ratio of the cross section of quasi elastic

scattering to that of free particle scattering should be appreciably higher than what has been observed at low energies and should increase with energy until reaching an asymptotic value of 1.0 at extremely high energies. If, on the other hand, the scattering is dominated by the large hadron processes, strong absorptions will make any elastic scattering with the interior protons practically un-observable due to initial and final state interactions. Thus, the ratio of the cross sections will be very small and, more or less, energy independent.

It is probably appropriate to give some estimates on the conditions under which the color transparency effect can be seen. First of all, the momentum transfer has to be large enough so that the hadrons can shrink to small sizes at the point of interaction. Furthermore in order for the color transparency effect to manifest itself the time it takes for the small hadrons to expand to their normal sizes has to be longer than the time it takes for the hadrons to travel through the nucleus. The first condition means that $1/\sqrt{t} \ll r_h$ where r_h is the size of the hadron, about 1 fm. Thus, momentum transfers of the order of 3 to 4 Gev should be enough. To arrive at the necessary energy, we note that the expansion time is approximately $1/\langle k_t \rangle$ where $\langle k_t \rangle$ is the typical intrinsic transverse momentum of a hadron, and the travel time of the hadron to exit the nucleus in the laboratory is $2R$, where R is the radius of the nucleus. The requirements that the initial and final

state hadrons be outside the nucleus before reaching their normal sizes can then be expressed as,

$$\frac{E}{m_h \langle k_t \rangle} \gg 2R \quad (2.24)$$

$$\frac{E'}{m_h \langle k_t \rangle} \gg 2R \quad (2.25)$$

where E and E' are the energies of the initial and final state hadrons respectively, (For the initial state particle, the precise statement should be that the size of the particle be smaller than a normal hadron before entering the nucleus. Technically , however, the problem is reversible, i.e., entering the nucleus with a small sizes is equivalent to exiting the nucleus remaining small.). Taking $\langle k_t \rangle$ to be .3 Gev, these conditions mean that energies of the order of 3 and 20 Gev are required respectively for the small pions and protons to exit the nucleus with negligible initial and final state interactions. Thus, incident energies of the order of 6 and 40 Gev are needed for $\pi\pi$ and pp scattering, respectively, at CMS 90 degrees.

In summary, the small hadron model predicts that at asymptotic energies the nucleus will be perfectly transparent to hard scattered hadrons. This means that the cross section for quasi elastic hadron nucleon scattering off a nuclear target at very high energies will be

proportional to the total number of nucleons in the nucleus A . At lower energies, we should still be able to observe increases of the transparency as the energy of the scattering process increases. In addition, detailed measurement of the transparency varying as energy and momentum transfer may provide us with important information on the short distance structure of the wave functions of the hadrons.

Nuclear transparency to hard scattered hadrons is only one of the effects predicted by the short distance scattering model. Other observable effects include enhancement in heavy flavor production off nuclear targets and absence of colinear hard inelastic interactions between fast moving hadrons and nuclear targets. All of these effects follow directly from the scaling property. For example at high enough energies, the heavy flavor particles are produced with sizes given by their masses, $r_q \sim 1/M_q$. If the time it takes for this anomalously small particle to grow to its normal size is longer than that for the particle to travel through the nucleus, then the physical particles will be formed outside the nucleus. The absorptions by the nuclear matter should be negligible. Therefore, the cross section of producing heavy flavor particles out of nuclear targets at high energies should also be proportional to the total number of nucleons A .

2.5 Fermi motion of nucleons inside a nucleus and its effects.

Since Fermi motion of the nucleons within the nucleus is both an interesting problem for the experiment, and an aspect which will greatly complicate the interpretation of the data, it seems fair to discuss it in a little more detail here.

Nucleons inside a nucleus can not be all at rest, according to Pauli exclusion principle. The simplest way of obtaining the momentum distribution functions is to treat the nucleons as free Fermi gas. Assuming that there are A nucleons we then have,

$$\begin{aligned} A &= 2 \frac{2}{h^3} \int_{\Omega} d\vec{r} d\vec{p} \\ &= 16\pi V \frac{p_f^3}{3h^3} \end{aligned} \quad (2.26)$$

$$p_f = \left(\frac{3h^3}{16\pi} \frac{A}{V} \right)^{1/3} \quad (2.27)$$

This means that the Fermi momentum (note that Fermi momentum here is used for the characteristic momentum for the nucleus, which is different from the generic name for the internal momentum) is independent of the nucleus being considered since V is proportional to

the mass number A . However it is well known that the nucleons are not truly free inside the nucleus, and such effects as the residue interactions, symmetry effects, surface effects, etc, neglected completely in the free Fermi gas model, play important roles in shaping up the spectrum of the nucleons. Furthermore, experimental data indicates that there are short distance correlations among the nucleons, which gives rise to the existence of high momentum tails in the spectral distributions.

The spectral functions have been studied in low energy quasi elastic electron nucleon scattering experiments, in which the electron scatters off one of the protons. By assuming that the observed cross section factorizes into a free particle cross section and a momentum distribution function of the target proton, nucleon spectra can be deduced from these measurements. Fig. 2.12 is a typical plot from such measurements. In addition, if one assumes that the spectrum can be approximated by the free Fermi gas model, Fermi momentum can be extracted. In fig. 2.13 the measured Fermi momenta are plotted as a function of the mass number A .

It can be seen that the free Fermi gas model prediction of constancy in Fermi momentum agrees with the data quite well for heavy nuclei.

However these low energy measurements can not probe into the high momentum region of the spectrum. Now, if we assume that the observed cross section in a hadron nucleon scattering process can similarly be written as a free particle cross section modulated by a momentum

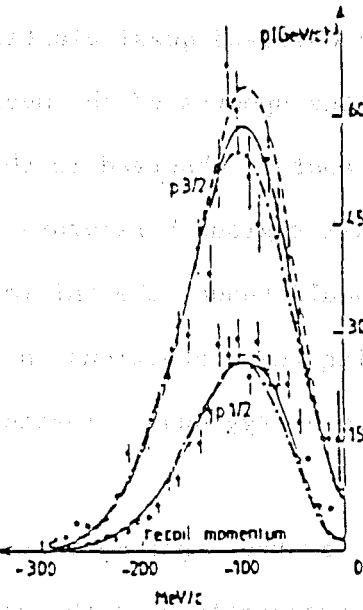


Fig. 2.12 Sample momentum spectrum measured by low energy electron quasi elastic scattering (Fru 1984).

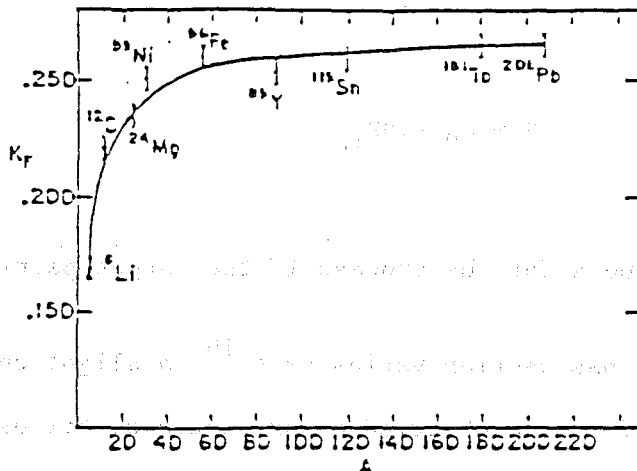


Fig. 2.13 Fermi momentum as a function of A (Bod 1981).

distribution function, the observed quasi elastic event samples can then be used to determine the spectra of the nucleons. With the extremely high momentum transfers observed in this experiment, we should be able to probe tail regions heretofore unexplored. Furthermore the transparency effect should reduce the initial and final state interactions, thus, reducing the distortions on the measured spectral functions, prevalent in low energy quasi elastic hadron nucleon scattering measurements.

Besides being a subject for the experiment, Fermi motion plays important roles in the interpretations of the data. First, the Fermi motion changes the kinematics of the scattering process in a substantial way. To the first order in the target momentum, the s of a pp scattering process between an incoming particle with momentum \vec{p} and a target particle with momentum \vec{p}_f is given by:

$$s = s_0 - 2 \cdot p p_{fz} \quad (2.28)$$

where s_0 would be the s for the process if the target particle were at rest. Because the cross section varies as s^{-10} a slight change in s will drastically affect the observed cross sections. For example, at a beam energy of 10 Gev, a proton scattering off a target proton with a momentum magnitude of .25 Gev moving parallel to the incoming momentum

has a s value of 15 GeV^2 , comparing to a s value of 25 GeV^2 when the target proton moves anti-parallel. This difference in turn means a difference in the cross section of a factor of 165, even though the beam momentum for the two cases is the same. This necessitates corrections in deriving the transparency from the observed event distributions because the scattering processes off the nuclear protons will be at effective energies different from that of the beam, depending on their momenta. On the other hand, this change in the effective energy due to Fermi motion will also enable us to observe the transparency at energies different from the beam, by dividing the data into different p_{fz} regions where p_{fz} is the longitudinal component of the Fermi momentum. Another important effect of the Fermi motion is that it smears the otherwise monochromatic fixed angle spectrum into a much broader distribution, thus, making the identification of the elastic scattering events from nuclear targets much more complicated. Kinematic constraints such as constraints on the coplanarities, missing masses, and opening angles, can not be used to identify nuclear elastic events anymore. More elaborate ways have to be devised to extract the nuclear elastic signals.

Chapter 3 The apparatus

We now turn to the description of the apparatus used for this experiment.

The experiment, designated as E834, was carried out at Brookhaven National Laboratory on Long Island, New York. The apparatus, consisting of a single arm spectrometer with momentum analysis in the vertical plane and a series of multi-wire proportional chambers which measure the directions of the recoil particles, was specifically designed for large angle exclusive interaction experiments. Mounted on a platform the spectrometer can rotate horizontally with an angular span of ± 22 degree. This greatly facilitates the centering of the apparatus to accept CMS fixed angle scattering events at different energies. In addition, the down stream part of the spectrometer can be lowered to accommodate different bending angles to the particles going through the spectrometer thus maximizing the acceptance. The angular range of the spectrometer is about 4 degrees in the laboratory and the side arm was arranged to record all elastic events accepted by the the spectrometer. With a bending power of about 20 kG-meter and long arms the spectrometer gives a momentum resolution of better than 1% at 10 Gev. Angular resolution of the side arm is about 5 milli-radians. A three stage trigger was implemented to select events with the desired

transverse momentum p_t . The apparatus can handle a flux of 5×10^7 particles per .75 second spill.

The beam line

Fig. 3.1 shows a lay out of the beam line C1 which was used for E834. The primary beam of 28 Gev protons from the AGS was extracted and directed to a production copper target C. A series of quadrupoles Q0 through Q5 followed immediately to focus the spray of secondary particles into a beam. A horizontal dipole magnet C1D1 followed to disperse the beam and direct particles with correct charges and approximately correct momenta towards a collimator C1C1 which moves horizontally to select a slice of the beam with the desired momentum dispersion. The intensity of the beam was controlled by another collimator C1C2 which moves vertically. The dipole magnet C1D2 was used to bend the beam towards the house where our detector was located. In order to bring the beam to the experimental target which is about 9 feet higher than the beam line at this point a series of pitching magnets P1 to P6 were used. Final re-focusing by quadrupole magnets Q8, Q9 and Q10 brings the beam to a size of about 1.5 inches in diameter at the target. Individual particle positions were measured by a beam hodoscope BH3 which is composed of 16 horizontally and 16 vertically oriented scintillation counters each 1/8 inches wide. Various elements including two spot counters located between the beam cherenkov counters, an segmented ionization chamber SWIC, a spot counter Q located in front of the experimental target, and a three element beam telescope BTEL were used to monitor the beam intensity. It should be

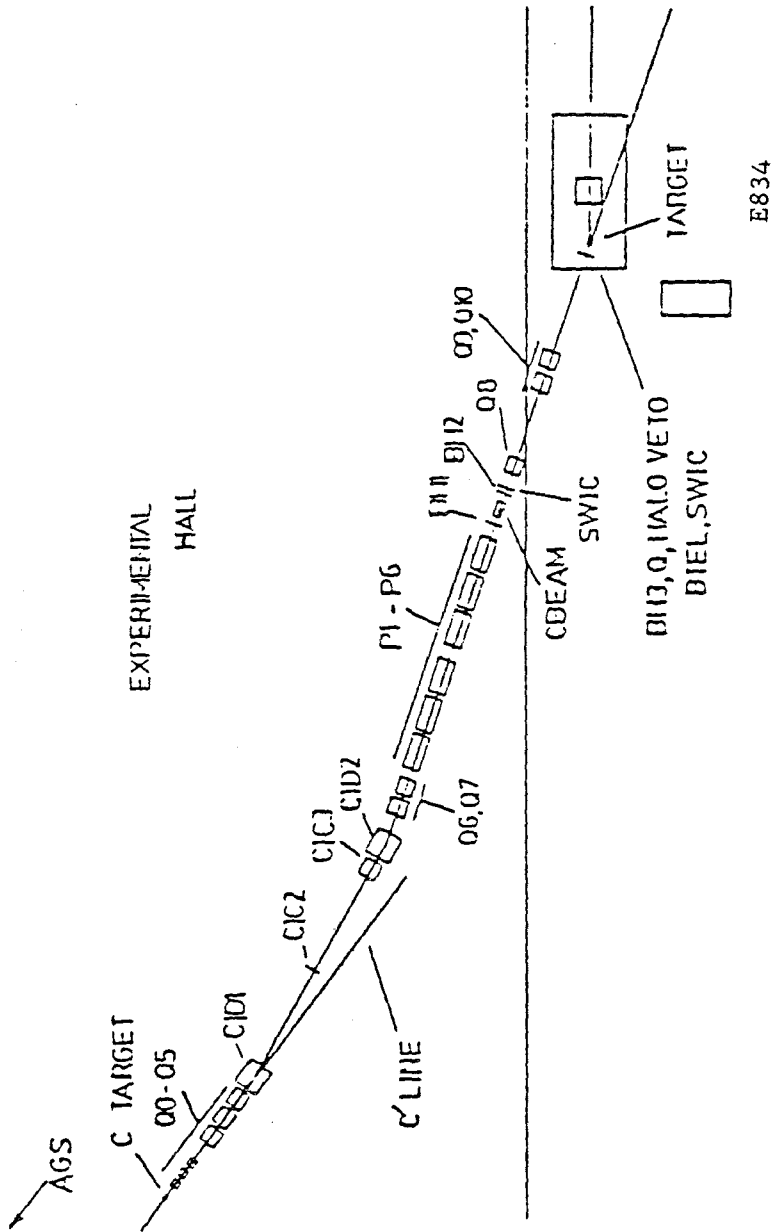


Figure 3.1.1 C1 beam line.

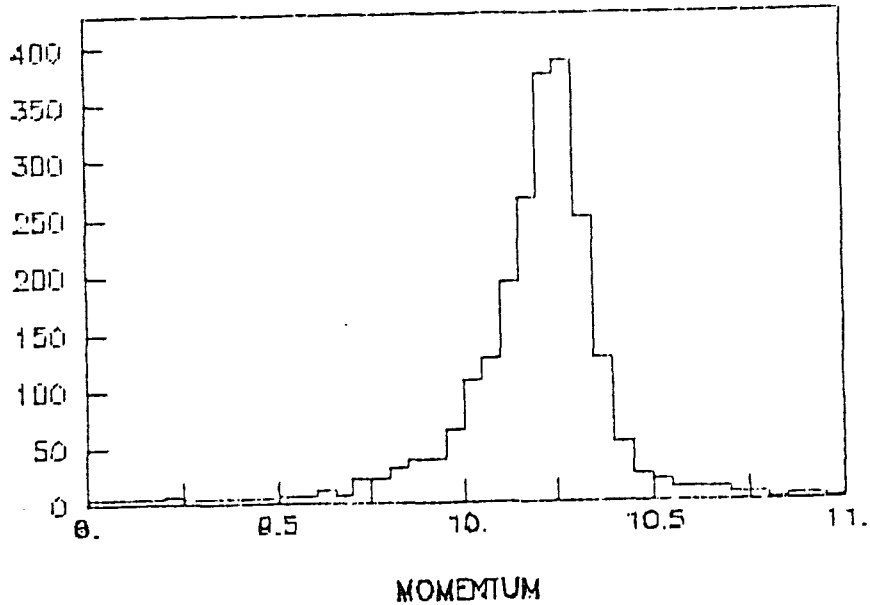


Fig. 3.2 The beam momentum dispersion.

pointed out that accuracy in knowing the beam intensity was not very important due to the design of the target and the fact that we were only interested in the ratio of the cross sections for scattering off nuclear targets to that off hydrogen targets. An off-line study with elastic hydrogen events indicates that the momentum spread of the beam is about 1% (FWHM) as shown in fig. 3.2, which is quite satisfactory for our purpose.

3.2 The target assembly

The dominant processes in hadron nucleus interactions involve either low energy particle productions or target break up's. The cross sections for large angle quasi elastic scattering processes are small, typically a few to a few tens of nanobarns. Two veto counter packages were used to enhance the signal to background ratio for quasi elastic scattering. Each package consisted of three layers of 3/16 inch thick scintillators sandwiched with two layers of one radiation length lead. These packages were supported by two layers of 3/8 inch plastic plates. The 30 by 12 inch packages covered the top and the bottom of the target area, about 90% of the solid angle. Fig. 3.3 is a sketch of the veto packages together with the target assembly. The plastic support plates closest to the beam also helped to absorb the nuclear debris from the decay of an excited nucleus after one of its protons was knocked out. Each of the counters was read out with 2 inch photomultipliers and the signals were amplified by dc amplifiers to ensure their capability of handling high rate, which is crucial to the success of the experiment. Using good elastic event candidates it was established that by demanding at least two counters from either side with hits to veto an event the signals can be clearly separated from the background. The counters run at single rates of about 1.5×10^6 counts per spill. With an event gate of 20 nanoseconds and coincidence of at least two counters, the accidental veto rate was negligible.

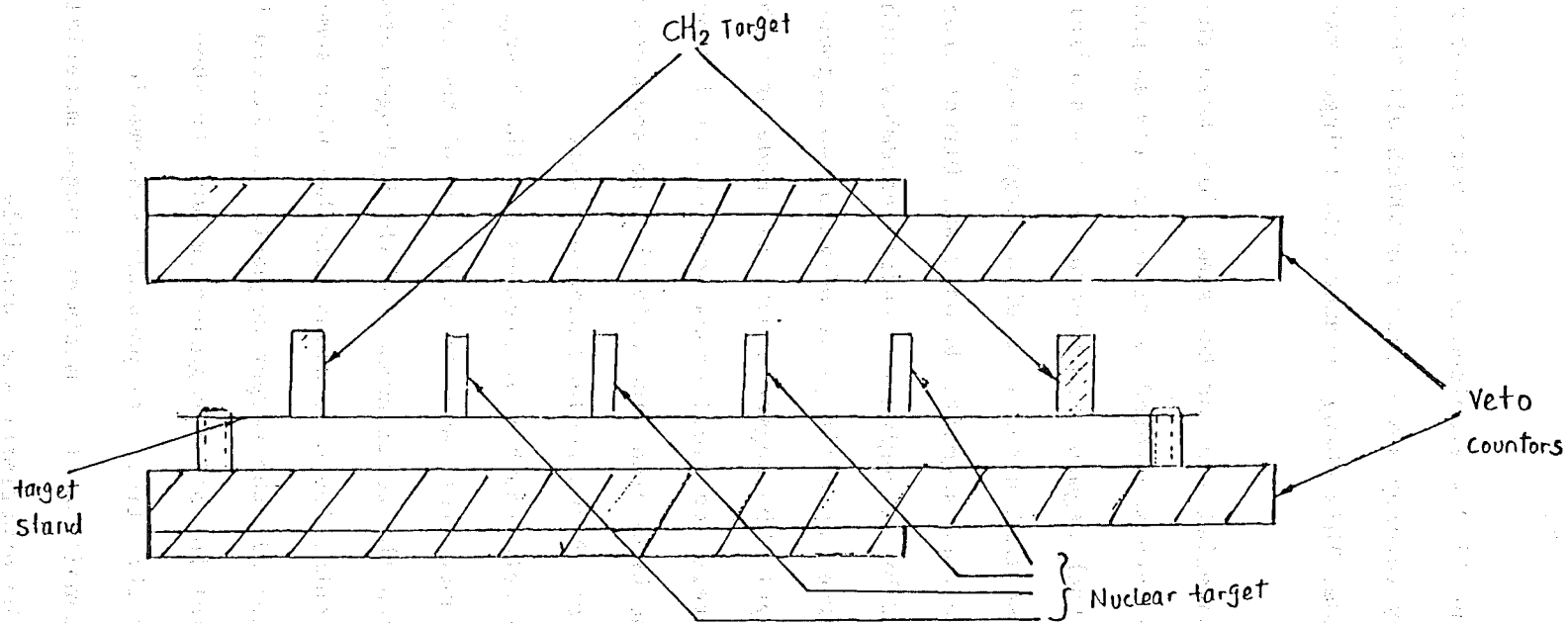


Fig. 3.3 Schematic view of the target assembly.

During the long span of the 12 Gev aluminum run the veto counters were put into the trigger by vetoing any events for which all three counters fired on either side. This change reduced the trigger rate by a factor of 4.

In order to have enough material and, at the same time, keep the absorptions to the outgoing hard scattered particles as low as possible segmented target was used. Each segment was separated by a sufficient distance from the next one so that a particle with large angle scattering would not pass through segments downstream. Direct cross section ratios were measured by arranging the target assembly such that four segments of nuclear target were always in between two segments of polyethylene (hydrogen) target. The segments were all made of high purity solid with approximately identical cross sections of 1.2 by 2.4 inches commensurate with the beam size. The polyethylene segments were 2 inches thick. The thickness of the nuclear segments were appropriately chosen so the total number of protons for the 4 segments of the nuclear targets is about the same for each type of the target material and is about 5 times the total number of the hydrogen atoms for the 2 polyethylene segments. The dimensions together with some other relevant parameters for all the target segments are listed in Table 3.1. The total material for all 6 segments amounts to about 0.1 interaction length. To keep the effects of possible systematic variations of the running conditions to a minimum, target material was switched regularly during the experiment when possible.

Table 3.1 Parameters of the target segments

Tgt	N_s	Dim (hxxxd) (cm)	Vol (cm^3)	Den (g/cm^3)	N_p (in unit of N_a)	N_N/N_H
CH ₂	2	6.1x5.1x3.0	94.3	0.93	100.2	
(H ₂)					25.0	1.00
(C)					75.1	3.00
Li	4	6.1x3.0x7.62	139.4	0.534	127.6	5.11
C	4	6.1x3.0x1.6	117.2	1.8	105.5	4.12
Al	4	6.1x3.0x1.3	95.2	2.7	123.8	4.95
Cu	4	6.1x3.1x0.4	30.3	8.9	124.1	4.96
Pb	4	6.1x3.0x0.4	29.3	11.2	130.0	5.20

3.3 The beam Cherenkov counters

The beam used for E834 consisted of about 60% positively charged pions, 40% protons and a small fraction of positively charged kaons at 6 Gev. At 12 Gev the corresponding fractions for pions and protons were about 30% and 70% respectively. Beam identification was accomplished by two differential Cherenkov counters. A Cherenkov counter works on the principle that a charged particle, when traveling in a medium with a speed larger than the velocity of light in that medium c/n , (n is the index of refraction of the medium) causes a coherent response by the medium in the form of radiation, called Cherenkov radiation, emitted at a characteristic angle θ with respect to the particle direction:

$$\cos(\theta) = \frac{1}{n\beta} \quad (3.1)$$

If a counter is designed such that particles with speeds greater than a threshold $\beta > \frac{1}{n}$ will all register their existence, it is called a threshold Cherenkov counter. The other type of Cherenkov counter is a differential device in which particles of different velocities radiate at different angles. When focused with a spherical mirror or a convex lens the Cherenkov light forms characteristic rings of images on the focal plane as shown schematically in fig. 3.4. The radii of the rings measure the Cherenkov angles which in turn measure the velocities of

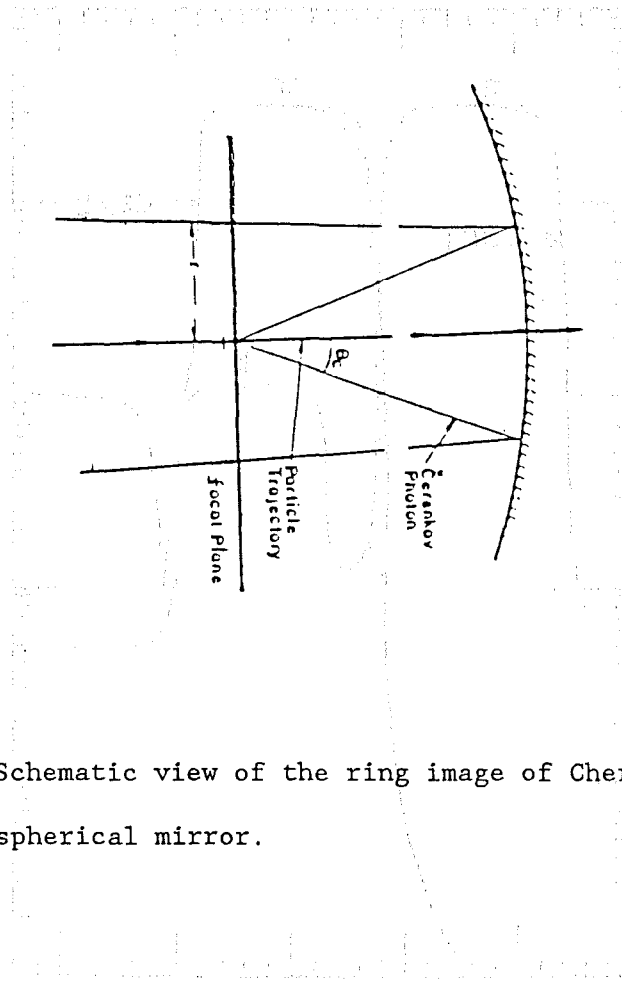


Fig. 3.4 Schematic view of the ring image of Cherenkov light focused by a spherical mirror.

the particles. In this way one can build a counter in which particles with many velocities radiate but only particles with speeds within β to $\beta + \delta\beta$ register themselves. With multiple, optically decoupled rings a counter can be built to distinguish particles with different speeds. The two counters used for beam identification in E834 were of identical construction, each 58 inches in length and 20 inches in diameter. Each counter has two optically decoupled rings of six 2 inch photomultipliers symmetrically mounted around the lens axis of the

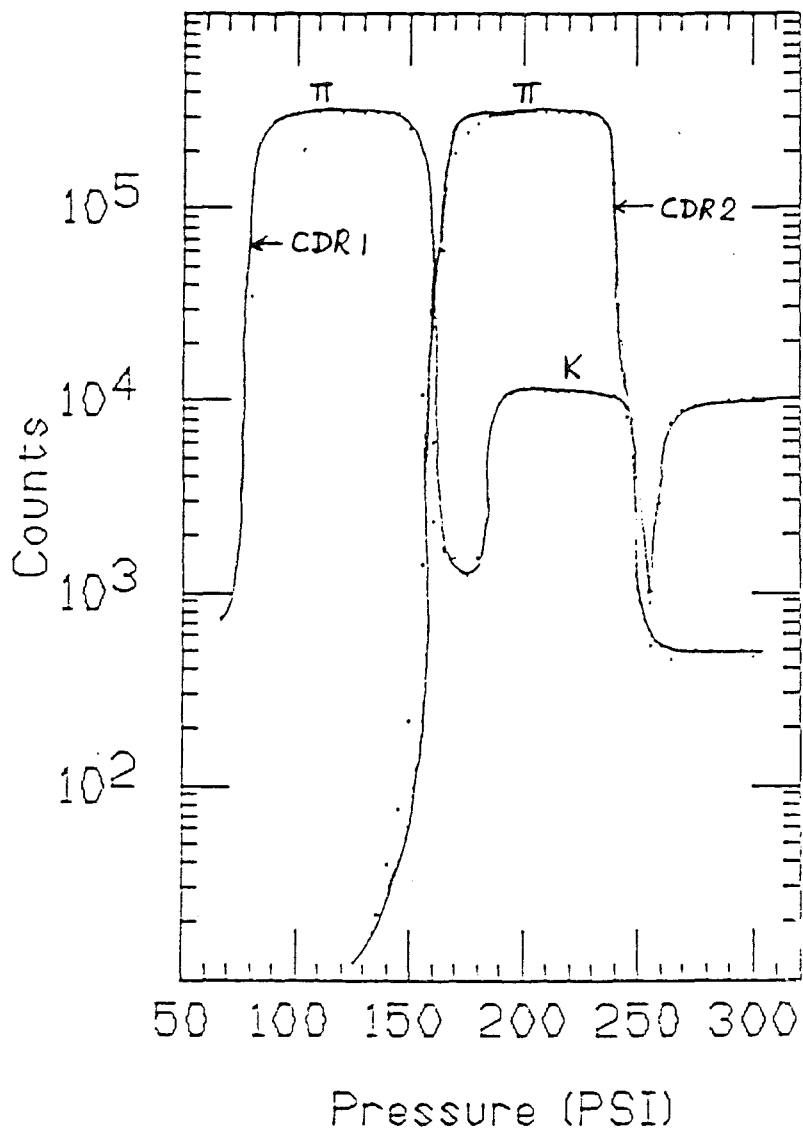


Fig. 3.5 Calibration curves of CDR1 and CDR2 at 6 Gev.

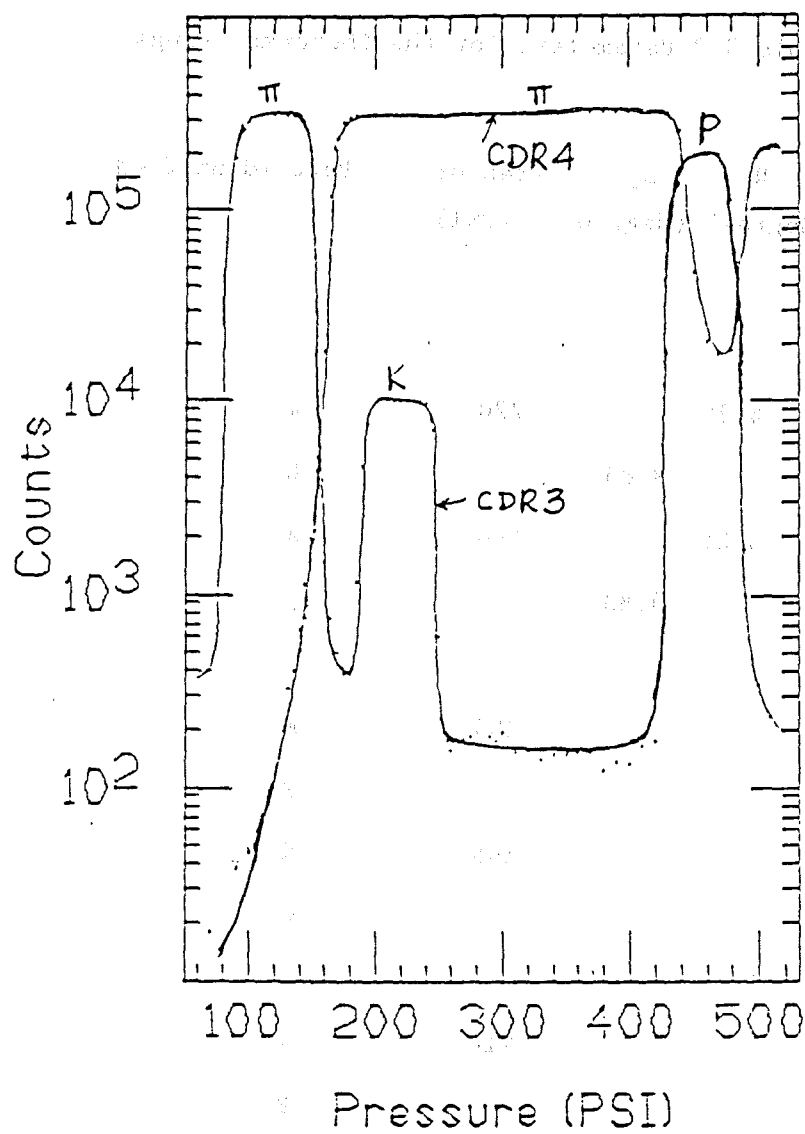


Fig. 3.6 Calibration curves for CDR3 and CDR4 at 6 GeV.

Table 3.2 Parameters for the Cherenkov rings

Ring	R_i (degree)	R_o (degree)	Pressure (PSI)	Part identified
CDR1	4.25		220	π
CDR2		9.83		K
6 Gev CDR3	4.25		460	π
CDR4		9.83		P
CDR1			255	K
CDR2				P
10 Gev CDR3			165	K
CDR4				π
CDR1			210	π
CDR2				P
12 Gev CDR3			120	π
CDR4				π

counter at the focusing plane of a spherical mirror which was mounted at the down stream end of the counter. The counters were located between the last pitching magnet P6 and quadrupole magnet Q8. High pressure carbon dioxide gas was used for the radiator for the counters. A summary of the physical properties together with the running conditions for the rings are listed in Table 3.2 where R_i is the inner radius of the inner ring and R_o is the outer radius of the outer ring. Two sample calibration curves at 6 Gev for the counters are shown in fig. 3.5 and fig. 3.6 respectively. With the help of the timing information the identification accuracy at 6 Gev is almost 100% for protons and about 70% for pions, i.e., about 30% of the doubly identified pion events are actually protons.

3.4 The spectrometer arm

A plan view of the spectrometer, consisting of 4 drift wire chambers (DWC), a bending magnet, two threshold Cherenkov counters and 4 trigger hodoscopes, is shown in fig. 3.7, together with the side proportional wire chambers (PWC) which record the directions of the recoil particles. In the following we will briefly describe each of the components. Throughout this thesis a right handed coordinate system will be used, where the origin is taken to be the center of the target, the positive y axis is taken to be the vertical upward direction, the positive z axis is taken to be the symmetry axis of the spectrometer directed downstream along the beam line and the positive x axis is given by right handedness to be the horizontal axis directed toward the side arm.

The two upstream spectrometer chambers, labeled as DWC3 and DWC4, separated by a distance of about 50 inches from each other, consisted of 3 x and 4 y measuring planes. The other two chambers, labeled as DWC1 and DWC2, separated by 100 inches from each other, consisted of 4 x and 4 y measuring planes and an additional plane which was oriented 30° from the vertical axis. This so-called v plane helps to resolve double track ambiguities. In order to resolve the left-right ambiguities, all adjacent x and y measuring planes were offset by 1/2 wire space from each other. Details on the chambers can be found else

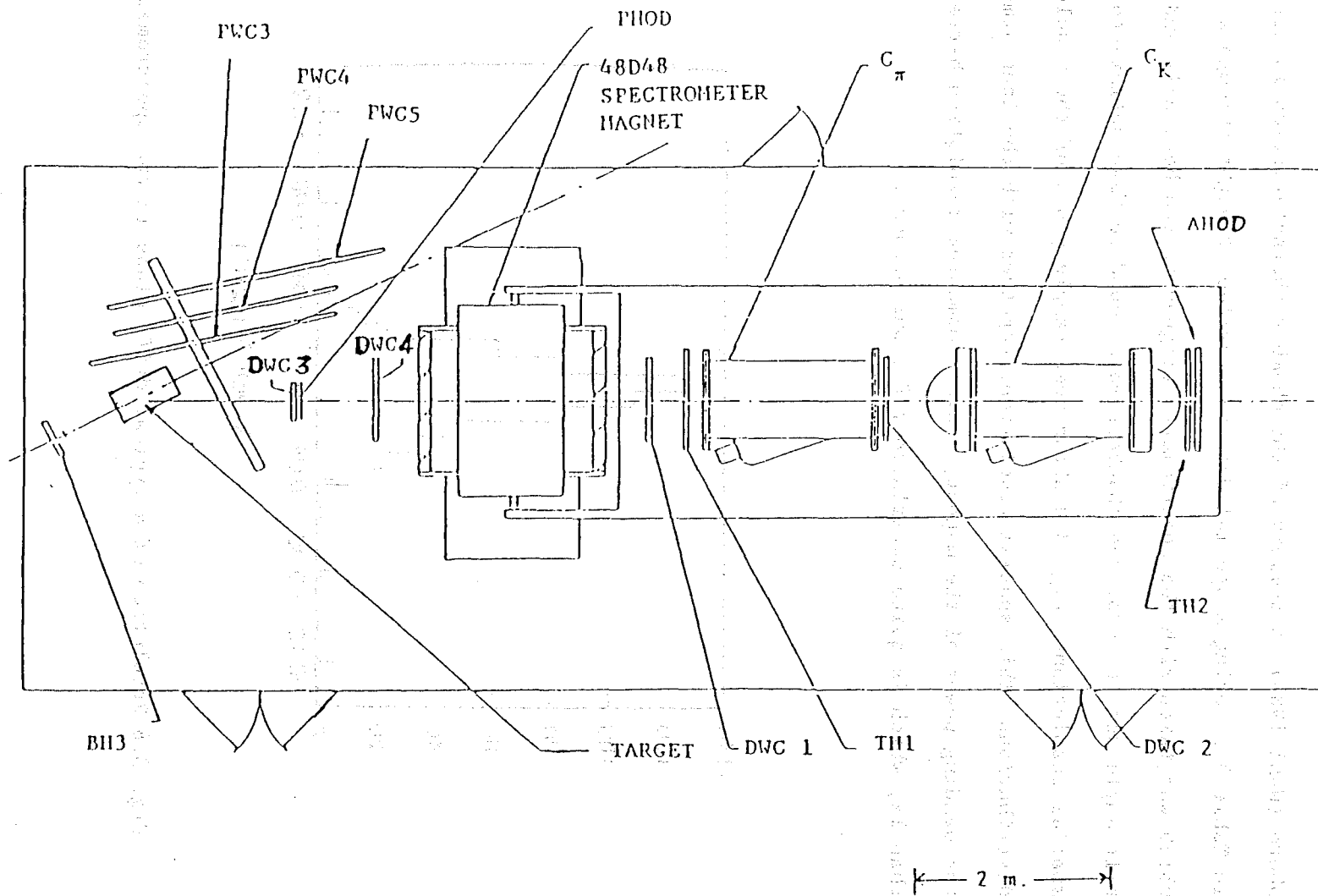


Fig. 3.7 Plan view of the detector.

where (Wahl 1985). A summary of the chamber characteristics is listed in Table 3.3. Using a special data set, called straight through's, which was taken with the spectrometer aligned to the beam axis and the tilt angle set to zero, the chambers were found to have satisfactory spatial resolutions. Fig. 3.8 shows some sample plots of the resolution distributions. This spatial resolution, together with the long arms and the bending power of the magnet, gave a momentum resolution better than 1%, which is quite satisfactory for our purpose.

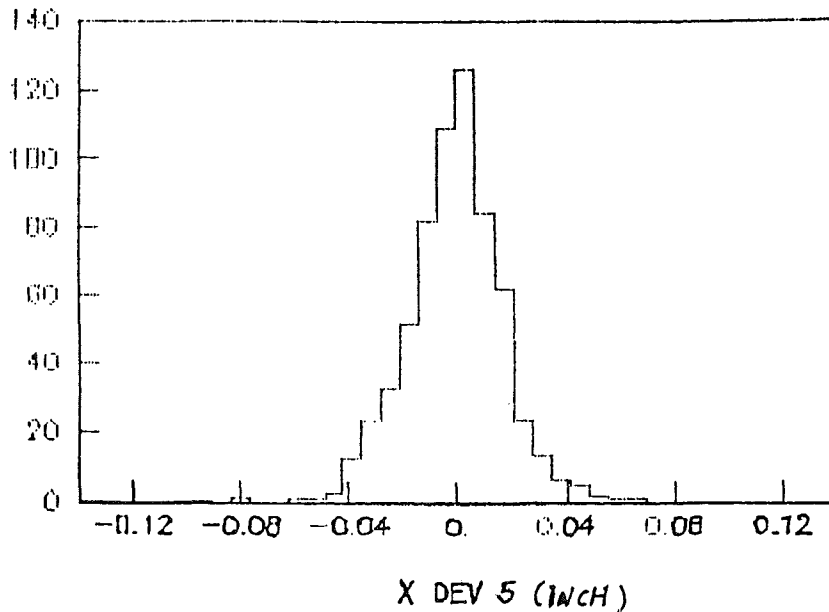


Fig. 3.8 Resolution of a typical drift plane in the spectrometer.

Table 3.4 The chamber parameters

Chamber	Size	Coord. measured	No. of wires	Wire spacing
DWC1	23.5" x 40."	X	93	0.25"
		X	93	0.25"
		Y	160	0.25"
		Y	160	0.25"
		U	160	0.25"
DWC2	32." x 40."	X	62	0.5"
		X	62	0.5"
		Y	80	0.5"
		Y	80	0.5"
DWC3	16.5" x 16.5"	X	124	0.125"
		X	124	0.125"
		Y	128	0.125"
		Y	128	0.125"
DWC4	24." x 32.5"	X	187	0.125"
		Y	256	0.125"
PWC1	48.5" x 35.5"	X	384	0.125"
		U	479	0.125"
		V	479	0.125"
PWC2	64.5" x 39.5"	U	607	0.125"
		V	607	0.125"
PWC3	80.5" x 63.5"	U	815	0.125"
		V	815	0.125"
Integ. mag. field		2 Tm		
Resolution		DWC's 0.5 mm		
		PWC's 1.6 mm		

The magnet, which ran at a central field of about 17 KG, provides a vertical bend that corresponds to a transverse momentum kick of .79 Gev at 10 Gev. The aperture of the magnet is 18 inches horizontally and 48 inches vertically. The effects of the inhomogeneities of the magnetic field were corrected in the software.

The trigger logic is described in Section 3.5. There were four trigger hodoscopes, labeled as PHOD, TH1, TH2, and AHOD respectively in fig. 3.7. The PHOD, located just behind DWC3, contains 4 scintillation counters. The TH1, located in front of the pion counter, was composed of eight 5 inch wide elements. The TH2 consisted of eight 12 inch wide elements, each overlapped with the adjacent two elements, resulting in fifteen 4 inch wide elements. The AHOD was made of 3 vertical 12 inch wide counters. The signals from all three down stream hodoscopes were read out with phototubes at both ends, mean-timed and discriminated.

As mentioned at the beginning of the chapter, the entire downstream portion of the spectrometer was mounted on a tilt table which can be set at different angles, thus greatly increasing the momentum acceptance. The ability to set the tilt angle also maintains the flexibility of changing the running energy without having to reset the whole spectrometer. The whole spectrometer can also be rotated around the vertical axis to increase the acceptance of particles scattered by 90 degree in the center of mass frame at different energies.

The side arm consists of three proportional wire chambers, labeled as PWC3, PWC4 and PWC5 respectively in fig. 3.7, with 7 planes. The

wires of all the planes (except one in PWC3, which was a x plane) were oriented at $\pm 30^{\circ}$ from the vertical axis (designated as V and U planes respectively). The distances from the interaction point and the orientations of the chambers were chosen to optimize the acceptances and the resolutions. With the arrangement shown in fig. 3.7, the accuracy in measuring the angles of the recoil particles is about 5 mr.

3.5 The trigger

A fast three stage trigger scheme was implemented in E834 to protect the data acquisition system from overload by the much more copious inclusive interactions in which particles, in general, have lower momenta. The first stage consisted of a coincidence of the "or" ed outputs from each of the four hodoscopes PHOD, TH1, TH2 and AHOD, called 4 out of 4, or 4/4 in short. This coincidence makes certain that there is a particle passing through the entire spectrometer. In the second and third stages, the total momentum and the transverse momentum of the particle were screened against the thresholds built into two trigger matrices, designated as HMAT for the hodoscope matrix, and DMAT for the drift (chamber) matrix, respectively. Only when the momentum and its transverse component of the particle passed these thresholds, was the event accepted. The idea of the matrices for the case of HMAT is shown schematically in fig. 3.9. Since the target is only 2 inches high it can approximately be treated as a point. Therefore, the bending angle, and thus the momentum of the particle, can be determined approximately from the intersection angle between the straight line that connects the TH1 and TH2 hits, and the straight line that connects the target point and the intersection point between the straight line determined by the TH1 and TH2 hits and the central plane of the magnet. Therefore, for a hit in any element of TH1, the requirement that the momentum of the particle be larger than certain value limits the number

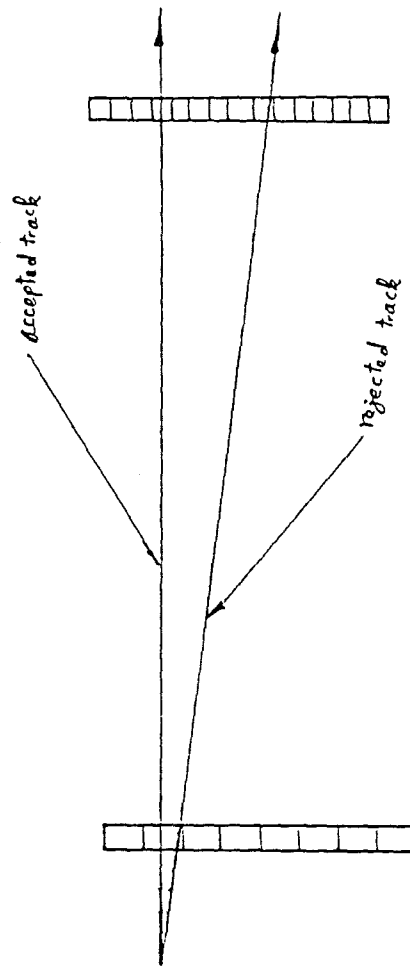


Fig. 3.9 Schematic of the hodoscope trigger matrix.

of acceptable TH2 elements, generally one or two. Proceeding this way for each element we arrive at a 8 by 15 matrix which correlates every TH1 element with the corresponding TH2 elements, and indicates acceptance or rejection of the event. The drift matrix DMAT works exactly the same way as the HMAT, except DMAT uses the wires of the y measuring planes of DWC1 and DWC2, instead of the hodoscope elements. In addition, AHOD elements, which measure x positions, determine the scattering angle. The DMAT trigger thus allows specification of the particle's transverse momentum. For this purpose, the y measuring wires of DWC1 and DWC2 were grouped into cells of 4. The cells from DWC1 and DWC2 were correlated into a 80 by 40 matrix which was then combined with three AHOD elements to form a 3 by 80 by 40 matrix. The actual matrices were generated by Monte Carlo simulations using the idea described above. Before each run the matrices were loaded into a trigger box which was manufactured at the University of Minnesota. The momentum resolution of HMAT was about .4 Gev/c and the transverse momentum resolution of DMAT was about .25 Gev/c. The decision time of HMAT was about 40 ns and the decision time of DMAT was about .4 micro second.

Two additional pre-scaled triggers were implemented in the experiment. One is called 3/4 trigger in which the coincidence of the outputs from any three of the four fast trigger elements was required to initiate an event read out. These triggers were mainly used for

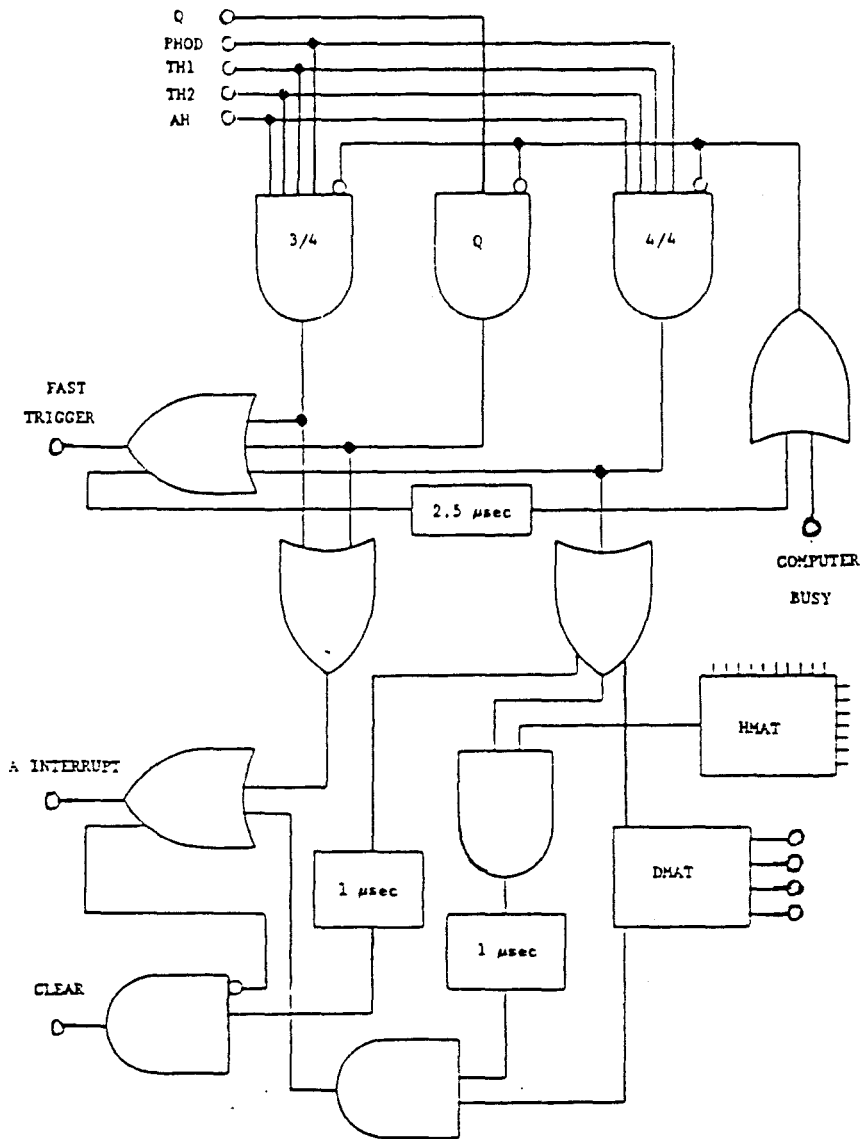


Fig. 3.10 The trigger logic.

trigger called Q trigger was initiated solely by a hit in the Q counter located in front of the target. These triggers were unaffected by the spectrometer trigger selections and were used to check for possible bias in the trigger system. 3/4 and Q triggers were pre-scaled to 10% and 5 % of the total recorded event rate.

The trigger logic is shown schematically in fig. 3.10. Upon occurrence of a 4/4 trigger control signals were sent out to various components of the detector to lock up the data and prepare for a possible event read out. Meanwhile signals from TH1 and Th2 were decoded and compared with HMAT. In the case that the HMAT is satisfied the coincidence output of 4/4*HMAT will be further compared with DMAT which comes in about 1 micro second later. If the comparison is successful a computer interrupt, called A interrupt, would be sent out to the computer and the read out process starts. Any failure in the process would allow the delayed clear signals to pass through and the event buffers would be cleared and the system would be prepared for the next event.

In addition to the event interrupt a second interrupt, called B interrupt, was taken at the end of each spill to read in all the beam information and the scalers.

3.6 The data acquisition

There was a prodigious amount of information to be collected for each event, including data from the scalers, ADC's, TDC's, and latches. The average length of an event block was about 800 bytes. Read in of an event took about 4 ms.

The data acquisition system was built on a PDP 11/60 computer which communicates with the detector through a standard CAMAC serial highway via a Jorway controller. The event interrupts were handled by the PDP 11/60 computer through an interface, called Bison Box developed at Fermilab. A well known program, called MULTI, was used for the data acquisition, data logging, on line event display and on line monitoring of the detector. About 170 6250 bpi data tapes were taken for the whole experiment.

3.6.1 The PWC data acquisition

Signals from a group of 16 adjacent PWC wires were amplified and discriminated by a Lecroy amplifier-discriminator 2735 card, which was mounted on a G10 support board at the chamber. The output signals from the 2735 card were then converted to ECL and transmitted to a latch card where they were converted to TTL, stretched to 100 ns wide and delayed by 250 ns. When the wire signals were in time with a 4/4 gate they were latched and loaded into the shift registers. Each latch card

handled 96 channels of PWC wire signals. 9 such cards and a controller card formed a crate. All the crates were controlled by a master crate controller card MCC, which was located in one of the CAMAC crates. When the event passed the second and third stage trigger, the PDP 11/60 sent a read in signal to MCC to initiate the read in process. The 96 channels of a latch card were arranged in 24 4 wire frames. The read in process proceeded sequentially starting from the last frame in the last crate and working backwards. On each clock cycle MCC took in a frame and a new frame from the latch card being read was shifted into the data path. This clock signal was passed onto the remaining crates in descending order, causing the registers in each crate to shift. When the frame was found empty it was discarded and the frame counter, which counted the number of frames that had been read, was incremented. When the frame contained data, MCC loaded a 16 bit word into a buffer located on MCC. The upper 4 bits of the word contain the hit information and the lower 12 bits the frame address. The process repeated until all the frames were examined. A pre-set bit pattern test signal, called the backfill signal, was then sent through the whole data path and read back. If the read back pattern was different from the one sent in, a backfill error message was issued by MCC indicating that there was some thing wrong in the PWC read in. When the read in process was completed, the PDP 11/60 read MCC buffer into the event block. The whole read in process for the PWC data took about .6 ms.

3.6.2 The DWC data acquisition

The DWC wire signals were amplified and discriminated using the same 2735 cards as were used by the PWC read out system. The ECL outputs were then transmitted to the stretcher cards where they were converted to TTL and stretched to 100 ns wide. Signals from the wires other than the y measuring planes in DWC1 and DWC2 were then converted back to ECL and transported to the drift chamber TDC's. For the wires in the y measuring planes in DWC1 and DWC2, the signals were splitted into 2 branches. One of the branches was treated the same way as the wires in other than the two y measuring planes. The other branch was "or" ed with signals from three other adjacent wires and transmitted to the trigger box to be used for the third stage trigger. The 96 channel Lecroy 2770 modules were used to process the hit and time information for read in by the PDP 11/60.

A large angle quasi elastic scattering off a nuclear target is a very rare occurrence at high energies. A typical 6250 bpi 12 Gev/c incident momentum tape, for example, contained only a few "good" events. About 170 of these tapes were recorded during E834. The majority were recorded at 10 and 12 Gev/c. The total number of quasi elastic events from these tapes amounted only to a few thousands. This data scarcity poses severe challenges for the off line analysis. The most serious problem was distinguishing the quasi elastic events from the background inclusive events that had similar kinematics, e.g., $pp \rightarrow p\Delta$, where Δ decayed into a proton and a soft, undetected π^0 . The problem was compounded by Fermi smearing, which made it impossible to identify elastic events using simple kinematic constraints, such as the ones used in the previous experiments. Other difficulties included multiple interactions within the event gate, caused by the high beam flux which was essential because of the diminutive cross sections; and attenuations of the initial and final state particles due to interactions with the nuclear matter, which reduced the event rate even further. The off line analysis involved unpacking the data blocks; calibrating the TDC constants; aligning the apparatus; reconstructing the tracks; identifying the initial and final state particles; analyzing the kinematics; and ultimately pulling out the interesting

events from the huge number of interactions dominated by inclusive processes.

In the following sections we will briefly describe some of the procedures involved in extracting these rare events from the massive amount of raw data.

4.1 The TDC calibration and alignment

Assuming that the drift velocity v_d is a constant the drift distance d can be related to the raw TDC reading T , through

$$d = (T - T_0)v_d \quad (4.1)$$

in terms of T_0 , the off set of the TDC modules, and v_d , the drift velocity;

or equivalently, through

$$d = \frac{T - T_0}{T_m - T_0} \frac{w}{2} \quad (4.2)$$

in terms of T_0 and T_m , the maximum TDC reading, where w is distance between the two adjacent sense wires.

A set of events, called "straight through's", taken in a special run in which the spectrometer was aligned with the beam and the bending magnet was turned off, was used for calibrating the constants. For operational convenience eq. 4.2 was used. The TDC readings from each plane were plotted for a sub set of the straight through events chosen by requiring one and only one hit in each drift plane. To further

improve the accuracy in determining these constants only those hits which were within the beam profile were included in this analysis. Ideally the plot should be a square. The upper edge would be the T_m and the lower edge would be the T_0 , or the the other way around, depending on whether the common start or common stop was used. However, due to the fact that near the center of the drift cell, the electric field configuration was very complicated, the upper edge of the plots were not quite sharp, as can be seen from a typical plot shown in fig. 4.1. Final adjustments were made by plotting the converted drift distance

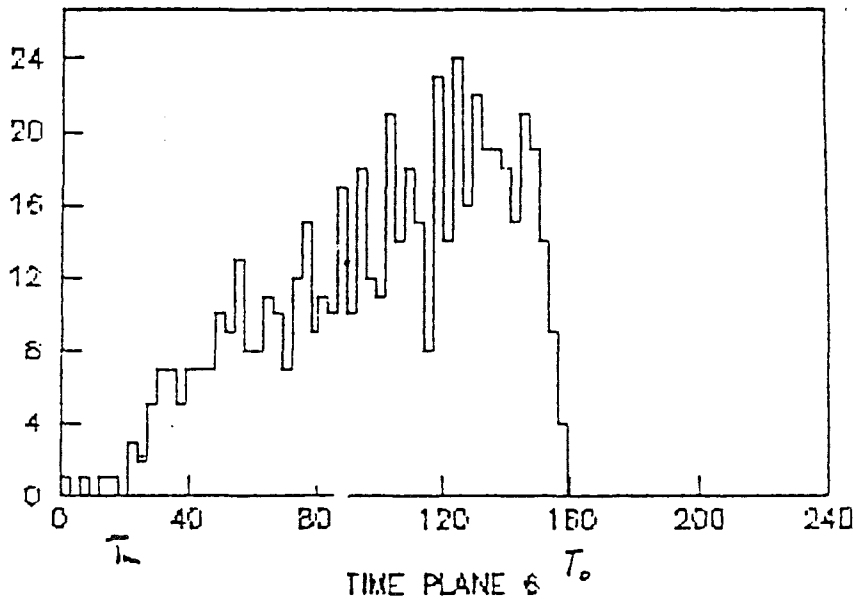


Fig. 4.1 Sample TDC plot

distributions. If there was an excess (depletion) of hits at the large drift distance end indicating that the value for the T_m had been too large (small) it was adjusted accordingly.

Before discussing the details of the alignment, it is appropriate to explain in some detail what needs to be done in the alignment process. As mentioned before, the primary coordinate system was the spectrometer frame. A chamber plane was defined by 6 coordinates: three coordinates to define the position of the origin of the so-called body frame (chosen to be the center of the lowest wire for the y measuring planes or the center of the right most wire in the case of the x measuring planes) and three angles which define the orientation of the plane. All the planes in the spectrometer were either x measuring or y measuring planes. The body frame axes were parallel to the reference frame. The alignment therefore involved adjusting only one coordinate of the body frame origin, e.g., x position of the origin for the x measuring planes. In the following we will generically call the coordinate to be adjusted the x coordinate. Alignment for the spectrometer was straightforward. Using the correct TDC constants, we then reconstructed a pre-selected set of events with the preliminary alignment file from a mechanical survey. The difference $\delta x = x_m - x_p$ was plotted for each event, where x_m was the hit position from the TDC reading and x_p was the hit position projected by the fitted track for which the concerned plane was left out in the reconstruction. If the plane was properly

aligned the δx distribution would be centered at zero. If the δx distribution was off the center, the coordinates of the chamber were adjusted appropriately. This process was iterated till all the chambers were considered properly aligned, i.e., all the residues were centered at zero and the widths were reasonable.

Side chamber alignment was more involved mainly due to the fact that it was impossible to run straight through beam through the side arm. The alignment of the side arm was divided into two stages: the relative alignment among all three side chambers and the absolute alignment of the whole side arm with respect to the reference frame. The relative alignment was accomplished by fitting selected hydrogen elastic events for which there was one good side track. First an arbitrary reference point, chosen to be the origin of PWC3, and the orientation of the first chamber were fixed. The coordinates of the 5 middle planes were allowed to vary and PWC2 and PWC3 were allowed to rotate around the vertical axis to minimize the total chi squared of the fitted tracks. This procedure determines the relative positioning of the last two chambers with respect to the first chamber to a satisfactory degree. In the absolute alignment, the reference point was allowed to change and the entire side arm was allowed to rotate around that point to minimize the total residue between the nominal track, projected by the kinematics from the beam and spectrometer track information, and the reconstructed side track. This step fixed the relative orientation of the side arm with respect to the whole apparatus. It turns out that the

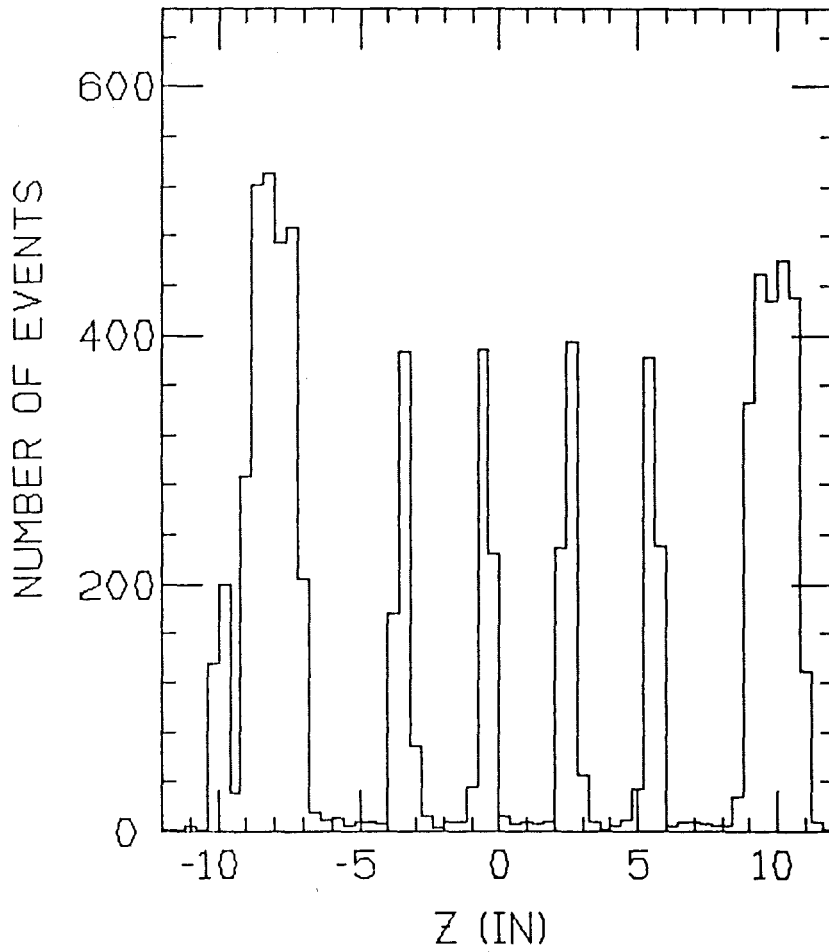


Fig. 4.2 Vertex distribution of the elastic events.

residues weren't sensitive to the displacement of the side arm along the acceptance centroid axis. To fix that deficiency, events with three tracks in the side arm were used for which a vertex could be found from the three tracks. A final polish of the side arm alignment was obtained by varying the plane positions so the residues of the x positions measured and project is centered at zero. Details of the side alignment can be found in (Bla 1986)

To show the quality of the alignment a sample plot of the vertex distributions for 6 Gev aluminum runs is shown in fig. 4.2 where the target segment positions are resolved very clearly.

4.2 The event reconstruction

The huge amount of the raw data and the fact that we were interested primarily in the quasi elastic events made it necessary and possible to employ a stepwise procedure in selecting and reconstructing the events. The procedure started with selecting events with a possible single track in the spectrometer. This was accomplished by requiring that there be enough planes with at least one hit and a limited number of planes with more than one hit in both arms. The spectrometer hits for the pre-selected events were then reconstructed and the transverse momentum calculated. When the transverse momentum was larger than the value set for the run, the procedure then proceeded to reconstruct the side arm. To further reduce the reconstruction time only the events with a limited multiplicity in the side arm were reconstructed. This way substantial reconstruction time was saved.

To derive a set of appropriate cuts for the pre-selection process a few runs were studied in detail. All events in these runs were fully reconstructed. The parameters required by the pre-selection process were plotted for the quasi elastic event candidates. The resulted cuts are list in table 4.2. The pre-selection reduced the data to less than 5% of the original amount. The loss of the quasi elastic events introduced by these cuts was estimated to be less than 3% of the total number of quasi elastic events.

In E834 the beam track was taken nominally to be along the z axis.

Table 4.1 The pre-selection cuts

min planes with hits		
	up stream	4
	down stream	6
	side arm	4
max planes with mult hits		
	up stream	3
	down stream	4
	side arm	
	6 Gev	4
	10 Gev	7
	12 Gev	7
P_t		
	6 Gev/c	1.2/c
	10 Gev/c	1.6/c
	12 Gev/c	1.8/c

The event reconstruction therefore involved only the spectrometer and side tracks. The algorithm for the reconstruction was designed to reconstruct 1 or 2 spectrometer tracks and 1, 2, or 3 side tracks. In the following we will go through each of the steps in event reconstruction.

4.2.1 The spectrometer reconstruction

The spectrometer reconstruction started with the track recognition. Each event was scanned for sufficient hits to initiate the reconstruction process. At least one y hit was needed in each chamber in the spectrometer arm to be able to determine the momentum of the particle. At least three x measuring planes with hits were required in the four chambers to unambiguously determine a track. The algorithm then proceeded to search for primitive x, up stream y and down stream y track segments, where by an x track segment we mean the projection of a track onto the xz plane, and similarly, by a y track segment we mean the projection onto the yz plane. The search process starts by taking a hit from the first plane that has a hit and tries to associate it with hits in other planes. The x (y for the y segments) and z coordinate of these hits were used to construct the primitive track segments. For the x and up stream y track candidates to be accepted, they were required to project into the magnet and to the target region. The down stream segments were required to project into the magnet. This process continues until all the hits were searched and examined. If the program failed to find at least one segment in each of the three projections the reconstruction was abandoned. Next the program tried to correlate the up stream y track segments with the down stream ones by projecting them into the center of the magnet. When the projected y coordinates were within 1 inch of each other, and the resultant momentum was

$(DY/DZ)_2$ y slope of the track down stream

These were most natural and convenient parameters for us because then, the scattering angle could be found simply from the upstream slopes and the bending angle was the difference between the two y slopes.

The basic idea of the track fitting process can be easily understood with the help of fig. 4.3, where a simplified two dimensional y projection of a track configuration is shown. The vector \vec{X}' , position of the point in the wire plane where the reconstructed track intersects

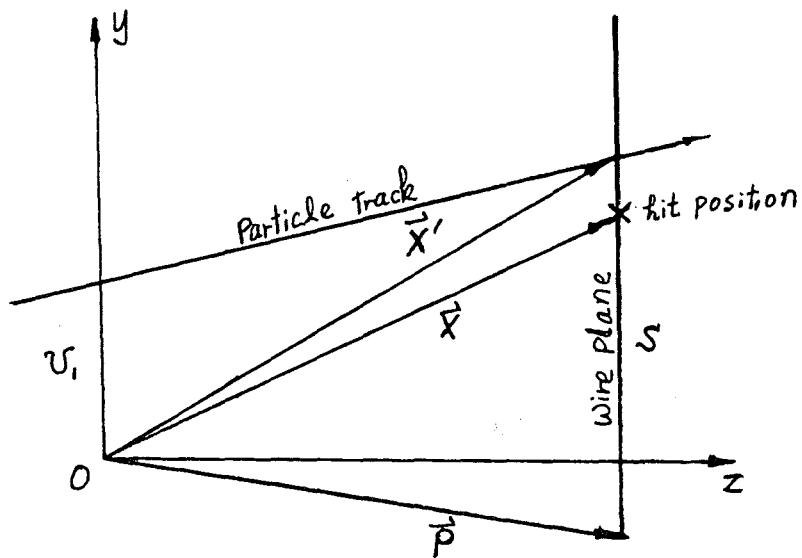


Fig. 4.3 The track fitting schematic.

the plane, can be described by a vector $(0, y_0 + \frac{dy}{dz}z, z)$ in terms the track parameters y_0 , $\frac{dy}{dz}$ and the known quantity z and the position of

the hit \vec{X} can be expressed in terms of \vec{P} , the position of the origin of the body frame (chamber frame) in the spectrometer frame, and \vec{s} , the position of the hit in the body frame. The purpose of the track fitting process is to find correct values for the parameters so

$$\begin{aligned} \vec{X}' &= \vec{X} \\ &= \vec{P} + \vec{s} \end{aligned} \tag{4.3}$$

Denote the unknown parameters by a generalized vector $v = (v_1=X,$

$v_2=\frac{dx}{dz}, v_3=Y, v_4=(\frac{dy}{dz})_1, v_4=(\frac{dy}{dz})_2)$ and take a dot product of both

sides of eq. 4.3 with the appropriate body directional unit vector $\vec{u} = (u_1, u_2, u_3)$ we, for the case shown in fig. 4.3, arrive at a expression involving the component of the body frame directional vector u 's and the unknown parameters:

$$u_2 v_3 + u_2 v_4 z = \vec{u} \cdot \vec{P} + s - u_3 z \tag{4.4}$$

For each on-track hit we can derive a similar expression relating the components of v and the known quantities. From these equations we can then solve for the unknown parameters. It is clear that the minimum number of hits must be greater or equal to the number of parameters. In the case where the number of hits is larger than the number of parameters the fitting process can be constrained since all the equations derived from the on-track hits are consistent. Putting the equations in a more concise matrix form the track fitting process then amounts to solve the following matrix equation for V :

$$A \cdot V = B \quad (4.5)$$

where A , B are known matrices. In terms of components:

$$A_{jk} V_k = B_j \quad (4.6)$$

where j is the hit counter and k is the parameter counter. For the case shown in the fig.4.3 the components are:

$$A_{j3} = u_2 \quad A_{j4} = u_2 z \quad B_j = \vec{u} \cdot \vec{P} + s - u_3 z \quad (4.7)$$

where j stands for the sequential number of the hit shown in the figure in the hit list of the track. However, due to the fringe fields and

other inaccuracies the equations were not truly linear so the track fitting process was iterative: starting with a less well fitted track with certain number of hits on it, the program then projects the fitted track onto each wire plane and calculates the position of the interception point; the distance from the interception point to the nearest hit in that plane will be compared with a pre determined convergence criteria; if the distance is smaller than the preset value, the hit will be counted as on the track, likewise if the distance from an on-track hit to the interception point is found to be larger than the preset value, it will be dropped from the track; the process continues until either no changes are found or the maximum number of iterations is reached. The fitting process started with the primitive tracks. In the first pass the drift time information was not used and each hit was tried twice assuming the hit was to the left and right of the wire, respectively. On the ensuing passes the closest hit was chosen and the convergence criteria was progressively improved. The effects of the fringe field and other inhomogeneities of the magnet were corrected for by a special routine in terms of a displacement of the track intersection point and an offset in the slope vector. These corrections were found by observing the discrepancies between the down stream segment estimated from the up stream segment and the known momentum of the particle, and the actually observed down stream segment. Details of the spectrometer reconstruction can be found elsewhere (Bal 1987).

4.2.2 The side arm reconstruction

The side arm reconstruction algorithm was designed with the ability to reconstruct three, two, or one tracks. The reconstruction process starts similarly with associating the u and v hits into primitive tracks. The program then tries to correlate the u v track segments into possible tracks. The x hits were used in a similar way as the v hits were used in the spectrometer reconstruction. The algorithm begins by trying for a three track reconstruction and works down towards small track multiplicities. If the three track attempt fails, the program then attempts a two track reconstruction, and if that also fails, the algorithm will then try for the one track reconstruction. The information obtained in each step was passed to the next. A vertex between the target and the first chamber was required for the two and three track reconstruction to be successful. Details of the side arm reconstruction are given in (Bla 1986)

4.3 The particle identification

4.3.1 The beam identification

The outputs of the ring phototubes of the beam Cherenkov counters were latched and the time information was recorded by fast TDC's. The identification of a beam particle involved the the latches and the TDC's. A ring was considered fired if there were more than three phototubes with coincident outputs out of the total of six. Because of the high beam flux, the time information was crucial in reducing the effects of the spurious signals. In particular, such signals were often produced by the particles following the scattering particle. For this purpose, the arrival time and the width of each ring was studied in detail using good samples of elastic events. In the off line analysis, the rings with signals were tagged, according to how well their arrival time matched with the pre-determined values, by 1 (good match), 0 (ambiguous), -1 (late). When more than one ring was available for identifying the same particle their information was combined (or ed). The functions of the rings at each energies was listed in Table 3.2 and the truth logic is summarized in Table 4.2 in which P π and K represent the proton, the pion and the kaon rings respectively. The status is described by "early" (meaning the time of the ring was early with respect to the nominal particle arrival time), "late" (meaning late arrival) and "outside" (meaning the arrival time either early or

Table 4.2 The truth table for the beam identification

P	π	K	identification
early	good	-	π
	outside	good	K
	late	late	P
	early or early		none
late	outside	good	K
	early	outside	π
	late	outside	none
	good	good	none
	good	outside	π
good	good	-	none
	outside	good	none
	outside	outside	P

late with respect to the nominal time). Since the beam gate was much wider than the ring phototube resolutions, there could be early time block. If a ring status was early, there could be an on time particle that was blocked. However a late status usually means that there wasn't an on time particle in that ring. Thus, a particle could be identified as a proton if the proton ring was on time and the pion and kaon rings were outside; or if the proton ring was early and both the pion and kaon rings were late. On the other hand, if any two or all of the three rings were early or good, the particle would be un-identified. In addition, it was assumed that the kaon ring could not block a kaon because the fraction of the kaons in the beam was very small.

As was pointed out before there was appreciable amount of protons being mis-identified as pions. At 6 Gev/c, where the pions could be separated from the protons by kinematic considerations in the software, the fraction of mis-identification of the pions was found to be about 30%, i.e., 30% of the identified pions were actually protons.

4.3.2 The spectrometer particle identification

The outputs from the photomultipliers of the spectrometer Cherenkov counters were also latched. The software identification of the spectrometer particles was fairly simple. If any of the counters fired within the event gate, the event was counted as a pion, otherwise it was counted as a proton. Since there were very few kaons in the beam (and thus very few in the spectrometer) the kaon identification wasn't used.

4.4 The event identification

One important feature of E834 was that the elastic (from now on we will refer to the nuclear quasi elastic scattering as elastic scattering for convenience with the understanding that whenever nuclear elastic scattering is used it means quasi elastic scattering) hadron proton scattering off hydrogen and nuclear targets were observed simultaneously. This way the normalization problems that invariably arise from having to measure absolute cross sections were avoided and the systematic errors were greatly reduced. It is in this spirit that the off line analysis procedures were designed such that the whole analysis program doesn't distinguish between the hydrogen and the nuclear events until the very end, where a simple cut on the target positions was used to separate the two type of events.

To extract a set of events with distinctive characteristics from the data, the first step is to choose a set of variables which have distinct values for the desired set of events. For example, in the hydrogen scattering experiment, one usually chooses variables such as the coplanarity, which measures the degree of deviation of the beam track, the spectrometer track and the side arm track from defining a single plane, or the opening angle, which is the angle between the spectrometer and the recoil particles. To within the experimental errors, these variables distribute over some narrow range for the fixed angle elastic scattering events, while for the inclusive background,

they distribute smoothly over some large range depending on the range of allowable missing momentum. These quantities are independent. Putting constraints on one of them will not limit the range of the other, which is important property of a variable used for cuts. However these variables can not be used for the selection of the elastic events in interactions involve nuclei because their values are not sharply distinct in this case due to Fermi smearing. Furthermore, the two variables are not orthogonal for nuclear targets in the operational sense because, in general, events with larger deviation in the opening angle also tends to have a larger coplanarity value so constraints on one of these variables will also limit the scope of the other. After some grouping, we realized that the best variable in the nuclear case is the apparent Fermi momentum. The word apparent is used here because the quantity can be regarded as the the Fermi momentum only in operational sense even for elastic events. This apparent Fermi momentum is defined by:

$$\vec{p}_b + \vec{p}_f = \vec{p}_s + \vec{p}_r \quad (4.8)$$

where \vec{p}_b is the beam momentum which is known, \vec{p}_s is the momentum of the spectrometer particle which is measured, \vec{p}_r is the momentum of the recoil particle which can be deduced by assuming that the interaction

was a elastic scattering, and \vec{p}_f is the unknown Fermi momentum. To within the experimental error \vec{P}_f is the Fermi momentum of the target particle for genuine elastic scattering events. However for false elastic events \vec{p}_f could be any value determined by the missing momentum of the process. Therefore the variable is useful for the selection of elastic events. Furthermore, if we project \vec{p}_f into a appropriate coordinate system the components are orthogonal. The frame we chose is the beam frame, i.e., the origin was at the center of the target, the z axis was the beam axis, the y axis is the axis normal to the scattering plane and the x axis was given by the right handedness. This frame has the advantage that the y component is perpendicular to the scattering plane which makes it less likely to be affected by the possible alignment errors. For hydrogen elastic events we expect \vec{p}_f components to peak at zero, while for nuclear elastic events we expect they will spread into a broad peak centered at zero.

Even though the on-line trigger provided some degree of suppression to the background interactions, the trigger selection conditions were intentionally loose that the interactions recorded were still dominated by background events. To sort out the rare elastic scattering events, various off-line selection conditions, called cuts, have to be used in the data analysis. The cuts used in E834 included:

geometrical,

$-12.5 \text{ inches} \leq z_{\text{vetex}} \leq 12.5 \text{ inches}$ (target region)

one and only one track in the spectrometer

one and only one track in the recoil arm

$\chi^2/\text{DOF} \leq 5$. for the spectrometer track

$\chi^2/\text{DOF} \leq 5$. for side track

number of off track hits ≤ 8

number of hits in the target veto ≤ 2 in either side

Kinematic

$p_t \geq$ value specified by the kinematics smeared by Fermi

motion

\vec{p}_f components are less than k_f , the Fermi momentum for the particular target.

particle species

and the interaction position that distinguishes the hydrogen from the nuclear target.

The most important cut to the identification of the elastic signals

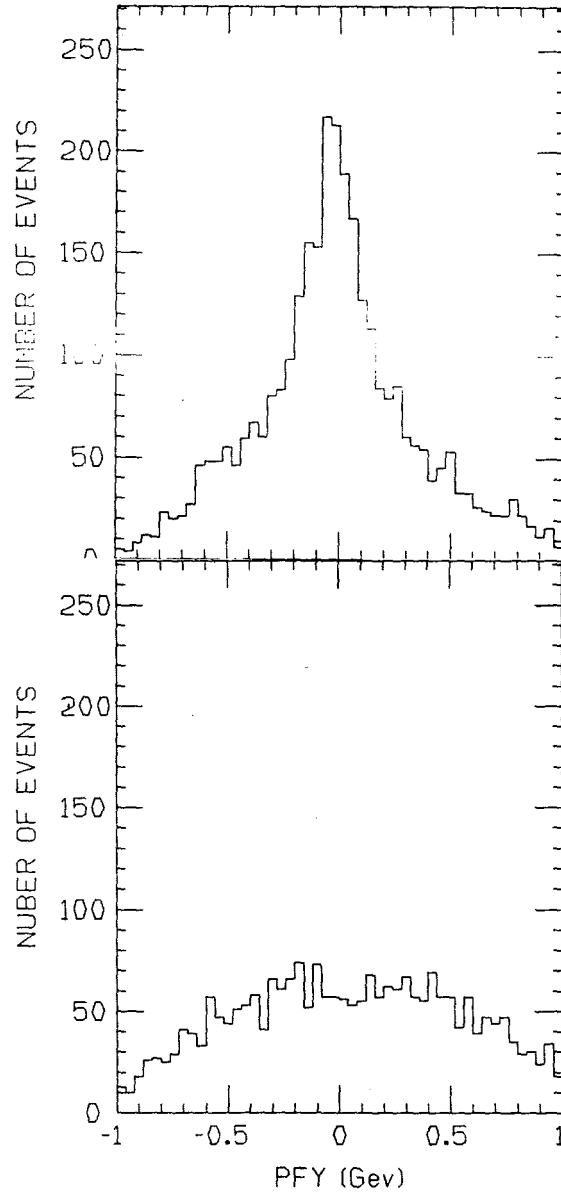


Fig. 4.4 P_{fy} distribution of the quasi elastic events from the Al target at 6 GeV, a) the veto cut on, b) the veto cut off.

is the veto counter cut. Its effectiveness can be easily seen from fig. 4.4, where the p_{fy} distribution for the 6 Gev aluminum data is plotted for the cases of without, and with two or more veto counters fired. As can be seen from the plots, the signal stands out unmistakably when the veto counter cut is imposed. By comparison, the reconstructed y component of Fermi momentum for the background events smoothly distributes over the whole region as expected. By subtracting the apparent background from the apparent signal with appropriate normalization to make sure that there are no events at the very large momentum region after the subtraction, we were able to obtain apparently clean elastic signals.

The hydrogen signals sticks out sharply in the finely binned p_{fz} plot as shown in fig. 4.5 again for the case of the 6 Gev aluminum. It is worth noting that the corresponding p_{fy} plot was much broader due to the beam dispersion in the y direction.

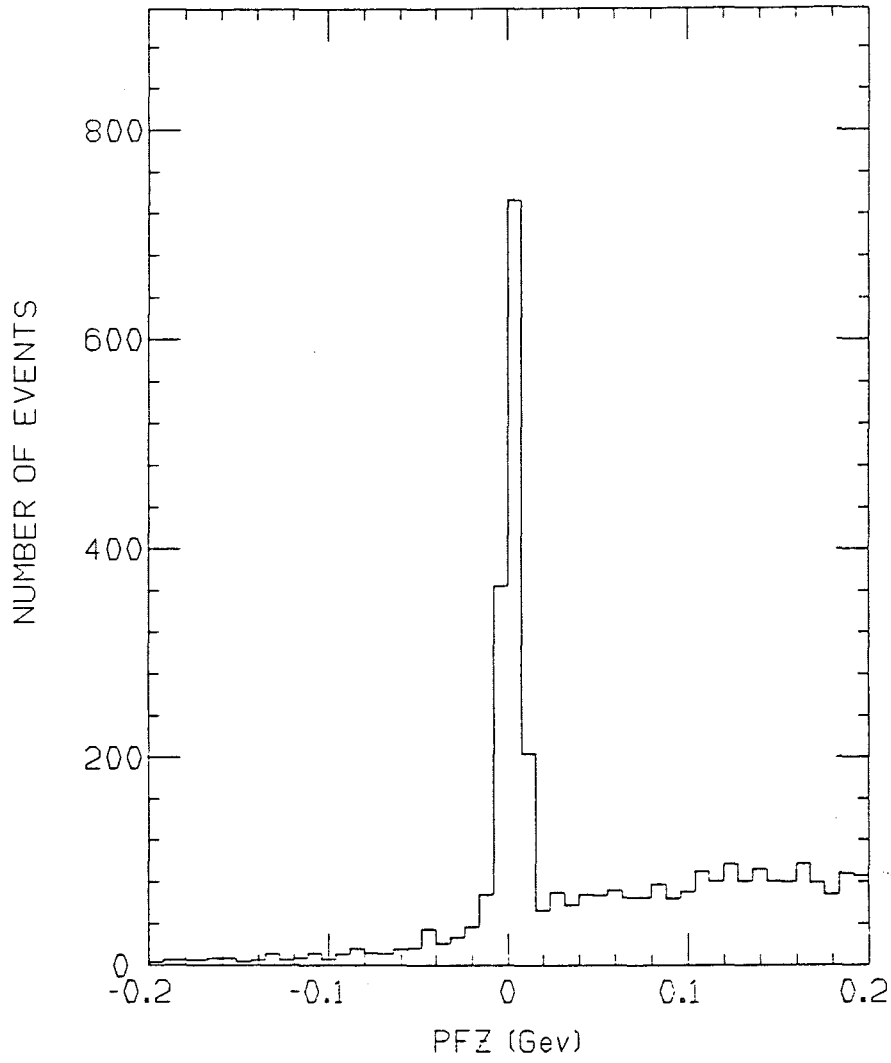


Fig. 4.5 P_{fz} distribution of the quasi elastic events from the polyethylene target.

Chapter 5. The results and discussions are presented in an appendix to the main report. Having the purified samples of the elastic scattering events we are now ready to present these events in a more physical context. The data to be reported here include:

- PP and π P elastic scattering off Li, C, Al, Cu, Pb targets at 6 Gev
- PP and π P elastic scattering off Li, C, Al, Cu, Pb targets at 10 Gev
- PP elastic scattering off C and Al targets at 12 Gev

The data will be presented in connection with two inter-related topics: the color transparency of nuclear matter to the hard scattered hadrons and the Fermi spectra of the nuclei. In section 5.1 the definition of the nuclear transparency and the procedures for extracting it from the data will be presented. Then the transparency for the afore mentioned targets will be presented. In particular, the transparency for Al and C targets will be presented as a function of the effective scattering energy, which can be different from the beam energy because of the Fermi motion of the target protons. To gain some idea on to what extent the data proves the hypothesis of color transparency, the variations of the transparency as a function of A (the mass number of the nucleus) will also be presented and comparisons of the data with the predictions of the Glauber model and some guessed expansion models will be given. The results will be discussed in conjunction with a discussion of Perturbative Quantum Chromodynamics and some recently developed ideas. A some what extensive report on the

errors and uncertainties in the data and in the procedures used to derive the transparency will be given at the end of section 5.1. . Section 5.2 will be devoted to presenting and discussing the data on Fermi spectral functions.

5.1 The proton transparency.

5.1.1 General description

The transparency of a particular type of nuclear matter, denoted by T , is defined as :

$$T(s) = \frac{(\frac{d\sigma}{dt})_N}{(\frac{d\sigma}{dt})_H} \quad (5.1)$$

where $(\frac{d\sigma}{dt})_N$ denotes the differential cross section of the proton scattering off the protons from that medium, and $(\frac{d\sigma}{dt})_H$ denotes the cross section of the proton scattering off the protons from the protons in the polyethylene target.

Eq. 5.1 can be rewritten as:

$$T(s)(\frac{d\sigma}{dt})_H[s_0] \frac{(\frac{d\sigma}{dt})_H[s]}{(\frac{d\sigma}{dt})_H[s_0]} = (\frac{d\sigma}{dt})_N[s] \quad (5.2)$$

Putting in the Fermi distribution for the medium $f(p_f)$ we have:

$$dp_f f(p_f) T(s) (\frac{d\sigma}{dt})_H[s_0] \frac{(\frac{d\sigma}{dt})_H[s]}{(\frac{d\sigma}{dt})_H[s_0]} = dp_f f(p_f) (\frac{d\sigma}{dt})_N[s] \quad (5.3)$$

Multiply both sides by the beam flux and take into account of the fact that there might be changes in the acceptances due to the Fermi smearing we then have:

$$dp_f \epsilon f(p_f) T(s) (dN/dt)_H \frac{(d\sigma/dt)_H [s]}{(d\sigma/dt)_H [s_0]} = \frac{n_H}{n_N} dp_f f(p_f) (dN/dt)_N [s] \quad (5.4)$$

where n_H and n_N are the number of protons from the hydrogen and the nuclear targets respectively, ϵ is the ratio of the acceptance of the nuclear elastic events to the acceptance of hydrogen elastic events.

As was pointed out earlier, to the lowest order approximation, s doesn't depend on the transverse components of the Fermi momentum, so we can integrate over them to arrive at:

$$dp_{fz} \epsilon f(p_{fz}) T(s) (dN/dt)_H \frac{(d\sigma/dt)_H [s]}{(d\sigma/dt)_H [s_0]} = \frac{n_H}{n_H} dp_{fz} f(p_{fz}) (dN/dt)_N [s] \quad (5.5)$$

If we now integrate over t , over the angular range of the detector and choose some p_{fz} interval in which $T(s)$ can approximately be regarded as a constant, we then have:

$$T(s) \int_a^b dp_{fz} \epsilon f(p_{fz}) \frac{(d\sigma/dt)_H [s]}{(d\sigma/dt)_H [s_0]} = \frac{n_H}{n_N} \frac{N_N}{N_H} \quad (5.6)$$

where N_H is the total number of the elastic events from the hydrogen target and N_N is the number of the elastic events from the nuclear target, for which p_{fz} lies within the limits of integration, i.e., $a \leq p_{fz} \leq b$. Therefore, the problem of extracting the transparency,

averaged over the energy range given by the p_{fz} interval, reduces to:

(1) counting the number of elastic events from the nuclear target, for which the longitudinal component of the Fermi momentum p_{fz} is required to be within the limits of integration (some region over which the transparency is approximately constant); (2) counting the total number of elastic events from the hydrogen target; (3) correcting for the effects caused by the variation of the cross section for pp elastic scattering, as a function of s ; (4) correcting for the possible changes in the acceptance of the apparatus due to the Fermi smearing; (5) correcting for the differences in the total number of protons in the nuclear and the hydrogen targets.

To derive the correction factors we need know both the Fermi distribution $f(p_f)$ for the medium and the pp elastic scattering cross section as a function of s . For the cross section, there exists quite extensive data which could be used. On the other hand, reliable data on

the Fermi distributions, including the high momentum tail regions, are almost non existent. Therefore, we have to choose one of the two approaches available: to use our own observed distributions, or to use some model, extrapolated from the existing data. Both methods have been used in analysing the data. The main difference from the two analyses is the overall normalization, which causes a overall shift in the transparency that is roughly independent of the energy. Here we will present the analysis using a model due to E. J. Moniz (Bod 1981) in which a high momentum tail, based on calculations of nucleon-nucleon correlations in nuclear matter, was added to the Fermi sphere discussed earlier derived from the low energy electron quasi elastic scattering data. This model was used by A. Bodek et al. in deriving the corrections due to the Fermi motion for the structure functions measured for nucleons. The model is defined as:

$$f(p_f) = \frac{1}{c} \left(1 - 6 \left(\frac{k_f a}{\pi} \right)^2 \right) \quad 0 \leq p_f \leq k_f$$

(5.7)

$$f(p_f) = \frac{1}{c} \left[2R \left(\frac{k_f a}{\pi} \right)^2 \left(\frac{k_f}{p_f} \right)^4 \right] \quad k_f \leq p_f \leq p_0$$

where p_f is the amplitude of the momentum and

$$a = 2 \text{ Gev}^{-1}$$

$$c = \frac{4k_f^3}{3}$$

$$R = \frac{1}{1 - k_f/p_0}$$

where p_0 is some cut off momentum beyond which the distribution

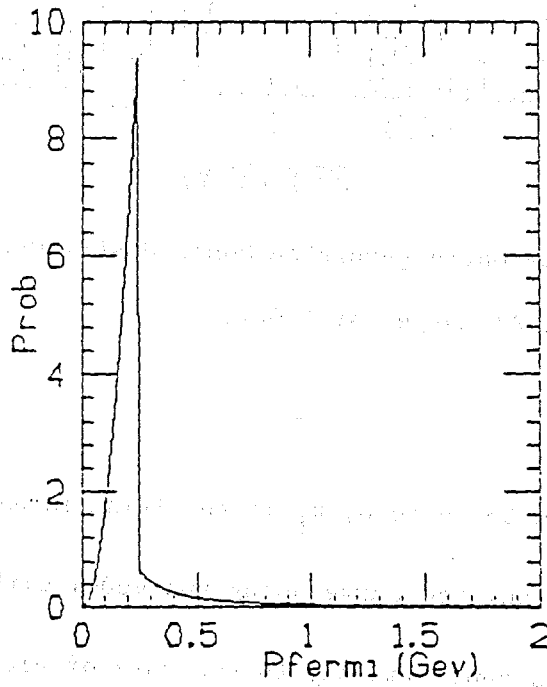


Fig. 5.1 The Moniz distribution.

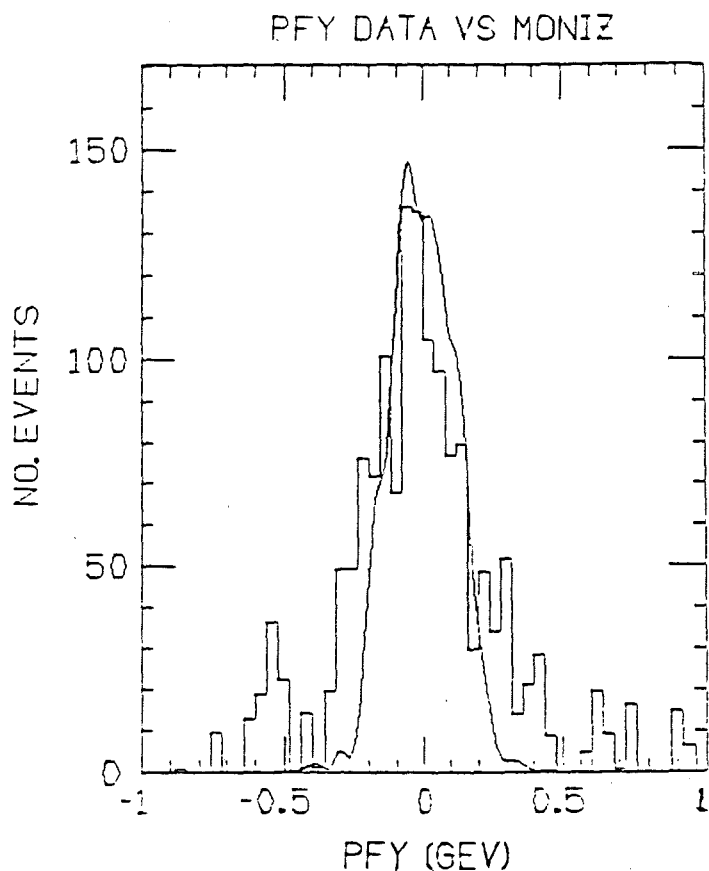


Fig. 5.2 Monte Carlo generated Moniz distribution comparing with the data from the Al target at 6 Gev.

function is taken to be zero, k_f is the Fermi momentum of the target.

Fig. 5.1 is a calculated curve using the model with a k_f of .25 Gev

which corresponds approximately to the case of aluminum. Fig. 5.2 shows

a Monte Carlo curve generated using the model together with our data

curve for an Al target (this plot is of the y component of the Fermi

momentum which is least affected by the experimental inaccuracies.). The plots reveal that our data shows a substantially higher tail than the model. The question is whether the increase is real or is due to some kind of kinematic effect. Some obvious questions can be raised. For example, how big an effect does the off-shell scattering have on the tail? How will the binding and the recoil of the remnant nuclear system affect the distribution in the tail region? How many of the tail events can be attributed to the remnant Glauber elastic final state interactions? Some of the questions will be discussed latter in conjunction with the discussions of the uncertainties of the data or in conjunction with the spectral function studies. Here we want only to point out the following:

The central region of the observed spectral distribution agrees with the Moniz model quite well, i.e., the central part of the spectral function can be described by a hard Fermi sphere (the central part of the Moniz model is a Fermi sphere).

The apparent tail in the observed spectral function is about 20% higher than what given by the Moniz model. Thus there could be a 20% or so shift when the two Fermi distributions are used to derive the correction factors for the transparency. The difference introduced in the transparency will be of the form of a overall normalization which is roughly independent of the energy. However, the shift does depend on the target material, since the tail amplitude of the distribution depends on that material.

The apparent enhancement in the tail region of our observed spectrum could be due to kinematic factors.

The actual derivation of the correction factors were done by Monte Carlo simulation. The details of the simulations will be given in Appendix 2. Here we will briefly outline what is involved in deriving the correction factors. As can be seen from Eq. 5.6 the quantity we want to find is the following integral:

$$I = \int_a^b dp_{fz} \epsilon f(p_{fz}) \frac{(d\sigma/dt)_H [s]}{(d\sigma/dt)_H [s_0]}. \quad (5.8)$$

Here f is some normalized distribution function, whose central part we know fairly well. The cross section as a function of p_{fz} is also known. The most straightforward way of obtaining the result of the integral is simulating the entire spectrum. The problem of finding I then reduces to simply counting the events within the range concerned and dividing the total by the corresponding number of events over the whole spectrum when the cross section enhancement factor is taken out. In practice however, this is not feasible for two reasons: one, the tail part of the distribution is not known well as was pointed out earlier, two, it is not economical to fully generate the tail since the simulated distribution would then be overwhelmed by the tail which is outside the acceptance of our detector, due to the rapid rise of the elastic cross

section as the effective energy decreases (large positive p_{fz} corresponds to low effective energy). What we did was to generate the central part of the spectrum, i.e., the hard sphere part in the Moniz model. The procedure of deriving I for any interval within the sphere goes the same way as before, i.e., counting the number of events that fall into the interval with the cross section enhancement and divide it by the total number of events over the whole sphere region when the cross section factor is taken out. The only change from the full spectrum simulation case is that now we have to divide I by an overall normalization factor which is the fraction of the area under the hard sphere part to the whole area under the distribution curve which is 1. For the cross section factor, we simplified the simulation process by including only the power law part in the Monte Carlo program and leaving the oscillatory part as a separate parameter which will be taken into account when we calculate the transparency. The effect of the detector acceptance and other inefficiencies are automatically included by running the simulated events through the same analysis procedures as were used by the real data. To summarize, the correction takes the form of three constants: γ_1 , the cross section enhancement due to Fermi motion of the target proton integrated over the p_{fz} range concerned, γ_2 , the ratio of the pp cross section, after the power function factor is taken out, at the effective energy that corresponds

to the p_{fz} concerned to that at the nominal beam energy, γ_3 , the overall normalization factor introduced due to the fact that the simulation process generates only the central part of the spectrum. The corrected transparency T is related to the raw transparency T_r , the ratio of the number of events within the p_{fz} interval to the total number of hydrogen events, by:

$$T = \frac{T_r}{\gamma_1 \gamma_2 \gamma_3} \quad (5.9)$$

For convenience the ratio of the number of hydrogen protons to the number of protons from the nuclear target was included in γ_3 . γ_2 was only used for the case where we broke the observed spectra into several sub-regions of p_{fz} , which corresponded to different effective beam energy, in hopes of obtaining a detailed picture on how the transparency varies with the energy. It should be pointed out that in the raw event counting, we counted only the events within the central sphere in accordance with the Monte Carlo procedure.

For the proton transparency analysis the data on different targets were processed in two different ways depending on the amount of data accumulated. For the Al and C targets the statistics were high enough so the data were analysed by dividing the p_{fz} distribution into 4

regions. The number of raw events in each region together with the corresponding correction constants for the Al target are listed in Table 5.1 through 5.3 for the cases of 6, 10 and 12 Gev respectively.

In these tables N_h is the number of events from the hydrogen target and N_n (-0.25 - 0.25) is the number of events from the nuclear target within the p_{fz} interval from -0.25 Gev/c to 0.25 Gev/c which, compared to the sub-interval counting, gives some idea on the accuracy of the event counting process. The errors listed include only the statistical errors. It should be pointed out that there is about 25% or so uncertainty, which is target dependent but approximately energy independent, in the transparency for each target due to the uncertainty in the spectral function. As was pointed out earlier the asymmetry in p_{fz} distribution is due to the rapid rise of the cross section as the decreasing effective energy. The similar list for the C target is shown in Table 5.4 through 5.6. For the rest of the targets the analysis were done selecting only events within a range of $-.15 \text{ Gev} \leq p_{fz} \leq .15 \text{ Gev}$. The results are listed in Table 5.7 and Table 5.8 for the cases of beam energy of 6 and 10 Gev respectively. The spectra functions will be shown in section 5.2 when we discuss the spectral studies.

Table 5.1 Event distribution over p_{fz} for pp scattering off Al target at 6 Gev

	p_{fz} (Gev/c)			
	-0.15--0.05	-0.05-0.05	0.05-0.15	0.15-0.25
no. of events	63	272	493	340
T_r	0.05	0.22	0.39	0.27
γ_1	0.23	1.	2.1	1.6
γ_2	0.95	1.	0.96	0.91
γ_3	1.4	1.4	1.4	1.4
T	0.16 \pm 0.021	0.16 \pm 0.009	0.14 \pm 0.006	0.14 \pm 0.007

$$N_h = 1259$$

$$N_n(-0.25 - 0.25) = 1194$$

Table 5.2 Event distribution over p_{fz} for pp scattering off Al target at 10 Gev

	p_{fz} (Gev/c)			
	-0.15 - -0.05	-0.05 - 0.05	0.05 - 0.15	0.15 - 0.25
no. of events	60	235	360	310
T_r	0.10	0.41	0.63	0.54
γ_1	0.21	1.	2.1	2.2
γ_2	1.3	1.	0.83	0.78
γ_3	1.4	1.4	1.4	1.4
T	0.28 \pm 0.037	0.29 \pm 0.019	0.26 \pm 0.014	0.23 \pm 0.013

$$N_h = 575$$

$$N_n(-0.25 - 0.25) = 980$$

Table 5.3 Event distribution over p_{fz} for pp scattering off Al target at 12 Gev

	p_{fz} (Gev/c)			
	-0.15 - -0.05	-0.05 - 0.05	0.05 - 0.15	0.15 - 0.25
no. of events	6	45	89	70
T_r	0.036	0.27	0.53	0.42
γ_1	0.23	1.	2.0	1.7
γ_2	0.91	1.	0.86	0.68
γ_3	1.4	1.4	1.4	1.4
T	0.13 \pm 0.051	0.19 \pm 0.029	0.22 \pm 0.024	0.27 \pm 0.032

$$N_h = 167$$

$$N_n (-0.25 - 0.25) = 189$$

Table 5.4 Event distribution over p_{fz} for pp scattering off C target at 6 Gev

	p_{fz} (Gev/c)			
	-0.15 - -0.05	-0.05 - 0.05	0.05 - 0.15	0.15 - 0.25
no. of events	43	221	409	279
T_r	0.063	0.32	0.60	0.35
γ_1	0.19	1.	2.1	1.4
γ_2	0.95	1.	0.96	0.91
γ_3	1.3	1.3	1.3	1.3
T	0.26 \pm 0.04	0.25 \pm 0.016	0.23 \pm 0.011	0.21 \pm 0.013

$$N_h = 687$$

$$N_n (-0.25 - 0.25) = 934$$

Table 5.5 Event distribution over p_{fz} for pp scattering off C
target at 10 Gev

	p_{fz} (Gev/c)			
	-0.15 - -0.05	-0.05 - 0.05	0.05 - 0.15	0.15 - 0.25
no. of events	67	357	624	519
T_r	0.077	0.41	0.71	0.59
γ_1	0.21	1.	2.2	2.2
γ_2	1.25	1.	0.83	0.78
γ_3	0.95	0.95	0.95	0.95
T	0.30 ± 0.037	0.43 ± 0.023	0.41 ± 0.016	0.37 ± 0.016

$$N_h = 875$$

$$N_n (-0.25 - 0.25) = 1620$$

Table 5.6 Event distribution over p_{fz} for pp scattering off C target at 12 Gev

	p_{fz} (Gev/c)			
	-0.15 - -0.05	-0.05 - 0.05	0.05 - 0.15	0.15 - 0.25
no. of events	10	56	107	82
T_r	0.060	0.34	0.64	0.49
γ_1	0.23	1.	2.0	1.7
γ_2	0.91	1.	0.86	0.68
γ_3	0.95	0.95	0.95	0.95
T	0.31 \pm 0.097	0.35 \pm 0.047	0.39 \pm 0.038	0.46 \pm 0.051

$$N_h = 167$$

$$N_n (-0.25 - 0.25) = 283$$

Table 5.7 No. of events within the central region ($-0.15 < p_{fz} < 0.15$)

for pp scattering off all targets at 6 Gev

Target	N_h	N_n	T_r	γ_1	γ_2	T
Li	504	974	1.9	0.88	5.4	0.41 \pm 0.013
C	687	673	0.98	0.97	3.9	0.26 \pm 0.01
Al	1259	828	0.66	1.1	3.3	0.18 \pm 0.006
Cu	580	251	0.43	1.2	3.9	0.098 \pm 0.006
Pb	330	56	0.17	1.2	3.9	0.038 \pm 0.005

Table 5.8 No. of events within the central region ($-0.15 < p_{fz} < 0.15$)

for pp scattering off all targets at 10 Gev

Target	N_h	N_n	T_r	γ_1	γ_2	T
Li	107	241	2.3	0.78	5.4	0.54 \pm 0.035
C	875	1048	1.2	1.2	2.66	0.39 \pm 0.012
Al	575	655	1.1	1.3	3.3	0.27 \pm 0.011
Cu	95	63	0.66	1.2	3.9	0.15 \pm 0.019
Pb	60	20	0.33	1.2	3.9	0.075 \pm 0.017

Table 5.9 No. of events within the central region ($-0.15 < p_{fz} < 0.15$)

for pp scattering off C and Al targets at 12 Gev

Target	N_h	N_n	T_r	γ_1	γ_2	T
C	167	173	1.0	1.1	2.7	0.35 \pm 0.027
Al	167	140	0.84	1.2	3.3	0.21 \pm 0.017

5.1.2 The energy dependence of the proton transparency and its interpretations:

The energy dependence of the proton transparency is summarized in figs. 5.3, 5.4 and 5.5. The transparency as a function of the effective beam energy is plotted in fig. 5.3 for the aluminum target, and in fig. 5.4 for the carbon target. Fig. 5.5 shows the transparency as a function of the beam energy selecting only events in the central region of p_{fz} between $-.15$ Gev to $.15$ Gev. From the plots we note the following features:

The transparency increases indeed as the incident energies increase from 6 to 10 Gev as expected by PQCD.

However, the transparency drops off appreciably at 12 Gev for both the carbon and aluminum targets, the only ones for which 12 Gev data were available. The drop off in the case of carbon target is not as pronounced as that for the aluminum target.

The transparency for lighter targets varies more slowly with energy than for the heavier targets.

All heavier targets show similar characteristics.

Our interpretation of the transparency data would have been more straight-forward, if we had not measured transparencies for incident energies above 10 Gev. Below this momentum, the transparency increases with the energy as expected by PQCD; the heavier targets seem to

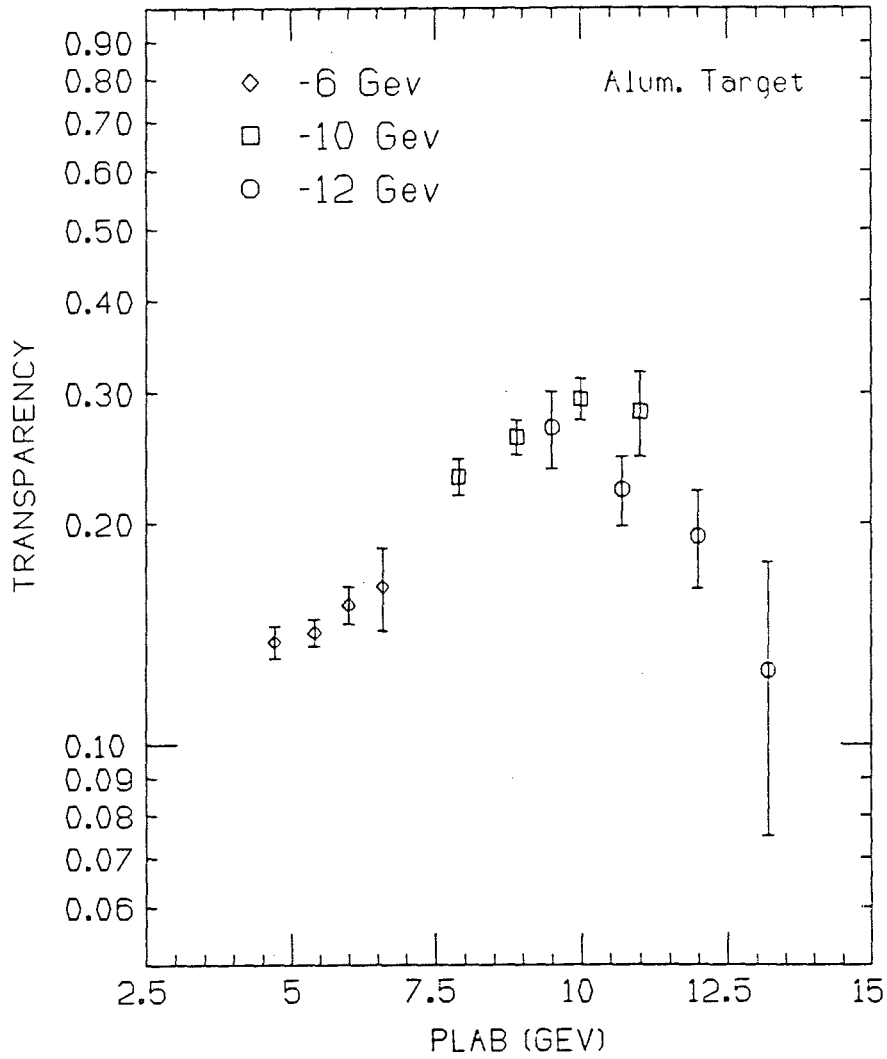


Fig. 5.3 The proton transparency as a function of the effective energy for the aluminum target.

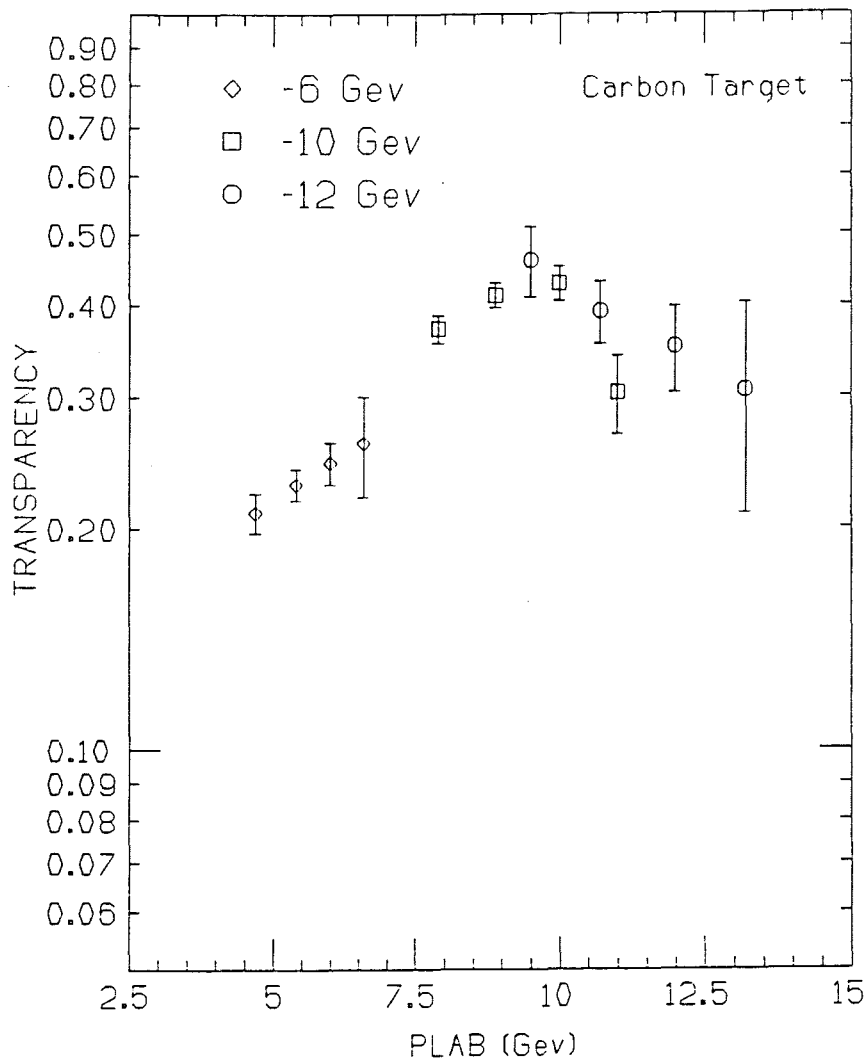


Fig. 5.4 The proton transparency as a function of the effective energy for the carbon target.

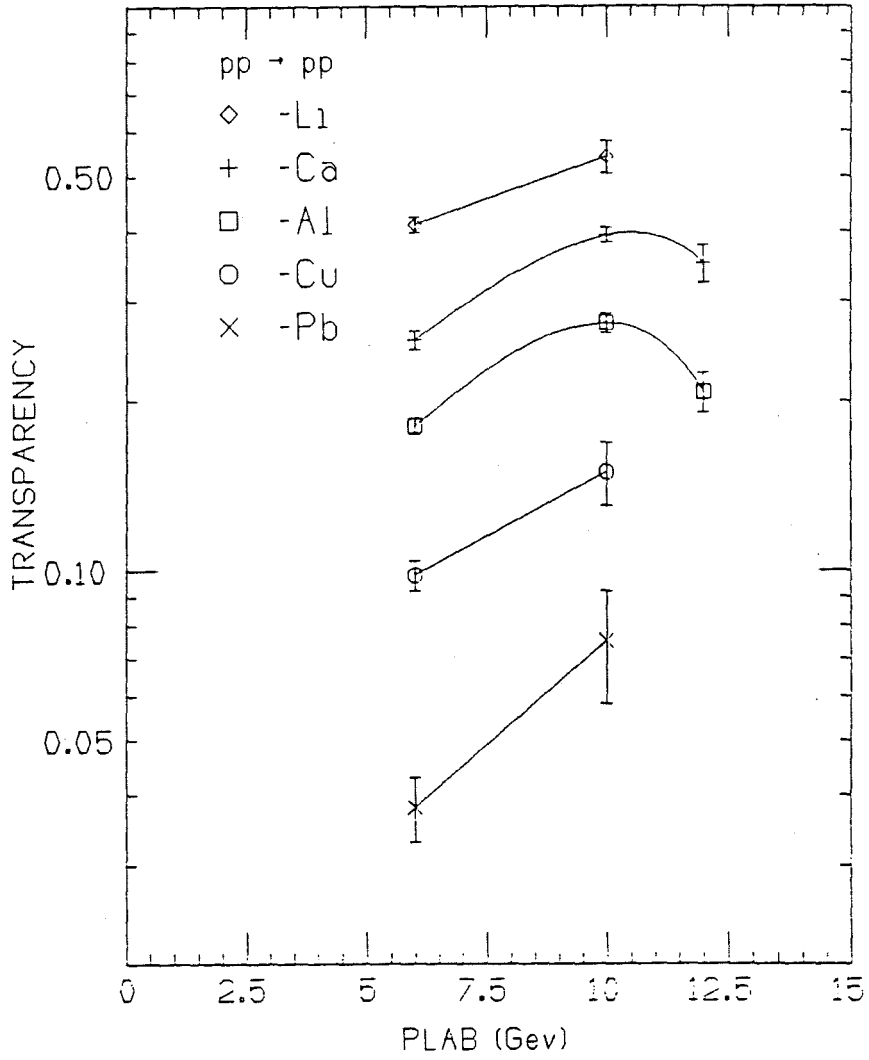


Fig. 5.5 The proton transparency as a function of the incident energy for all targets.

approach the asymptotic energy, where the transparency is expected to reach its asymptotic value of 1, more slowly than the lighter targets as evidenced by their lower value of transparency at the measured energies and so on. However the sudden drop off of the transparency at 12 Gev (obvious for Al, less clear for C) poses difficulties for PQCD. Two models have been proposed to explain the behavior of our data: the resonance or threshold production model by S. Brodsky and de Terromond and the chromo phase interference model by P. Ralston. In the following we will outline the main points of the two models.

According to Brodsky model (Bro 1988), the process of $pp \rightarrow pp$ occurs through two different channels: the short distance elastic scattering channel, which is described by PQCD, and a resonance production channel, which possesses the properties of normal hadronic interactions at large distances. The resonance decays into pp with a finite branching ratio so it is not easily distinguishable from the non-resonant pp elastic scattering. However when the interactions happen in nuclear matter, as was the case in E834, the resonance decay component is mostly absorbed by the nuclear medium, so we are left with contributions from the short distance elastic scattering alone. Assuming that the resonance production dominates at its threshold the sudden drop in the transparency can then be easily explained as due to the absorptions of the protons from the resonance decay by the medium. Moreover, if in addition the resonance is assumed to be of $J = L = S = 1$ it can also be used handily to explain the very challenging results

from the polarized proton scattering experiments. It was found that at $p_{\text{lab}} = 11.75 \text{ Gev}$ and $\theta_{\text{c.m.}} = 90^\circ$, protons with their spins polarized parallel have 4 times as large a probability of scattering as when their spins polarized anti-parallel. In terms of the spin-spin correlation asymmetry

$$A_{\text{NN}} = \frac{d\sigma(\uparrow\uparrow) - d\sigma(\uparrow\downarrow)}{d\sigma(\uparrow\uparrow) + d\sigma(\uparrow\downarrow)} \quad (5.10)$$

the results were very illustratively shown in Fig. 2.11. Note that the sharp increase in A_{NN} occurs at about the same energy and angle (same t) where the dip in the transparency is seen. With an assumption that the resonance has a spin of 1, the peak can then be attributed to the resonance. According to Brodsky there are a number of sources that can produce a resonance with a mass $M^* = \sqrt{s} = 5 \text{ Gev}$ and a baryon number of 2:

a) a multi-gluonic excitation such as

$$|gggggggg>$$

b) a hidden color color-singlet excitation

$$|qqqqqq>$$

c) a hidden flavor excitation

$$|qqqqqqQ\bar{Q}\rangle$$

Assuming the resonance is a hidden flavor excitation the model has a number of definite predictions:

The transparency will resume its PQCD behavior once again at still higher energies above the resonance threshold (≥ 16 Gev).

Even at the threshold energies, the transparency should increase as the scattering angles decreases since the resonance decay channel has a much flatter angular distribution than the elastic scattering. (and is less important at smaller angles.)

In pion proton scattering off a nucleus, a similar resonance should also appear at energies corresponding to the πp quark contents.

At the threshold energies, we should see an enhancement in heavy flavor production.

J. Ralston and collaborators (Ral 1988) proposed an idea which explains the structure of our data well without the exotic resonance. The Ralston model proposes that pp scattering involves both the PQCD process at short distances and the Landshoff pinch process at large distances. These two processes interfere with each other resulting in a cross section which is the quark counting law modified by a factor determined mainly by the energy dependent phase shift (Pir 1982):

$$\left(\frac{d\sigma}{dt}\right)_{90^\circ} \approx s^{-10} R_1(s) \quad (5.11)$$

where

$$R_1(s) \propto 1 + \rho_1 (s/\text{Gev}^2)^{1-K} \cos(\phi(s) + \delta_1) + \rho_1^2 (s/\text{Gev}^2)^{2-2K}/4 \quad (5.12)$$

The the energy dependent chromo-Coulomb phase shift consists of an uncalculable part δ_1 and a calculable part $\phi(s)$ whose energy dependence is known. When the scattering occurs in nuclear matter we can simply replace ρ_1 by ρ_A and δ_1 by δ_A so the ratio of the elastic scattering off nuclear targets to that off a free proton, defined as the transparency, is simply:

$$T(s) = \frac{1}{A} \frac{d\sigma(pA)/dt}{d\sigma(pp)/dt} = N_A \frac{1 + \rho_A (s)^{1-K} \cos(\phi(s) + \delta_A) + \rho_A^2 (s)^{2-2K}/4}{1 + \rho_1 (s)^{1-K} \cos(\phi(s) + \delta_1) + \rho_1^2 (s)^{2-2K}/4} \quad (5.13)$$

where N_A is an A dependent, but E independent normalization constant.

Ralston and collaborators argue that for heavy targets, the large distance Landshoff process is completely absorbed and its phase shifts

becomes undetectable. Therefore, the energy dependent phase shift in the transparency is completely determined by the PQCD component.

In the limit of large A such that $\rho_A s^{1-K} \ll 1$, the numerator becomes a constant so

$$T(s) \rightarrow \frac{\text{const}}{R_1(s)} \quad (5.14)$$

i.e., the structure of the transparency for heavy nuclei is completely determined by the structure of the pp scattering cross section as a function of energy. This result together with the observed data points for the carbon and aluminum are plotted in fig. 5.6 where the curves are normalized at 10 Gev. It is clear that the plots of transparency reflect these assertions. It should be pointed out that the Ralston model can also account for the behavior of A_{NN} (Pir 1983).

Clearly our data alone are not enough to rule out either of the two models. However, the two models do have some distinct predictions. If the Ralston model is correct, we would expect that the transparency will simply follow the oscillatory behavior of pp scattering. The model would also predict a similar behavior in the πp transparency. This hypothesis is again supported by the data, even though the statistics are much worse than the pp data. One way of differentiating between the two models would be to measure the transparency at smaller scattering

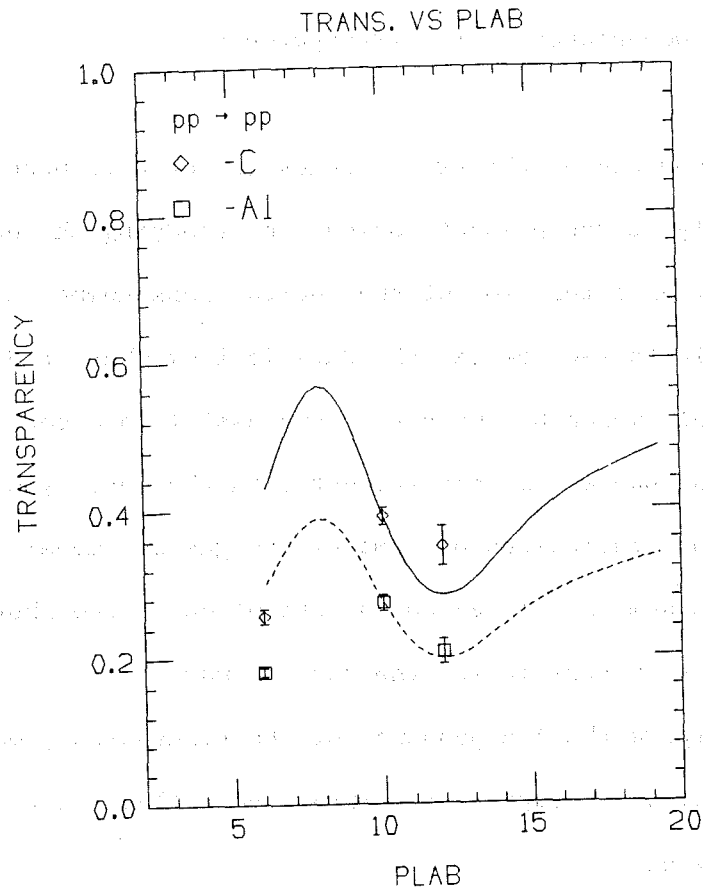


Fig. 5.6 Comparison between the Ralston model prediction and the data on the transparencies. Only the statistical errors are shown in the data points.

angles where the Brodsky model predicts a restoration of transparency, while the Ralston model predicts a continuous suppression according to the measured cross section.

5.1.3 The A Dependence of the transparency

The A dependence of the transparency is not well understood theoretically at the present. However by studying the behavior of the transparency as a function of the nuclear mass number A we should at least be able to see how far the data is from what predicted by the Glauber model, which has been very successful in accounting for the low energy hadron nucleus scattering data. Furthermore by comparing the data with the predictions of some of the guessed models we should be able to gain some knowledge on the evolution of the short distance interaction structure inside the nuclear matter.

To investigate the A dependence of the transparency we will follow the formalism of G. Farrar (Far 1988) and collaborators by defining the transparency as:

$$T = \frac{A_{\text{eff}}(P_1, P_2, P_3)}{A}$$
$$= \frac{1}{A} \int d\vec{r} \rho_A(\vec{r}) P_1(\vec{p}_1, \vec{r}) P_2(\vec{p}_2, \vec{r}) P_3(\vec{p}_3, \vec{r}) \quad (5.15)$$

where P_i denotes the probability that proton i, which carries a momentum \vec{p}_i at the point of hard scattering \vec{r} , passes through the nucleus without experiencing additional interactions, be it elastic or

inelastic. To derive an expression for the probability P_i we imagine that at some point inside the nucleus the hard scattering occurs and the final state small protons travel along their path while expanding. The probability that proton i proceeds from z to $z+dz$ without suffering an interaction with the medium decreases by an amount:

$$dP_i = -P_i(z) dz \sigma^{\text{eff}}(z, \vec{p}_i) \rho_A(z) \quad (5.16)$$

Integrate over the whole path inside the nucleus we have the probability of proton i emerging outside the nucleus without ever interacting with the nucleus:

$$P_i(\vec{p}_i, \vec{r}) = \exp(-\int dz \sigma^{\text{eff}}(\vec{p}_i, z) \rho_A(z)) \quad (5.17)$$

where σ^{eff} is the effective total cross section between the hard scattered proton and the nuclear medium during the expansion. The integral is taken along the path of the proton. For the density of the nuclear matter we used the Wood-Saxon formula:

$$\rho(r) = \frac{c}{1 + e^{-(R-r)/b}} \quad (5.18)$$

where c is a normalization constant chosen such that $\int \rho(\vec{r}) d\vec{r} = A$, and

$$R = 1.1A^{1/3} \text{ fm} \quad (5.19)$$

$$b = 0.56 \text{ fm}$$

It is more difficult to determine the effective cross section σ^{eff} . For simulating the Glauber processes we can simply put in the total hadronic cross sections, for example, 40 mb for the protons and 25 mb for the pions. However the simulation of the shrunken protons is more involved and model dependent. The main reason is that it is not clear how the protons expand back to their normal sizes from a anomalously small configurations. The simplest approach is to assume that the cross section scales as the transverse size of the expanding proton:

$$\sigma^{\text{eff}} = \frac{x_t^2(z)}{\langle x_t^2 \rangle} \sigma_{pA} \quad (5.20)$$

where σ_{hA} is taken to be the total hadronic cross section of the proton, i.e., 40 mb, and $x_t(z)$ is the transverse size of the proton at point z on its path. To find the transverse size of the hadrons we

imagine that at the point of interaction the quarks occupy a transverse area given by:

$$\frac{n^2 \langle k_t^2 \rangle}{t} \sigma_{pA}$$

where k_t is the typical intrinsic transverse momentum carried by a quark inside a hadron, about .35 Gev in value, t is the four momentum transfer squared of the hard scattering process, and n is the number of valence quarks, i.e., $n = 3$ for protons, and $n = 2$ for pions. From this initial size the proton then expands while travelling through the nucleus. To obtain some idea on how the expansion mechanism affects the transparency we follow Farrar by taking up two different expansion models: the naive parton model and the QCD motivated quantum diffusion model. In the naive parton model the partons flight away with a velocity of light so that at time t after the hard collision the transverse size of the hadron in the lab is $(E/m)z$ where z is the longitudinal distance that the hadron has traveled. This suggests a transverse area of $x_t^2 \propto z^2$ where z is the longitudinal distance traveled by the hadron after the collision. In the PQCD inspired quantum diffusion model the transverse size of a hadron is considered to be proportional to the longitudinal distance, i.e., $x_t \propto z$.

Therefore the effective cross section can, in general, be expressed as:

$$\sigma^{\text{eff}} = \sigma_{\text{hA}} \left(\left[\left(\frac{z}{l_h} \right)^\tau + \frac{\langle n^2 k_t^2 \rangle}{t} \left(1 - \left(\frac{z}{l_h} \right)^\tau \right) \right] \theta(l_h - z) + \theta(z - l_h) \right) \quad (5.21)$$

where $\tau = 0$ corresponds to the case of no expansion, i.e., the Glauber case, $\tau = 1$ corresponds to the quantum diffusion expansion and $\tau = 2$ corresponds to the naive parton expansion, and l_h is the distance traveled by the proton during the time of expansion, which has to be estimated from model as well. In the naive parton model $l_h = E/m\sqrt{\sigma_{\text{hA}}}/\pi$. In the PQCD inspired models l_h is determined by the dominant denominator in the light cone quantization propagators:

$$l_h = \frac{1}{\langle E_n - E_h \rangle} \approx 2p_h \frac{1}{\langle M_n^2 - M_h^2 \rangle} \quad (5.22)$$

where M_n is the mass of a typical intermediate state and p_h is the momentum of the hadron. For proton we used the value

$$\frac{1}{\langle M_n^2 - M_N^2 \rangle} = \frac{1}{.7 \text{ GeV}^2} \quad (5.23)$$

as adopted by Farrar.

Since the problem was spherically symmetric the actual simulation was fairly simple. The whole nucleus volume, which was taken to be a sphere

with a radius 3 times as large as that given by eq. 5.19 to take into account the exponential tail of the Wood-Saxon density function, was divided into spherical shells with infinitesimal thickness. Within each shell the location of the hard collision was randomly chosen. The incoming and outgoing protons were then traced through the nucleus volume and the survival probability of protons were calculated with eq. 5.17 using a total hadronic cross section of 40 mb. It is clear that the transparency depends on the polar angle of the interaction point within each shell. Therefore, multi points were generated and the resulting transparencies were averaged. The contributions from all the shells were then summed up and normalized by the mass number A to get the transparency T .

The results of the simulations together with the data points are plotted in fig. 5.7. From the bottom upward the curves represent the Glauber model prediction, the QCD diffusion model predictions at 6, 10, 12 Gev, the naive parton model prediction at 6 Gev and the QCD diffusion model prediction at 20 Gev respectively. In the case of the Glauber model the fraction of protons seen by the incoming proton is approximately constant for very heavy nuclei contrary to the notion that the quasi elastic pA cross section should be proportional to the radius of the nucleus. The reason is that even the outer ring of the nucleus is shadowed when the nucleus is very large. The steep rise down to the light nuclei end is mainly due to the back scattering by the penetrating protons. The most important feature of the plot is that the

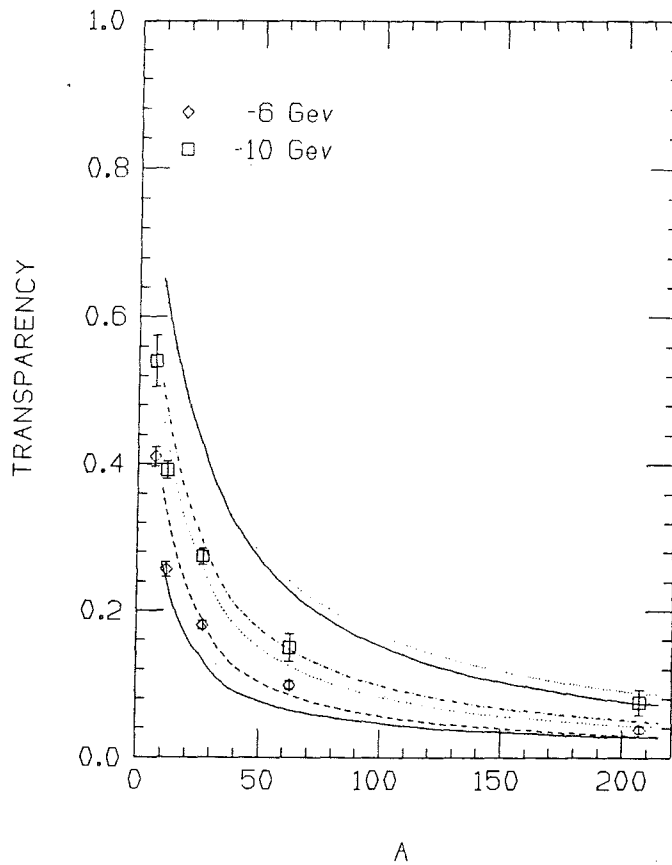


Fig. 5.7 A dependence of the transparency. From the bottom upwards the curves represent the Glauber model prediction, the QCD diffusion model predictions at 6, 10, 12 GeV, the naive parton model prediction at 6 GeV and the QCD diffusion model prediction at 20 GeV. The error bars include only the statistical errors.

data clearly disagree with the Glauber model predictions. This together with the fact that the transparency increases with energy constitute important evidence for the existence of the color transparency effect. Note that the naive parton model always gives a higher transparency. This is due to the smaller effective cross section and longer expansion time in that model. Another interesting feature to note from the plot is that the data points seem to favor the quantum diffusion model. However it should be pointed out that there is an overall normalization uncertainty in the determination of the transparency, as will be discussed in the next section. Namely, the data points could move upward or downward by about 20% approximately in parallel to the curves.

5.1.4 The errors and uncertainties on the proton transparency

It should be fairly obvious that the whole analysis presented here hinges on the assumption that the observed cross section of a free proton scattering off a proton inside the nucleus can be represented by a free particle cross section modulated by a nucleon spectral function:

$$\left(\frac{d\sigma}{dt}\right)_{\text{obs}} = T(p)f(p)\left(\frac{d\sigma}{dt}\right)_{\text{free}} \quad (5.24)$$

Furthermore the effects of the binding, the recoil and the Fermi energies were all neglected. The validity of these assumptions can be questioned in two levels: first, can the off shell scattering cross section be approximated by on shell one? Second, if the answer to the first question is yes, how does one choose the kinematic variables so the actual off shell scattering can be best approximated? Or in our case, how big an error is introduced by neglecting all the energies mentioned above?

To answer the first question, it is probably helpful to look at the diagram, drawn in fig. 5.8, where the gluon lines connecting the hard scattered protons and the remnant nucleus represent the soft interactions through which the off-shell protons go on mass shell. Needless to say, after the scattering process both protons have to be on the mass shell. Therefore, the process can probably be thought of as

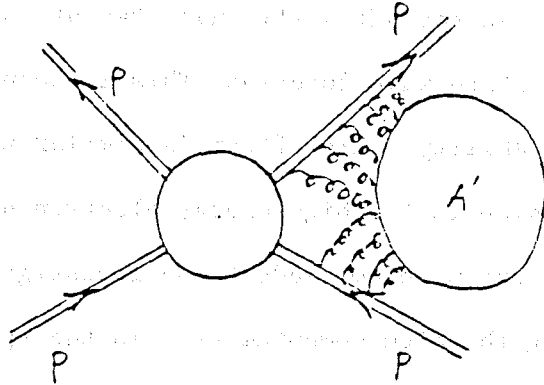


Fig. 5.8 Schematic view of a proton scattering off an off-shell proton from a nucleus.

proceeding through two different stages. In the first stage (not in the sense of time sequence!) the off shell proton interacts with the nuclear system by exchanging soft gluons to go on the mass shell. Some time in that process the hard interaction occurs and the resultant final state protons proceed on their way out. The process of going on the mass shell will continue if the ejected proton has not done so already by that time. If this picture is true we should expect that the further the proton is off mass shell, the less likely the hard scattering process will be intact, because the more energy being exchanged through the soft processes, the more likely that something

will be produced. This effect can be expressed in a more formal language by saying that the off shell character of the proton suppresses its Fock state wave function. This in turn suppresses the hard scattering probability. This effect is similar to the off shell form factor suppression in the high energy electron quasi elastic scattering. Clearly the problem needs to be investigated further. However, by avoiding the high momentum tail in the spectrum when counting the elastic events, we hope to minimize this effect.

To answer the second question, we need to analyse the effects of the binding and the recoil energies in more detail. First let's consider the recoil. Intuitively we might think that the whole remnant nucleus recoils against the ejected proton when the hard scattering occurs. If this is indeed the case then the recoil energy should be negligible, because the nucleus is heavy. However, this picture may not be valid in the high momentum region. It has been suggested (Str 1980) that the very existence of the tail can be attributed to the short distance nucleon correlations. Namely, the nucleons inside the nucleus form localized clusters. When a proton in the cluster is knocked out it is more likely that the remaining members of the cluster, not the whole nucleus, recoil against the ejected proton. At high momenta, the recoil energy will not be small for the case of, say, two nucleon clusters. The reason for this is not difficult to understand physically. Imagine that a very high energy projectile impinges on one of the clusters in the nucleus. In order for the nucleus to recoil as a whole there has to

be enough time for the remainder of the cluster to interact with the rest of the nucleus, and for the remnant nucleus to readjust itself. However, the time scale of the hard interaction is so short compared to the time scale involved in a typical nuclear interaction it is not likely that this readjustment will happen. What happens is probably that the partners in the cluster recoil inside the nucleus and presumably will lose their energies gradually to the nucleus through soft processes, resulting in an excited nucleus. To get an idea on how large this recoil effect can be on the kinematics of the process, let's consider the case where the ejected proton has a momentum of .5 Gev. Assume that only one proton recoils after the hard scattering. The recoil energy is .14 Gev. The corresponding change in s at 10 Gev incident energy is $2 \times 10 \times .14 = 2.8 \text{ Gev}^2$, which in turn means a change in cross section of $(20/17.2)^{10} = 4.5$. Namely, a hard scattering off a proton with a momentum of 0.5 Gev will get a kinematic boost of a factor of 4.5 in the cross section, if it is indeed one nucleon that recoils against the ejected proton. This analysis shows that the apparent enhancement in the tail region could well be due to the kinematic boost. If the tail events are counted in deducing the transparency and the recoil energy is neglected in calculating the correction factors we could over estimate the transparency substantially.

Next let's consider the effect of the binding energy. Even though on

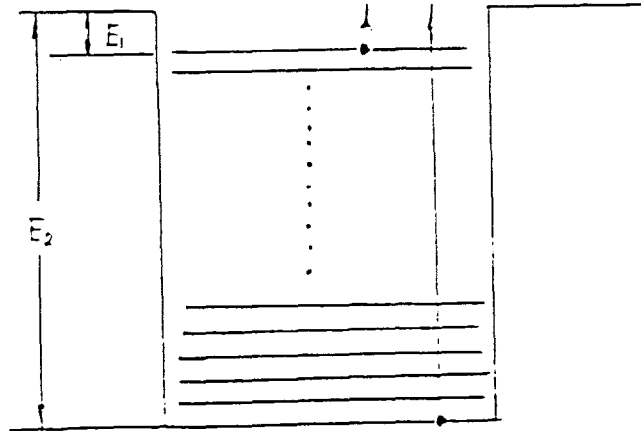


Fig. 5.9 Schematic view of scattering off nuclear protons from different energy levels.

the average the separation energy of a nucleon is quite small, the actual binding energy for a particular proton being ejected depends on what level it is ejected from. The situation is shown schematically in fig. 5.9. When a proton is knocked out from certain energy level the corresponding binding energy is the difference between that level and zero. It is obvious that the energy one has to put in varies considerably when knocking out a proton from the different levels. The question is how the momentum varies as the energy level. For harmonic oscillator potentials the momentum increases with the energy, i.e., the high momentum region correspond to high level. This means that

scattering off a proton with lower momentum will get a larger kinematic boost in the cross section, compared to scattering off a proton with higher momentum, because the effective energy in the process is lower due to the larger energy lost to the binding. However the situation will be reversed for the hydrogen like potentials because there the high momentum region corresponds to lower energy levels. This will distort the spectrum if the effect is not corrected for. The distortions could be important for the heavy nuclei. Once again by dropping the tail region in counting the elastic events we hope to keep the effect small.

In summary, by not counting the events in the high momentum tail region we hope to keep the errors resulted from neglecting the recoil and binding energies small. However this brings up the question of what is the actual fraction of the tail region, which is needed in determining the transparency. Clearly independent measurements on the full momentum spectral functions, including the tail, would be very useful in this regard. For now we can only make some rough estimates. According to some theoretical estimates the fraction of the probability in the tail is between 15 to 35 percent. By using the Moniz model, we in effect assumed a tail fraction of about 15%, (the tail in this model extends to 4 Gev) depending on the material. This indicates that the uncertainty is about 20%, which varies from target to target. Another way of estimating the fraction is by looking at our own spectral functions and comparing the apparent tail with that predicted

by the more conservative Moniz model. The difference is again about 20%.

The sources of the systematic errors could include: the bias in the event identification because of the finite solid angle coverage and the photon conversion inefficiencies of the veto counters; the event losses due to the event selection cuts imposed in the analysis, the losses due to the accidental vetos caused by the decay products of the excited nucleus, the follow up interactions and the noises of the counters; the distortions of the spectral functions due to the elastic final state interactions; and the acceptance changes due to the Fermi smearing.

The veto counters could produce bias causing apparent enhancement to the signal in the low Fermi momentum central region because the counters do not have 4π coverage. π^0 's emitted almost colinearly with the hard scattered protons could escape from detection because the wire chambers do not register neutral particles. To estimate the magnitude of the effect we studied the dominant background process $pp \rightarrow pp\pi^0$ using Monte Carlo simulations. The results are shown in fig. 5.10 in which the p_{fy} distribution for the events which satisfy the veto cut and for the ones which do not satisfy the cut. No appreciable bias can be seen from the plot. The problem can also be studied by noting that the veto counters cover different angular range for particles originating from different target segments. Namely, the co-produced particles can escape from the veto counters at larger angles with

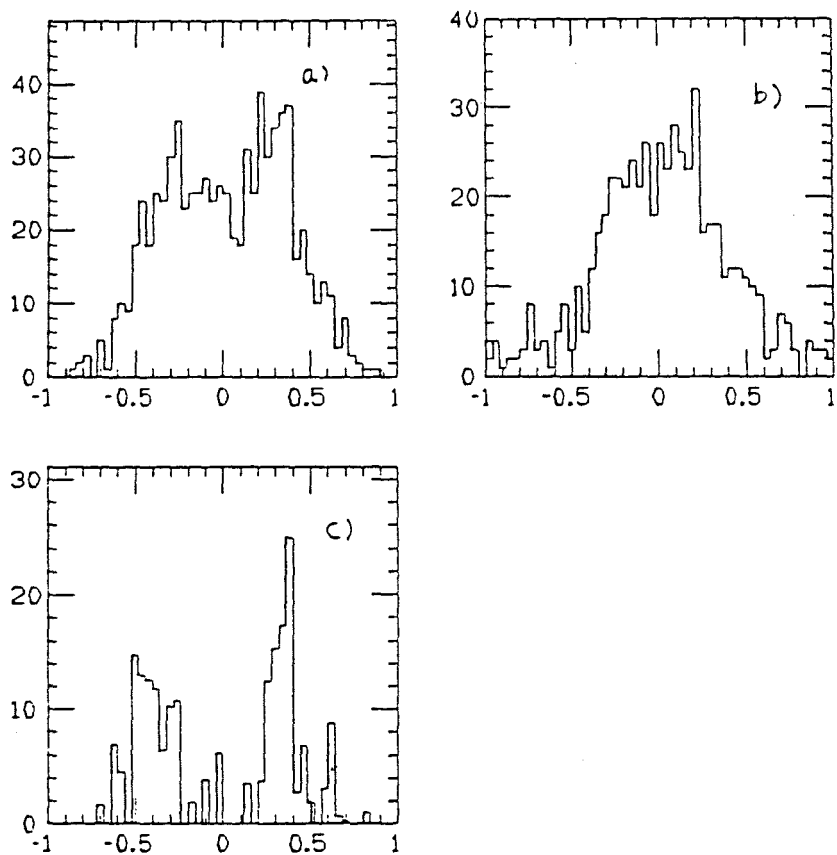


Fig. 5.10 The simulated inclusive decay of $pp \rightarrow p\Delta$. a) Events with veto cut on, b) events with veto cut off, c) the difference.

respect to the leading particle when originating from the down stream segments than when originating from the up stream segments. This means that the fraction of background events that appear in the signal sample for the down stream segments will be larger than that for the upstream segments, and the fake signals from the up stream segments could be more concentrated in the central region. By separately identifying the signal and the background events from the up and the down stream segments we should be able to find out whether this difference of angular coverage produces appreciable effects on the net signal identification. It was found that the discrepancies in the number of elastic events are within the errors accountable by the attenuations of the beam, which is about 10%, and the statistics, even though the number of background events picked up from the up and the down stream segments do vary by about 20%. The photon conversion inefficiencies of the veto counters will not affect the transparency as long as it is uniform for particles emerge at all angles.

The losses of the events due to the cuts imposed in the analysis were studied quite carefully for a few runs at the beginning of the analysis. As a matter of fact the cuts were established with the criteria that the resulted loss of events should be less than 5%.

Because the target system was designed such that particles exiting at 90 degrees with respect to the beam in the center of mass frame will not pass through the target segments that are further down stream absorptions by segments other than the one from which the hard

scattered particles emerge, are negligible. Absorption by the same segment is also small because each segment contains only about .025 interaction length of material. Accidental vetos caused by the decay debris of the excited nucleus, the follow up interactions, and the noises of the counters are believed to be unimportant because the background p_{fy} plots do not show any appreciable peaking when the anti-veto cut was imposed.

The elastic final state interactions, commonly referred to as the multiple scattering or Glauber interactions, could be another source of error. These interactions broaden the spectrum, thus, reducing the content in the central region. This reduction of content in the central region will in turn decrease the resulted transparency because we only counted the events in the central region in determining the transparency. We will come back to this point when we discuss the spectral functions. For now we want only to point out that in all the cases, these effects seem unable to account for all of the apparent enhancement in the tail region. Monte Carlo studies indicate that changes in the acceptance introduced by the Fermi smearing is also small.

In summary the overall uncertainty in transparency is about 25%, which is dominated by the uncertainty in the tail fraction of the spectral functions. It should also be pointed out that the uncertainties depend on both the energy and the target material.

5.2 The pion transparency

The data on the pion transparency suffer further uncertainties due to the lower statistics and also due to the mis-identification of the beam pions. Fig. 5.11 shows the finely binned p_{fz} distribution for the πp scattering off aluminum target at 6 Gev. By counting the number of events under the high pion peak and the lower proton peak it is estimated that there is about 30% contaminations from the protons. Unfortunately this separation was possible only from the p_{fz} plot at 6 Gev incident energy. In the p_{fy} plot, which we used to separate the

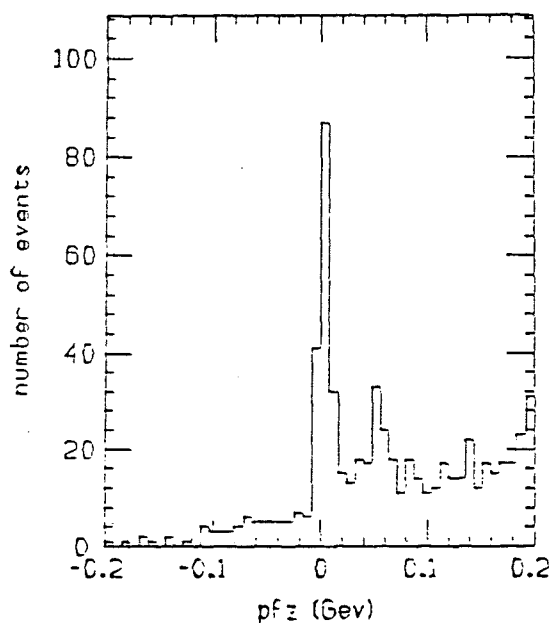


Fig. 5.11 P_{fz} distribution for the pion scattering. Note the second peak which is due to the proton contamination.

signals from the background, the separation was not possible because of the beam momentum dispersion. Because of this the data at 6 Gev will be presented with pure pions identified and those at 10 Gev will be presented with contaminations. No data on pions at 12 Gev were taken.

The determination of the transparency for pions were similar to those for the protons. At 6 Gev the number of protons were identified from the pion samples from the finely binned p_{fz} plots for each of the targets. These events were then subtracted from the elastic samples identified from the p_{fy} plots. At 10 Gev the contaminated samples were used for the determination of the transparency without any fiddling. The resulted samples of the elastic events for all the targets are listed in Table 5.10. As in the case of the proton transparencies the errors listed include only the statistical ones. The corrected transparency is plotted in fig. 5.12.

The most striking feature of the pion transparency is that its magnitude is very close to that of the protons. This seems very surprising because, as we have pointed out in section 2.4, the asymptotic energy for a pion is much lower than that for a proton. However, it should be pointed out that the transparency depends very much on the expansion mechanism. If the anomalously small pion expands fast enough, the transparency could be small no matter how small the pion was initially. Another point worth noting is that according to the Brodsky model there should be a similar resonance in the pion

Table 5.10 No. of events in the central region for πp scattering
off all targets at 6 Gev

target	N_h	N_n	T_r	γ_1	γ_2	T
Li	75	122	1.6	0.71	5.4	0.43 \pm 0.05
C	117	112	0.96	0.85	3.9	0.29 \pm 0.027
Al	143	91	0.64	1.0	3.3	0.19 \pm 0.02
Cu	95	34	0.36	0.90	3.9	0.10 \pm 0.018
Pb	47	7	0.15	0.90	3.9	0.043 \pm 0.016

Table 5.11 No. of events in the central region for πp scattering off
all targets at 10 Gev

target	N_h	N_n	T_r	γ_1	γ_2	T
Li	20	44	2.2	1.3	4.9	0.58 \pm 0.087
C	143	195	1.4	1.2	2.7	0.44 \pm 0.032
Al	97	121	1.2	1.0	4.2	0.28 \pm 0.026
Cu	9	5	0.56	0.90	3.9	0.16 \pm 0.072
Pb	8	-				

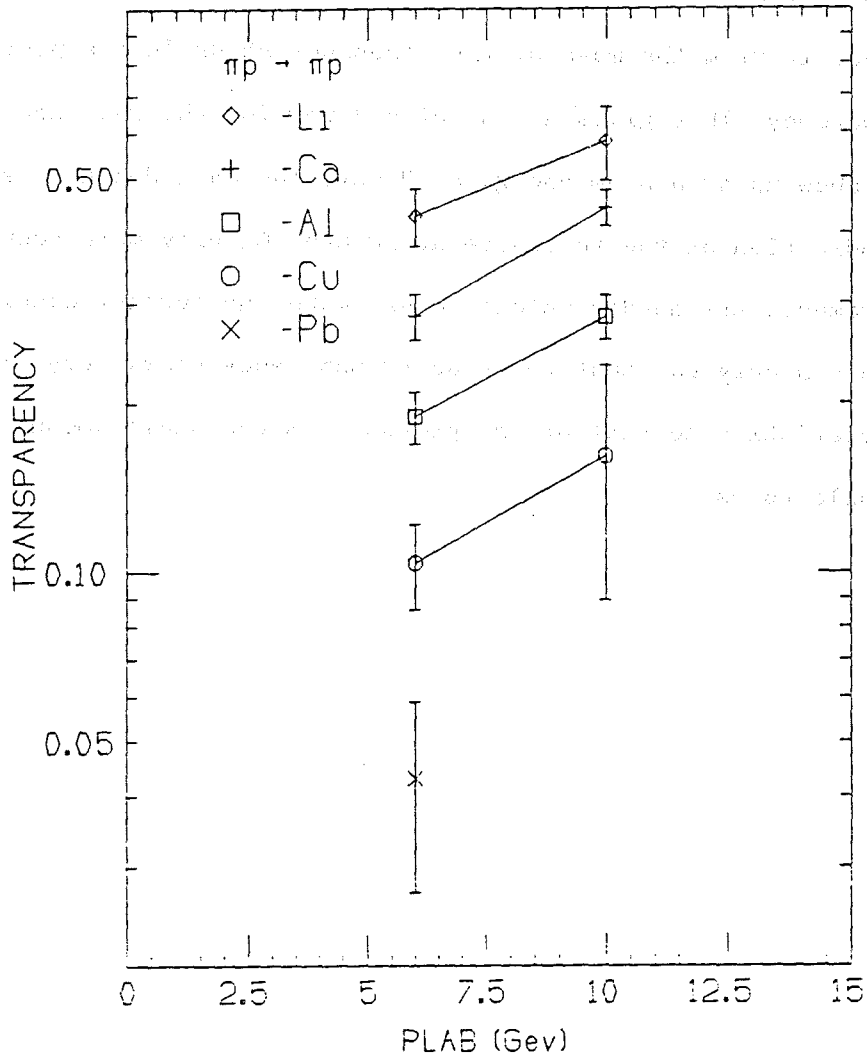


Fig. 5.12 The pion transparency as a function of the incident energy for all the targets.

transparency corresponding to the quark contents of the pion proton system. The most crude estimate of the mass of the resonance would be to take the mass difference between the a proton and a pion and subtract it from the mass of the resonance shown in the proton transparency. This gives a mass of 4.3 Gev for the resonance which would show up at a beam energy of 9 Gev. The data doesn't seem to show any indication of the resonance at 10 Gev. Clearly more accurate measurements are needed before we can make any further conclusions. For now we can only say that the pion transparency shows very similar characteristics to that of the proton from the small amount of data available to us.

5.3 The nucleon spectral functions

We now turn to the second part of our data presentation, i.e., the study of the nucleon spectral functions. As we have pointed out earlier, the quasi elastic scattering data itself is a measurement of the spectral functions if the observed cross section can be expressed in the form of eq. 5. 11. As was also pointed out earlier, the observed longitudinal component of the spectral function p_{fz} was severely skewed towards the positive p_{fz} end because of the rapid rise of the cross section with decreasing s . However, to the lowest order approximation, the transverse components do not contribute to the s , at least in the central region, so a plot of the observed p_{fy} distribution should be a fairly good representation of the spectral function. The results on the observed spectral functions are collected in fig. 5.13 to 5.17 for all targets used at different energies.

The most important characteristics of the observed spectral functions, comparing to those obtained from the low energy electron scattering experiments or from the model predictions for the same material, is that in each of the targets used, there is a substantially higher tail. The possible explanation for the tail enhancement has been given in section 5.1.4. Here we will further elaborate on it a little. As was pointed out there, the most important contribution to the

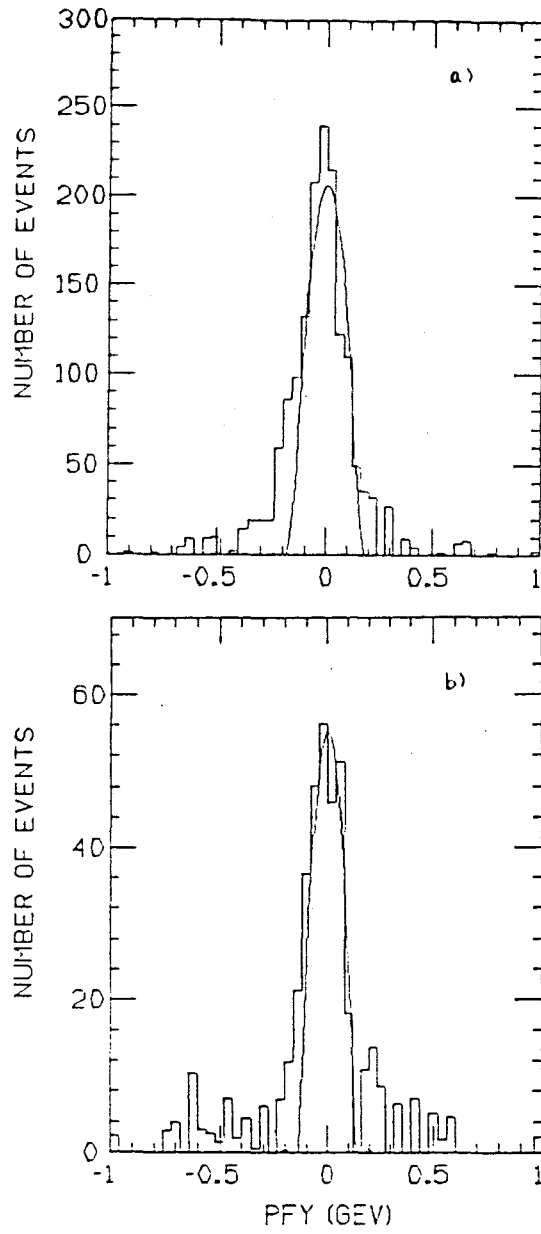


Fig. 5.13 The spectral function of lithium. a) at 6 Gev, b) at 10 Gev.

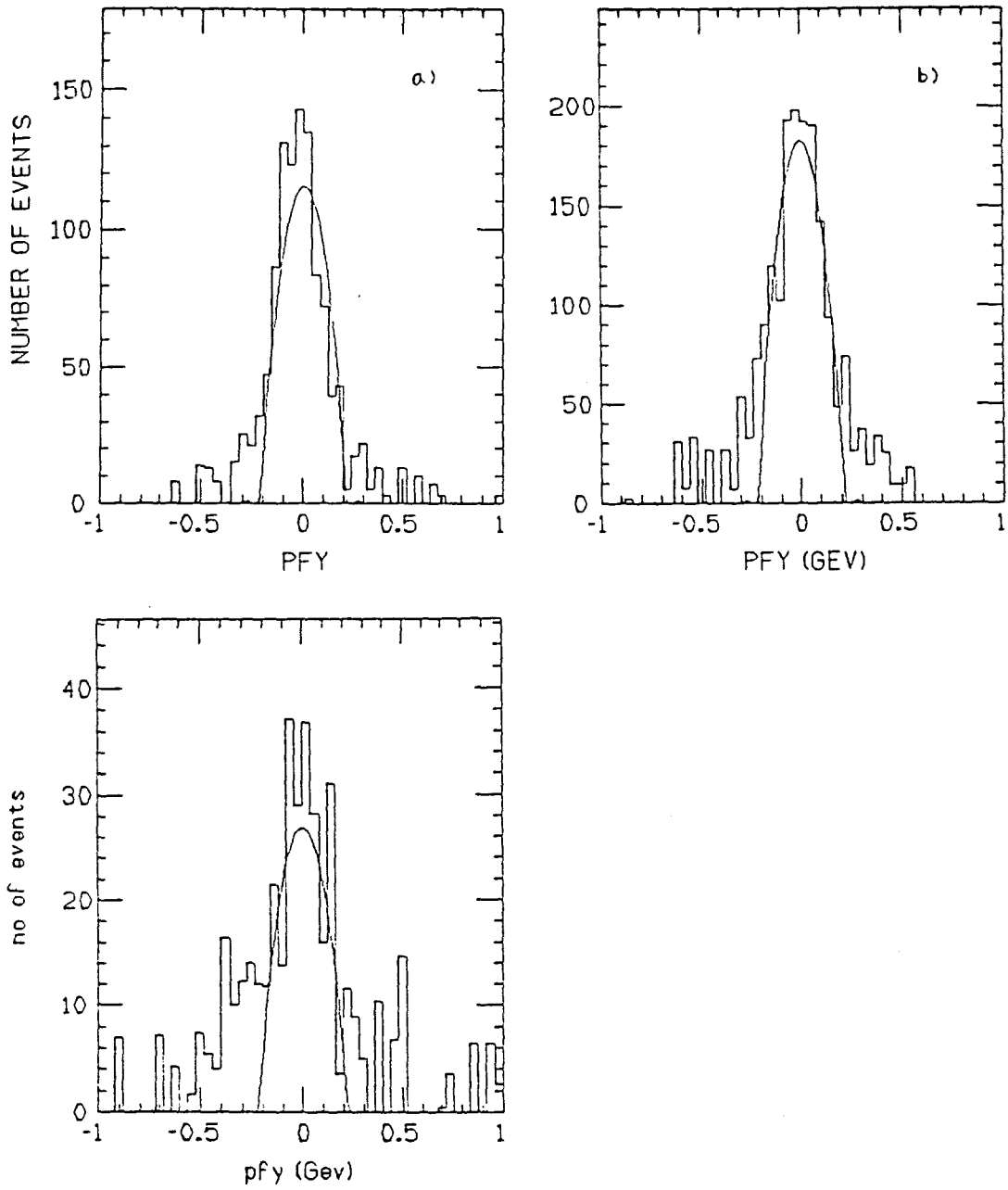


Fig. 5.14 The spectral function for carbon. a) at 6 Gev, b) at 10 Gev, c) at 12 Gev.

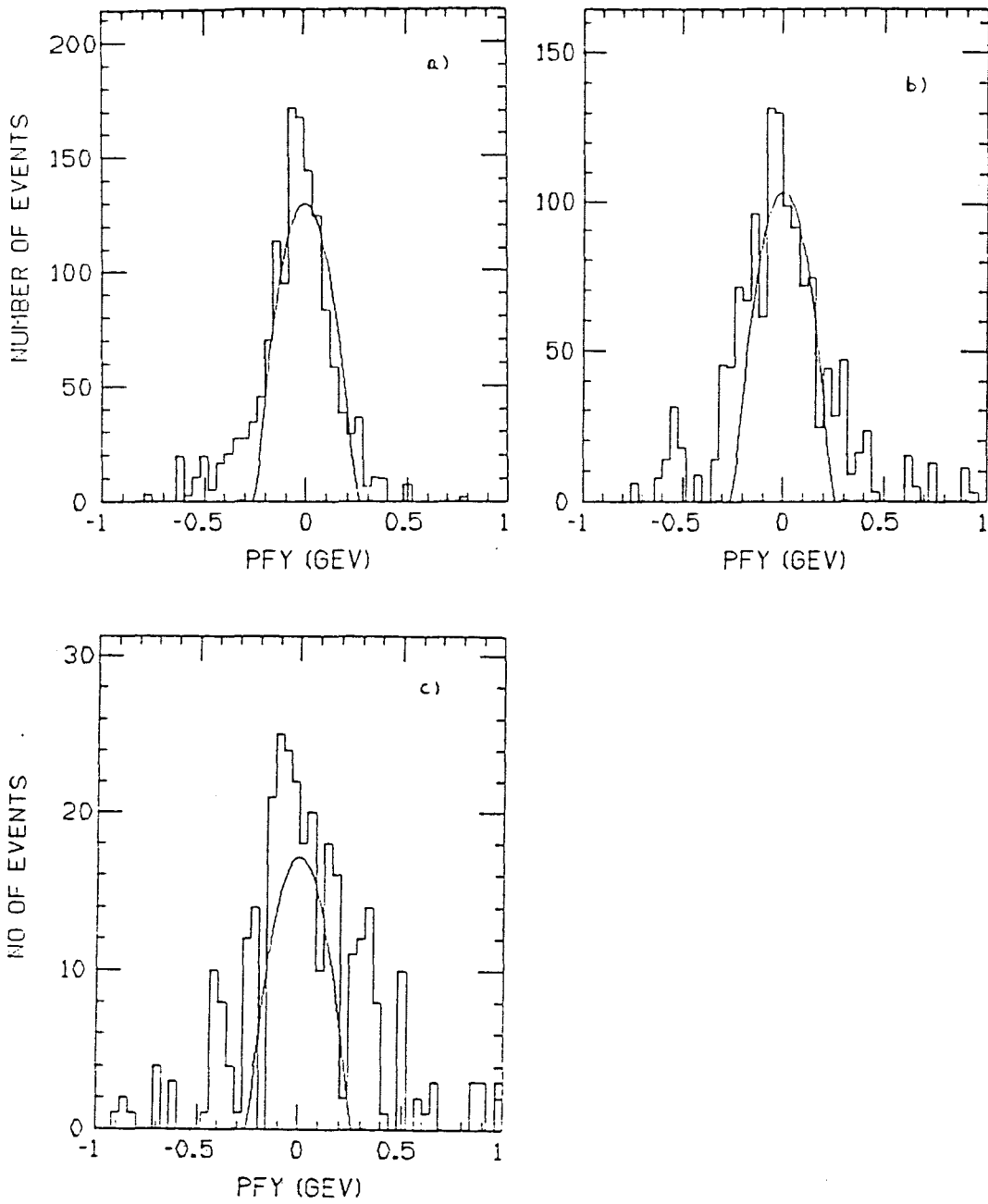


Fig. 5.15 The spectral function for aluminum. a) at 6 Gev, b) at 10 Gev, c) at 12 Gev.

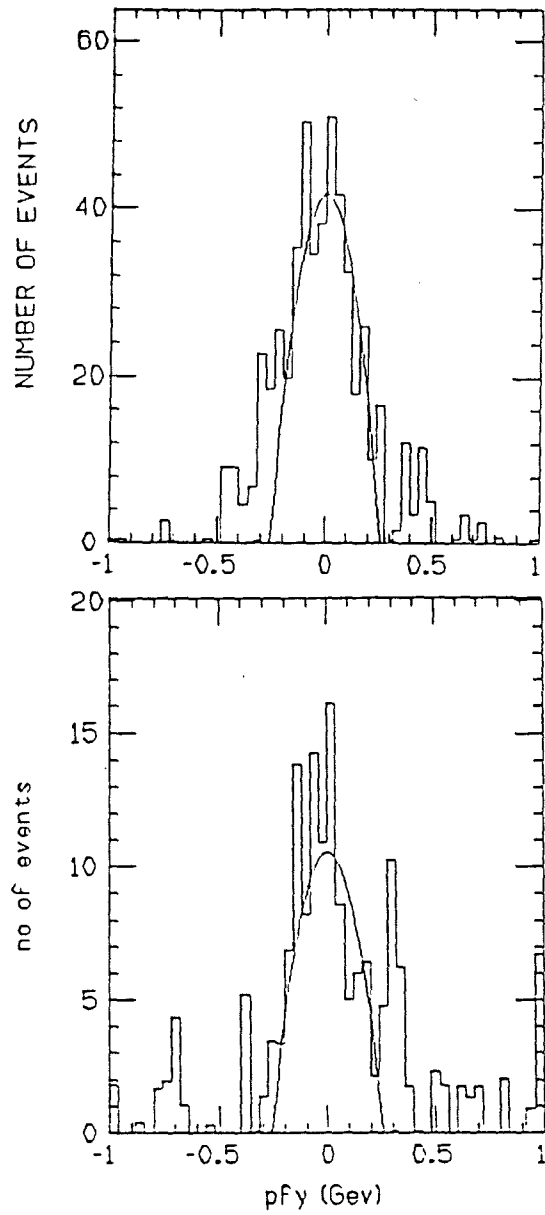


Fig. 5.16 The spectral function for copper. a) at 6 Gev, b) at 10 Gev.

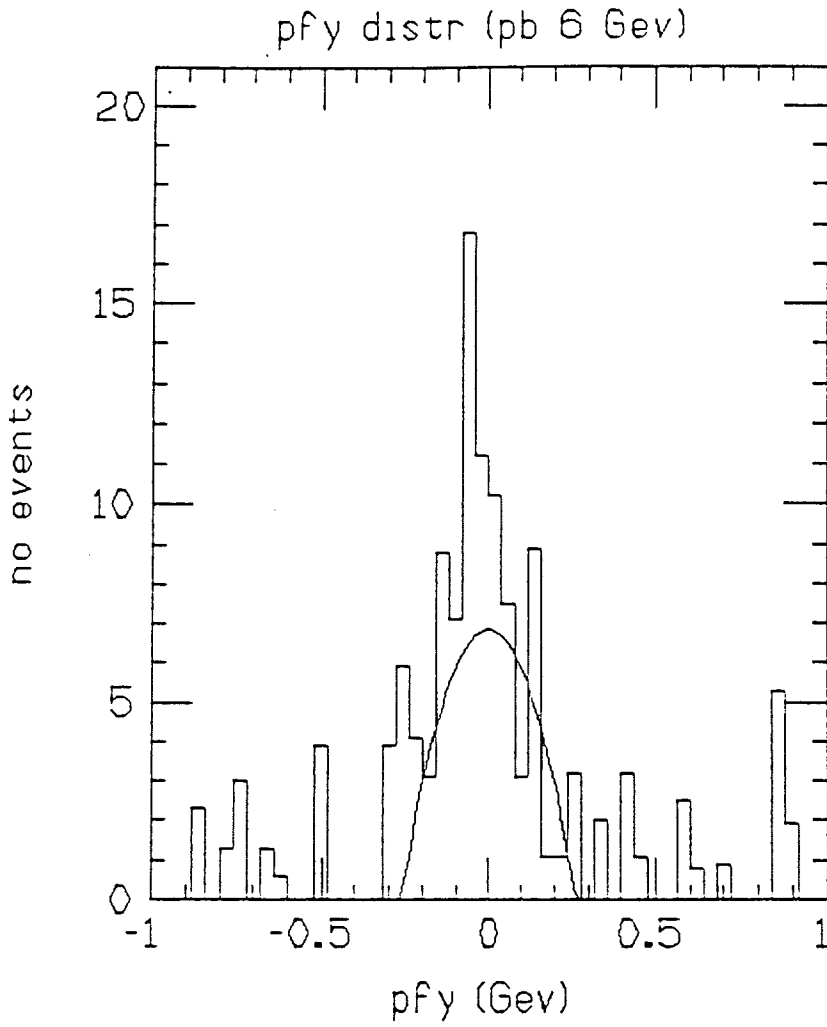


Fig. 5.17 The spectral function for lead at 6 Gev.

increase is probably kinematic, i.e., the decreases of the effective energy due to the recoil and/or the binding energies. Let me now compare these contributions to the contribution from the initial and/or final state elastic interactions. First we note that the total elastic cross section is about 1/3 of the total inelastic cross section for pp. Using the observed transparency of .3 at 10 Gev we would conclude that only about 23% of the hard scattered protons experience the final state soft elastic interactions. The characteristic width of the smearing by the multiple scattering in p_{fy} was estimated to be about .2 to .3 Gev. Superposition of this width with a true spectral function for a heavy target like aluminum with a width of .25 Gev gives a spectral distribution with a width of about .35. It is easy to see that spill over from the central region to the tail has to be less than 30% (The ratio of the area under the true spectrum to the area under the superposed spectrum. The ratio is 30% for a flat spectrum.) of the the total fraction possible which is 23%. Thus, the contributions from the elastic soft interactions can only account for 7% or so of the tail for a heavy target. The situation is quite different for a light target because the width due to multiple scattering does not vary as the target material while the intrinsic spectrum of a light nucleus is much narrower. Thus, a larger fraction of the events which suffer multiple scattering will be spill into the tail. For example, for Li target the width of the intrinsic spectrum is about .15 Gev and the superposed

width is about .29 Gev. Thus, about 50% of the 23% of the hard scattered protons could spill into the tail region, giving a tail fraction of about 12%, which is actually quite close to what was seen. The actual spill over fraction will be somewhat smaller than 12% because the Li transparency is larger than .3, making the fraction of the hard scattered protons that suffer the soft elastic scattering smaller. Incidentally the kinematic boost for a light target is much smaller than that for a heavy target because the average tail momentum for a light target is expected to be smaller. It is quite interesting to note that using this idea we can estimate the change of the fraction in the tail region from the measured transparency. For example, The transparency at 12 Gev is about 35% lower than that at 10 Gev for aluminum. Thus we should see about 4% more tail events. This is consistent with the data though not conclusive because of the low statistics.

Aside from the uncertainties mentioned before, it is also known from nuclear physics that the spectral functions are quite different for different energy levels. Data from the low energy electron quasi elastic scattering experiments on light nuclei seem to indicate that the higher energy levels, corresponding to smaller separation energies, have larger high momentum component, consistent with what would be expected from the harmonic oscillator potentials. In E834 the protons could be ejected from any state. Thus, the measured spectrum is a sum over all the energy levels. If for some reason the hard scattering

process picks up more protons from higher energy levels, then there could be distortions towards larger momentum. However it is hard to imagine that the variation can be as large as what has been observed.

More fundamental explanations for the enhancement in the tail can also be argued if we believe that the hard scattering process does have the preference of picking up the short distance component of the proton wave functions. It was argued (Str 1984) that the EMC effect can be explained by assuming the existence of non nucleon degrees of freedom in the nucleus. Now imagine that the nucleus is formed with nucleon cores, corresponding to the valence quark contents of the nucleons, surrounded by meson clouds. It is conceivable that the probability of a core, whose constituents are separated by large distances, being knocked out without causing serious disturbance to the nucleus (producing extra particles or breaking the nucleus), is smaller than that of a core whose constituents are close together, because the latter is in a more color neutral state, causing weaker disturbances when ejected. This means that the large distance components will be suppressed in the hard scattering process, causing the apparent enhancement of the large momentum part in the spectrum. If this is true (that is, the tail is really as high as what was observed.) then the transparency could be considerably higher than what is reported here.

Accurate measurement of the tail of the nucleon spectral functions is a very interesting subject. It was pointed out (Bro 1989) that the shape of the tail distribution is known from the general scaling

argument assuming that the high momentum tail can be attributed to the two nucleon correlations. As was pointed out in section 2.1, the probability of having n constituents confined to a region with sizes given by $1/\sqrt{t}$ is $t^{-(n-1)}$. A two nucleon system has 6 constituents.

Thus, the spectrum of a two nucleon cluster should be of the form of

$(\frac{1}{2})^5$, where p_t is the transverse Fermi momentum. This says that
 p_t

beginning somewhere in the tail the spectrum will become a power function of the transverse components of the Fermi momentum. Even though the statistics of the data do not allow for an accurate determination of the shape of the tail, this experiment is, however, the first one that measured the spectral functions with high energy quasi elastic hadron proton scattering. The existence of the tail is quite clear, even though the origin of the large size may be arguable. High energy hadrons are ideal for probing the tail because the incoming small hadrons can probe an ever smaller space where the target protons carry unusually large momentum.

Final comments

It has been demonstrated in E834 that quasi elastic scattering off nuclear targets at momentum transfers up to 12 Gev^2 can be measured. The transparencies of Li, C, Al, Cu and Pb targets to hard scattered protons and pions were measured at 6 and 10 Gev incident energies and those of Al and C targets to hard scattered protons were also measured at 12 Gev. The results seem to agree with what is predicted by the small hadron scattering model in going from 6 to 10 Gev, namely, the transparency increases with the energy. However, the drop off of the transparency at 12 Gev, clearly seen in aluminum, can not be explained by this model alone. Some newly developed models, which account for the structure of the observed transparencies well, were discussed. Assuming that the observed event distributions can be expressed as free particle scattering cross sections modulated by nucleon intrinsic momentum distributions and the transparencies, the spectral functions for the afore mentioned targets were deduced. The most important feature of the observed spectral functions is the apparent enhancement in the high momentum tails which is about 20% or more, depending on the target, higher than what is predicted by the Moniz model. Possible explanations for the apparent enhancement were discussed.

The overall uncertainty of the transparency measurements was about 30% to 40%. The main uncertainty was due to the uncertainties in the spectral functions.

The experiment can probably be improved in two ways: improve the statistics and improve the background rejection. The most important improvement can probably be made by making better measurements of the spectral functions. One way of achieving this is by going to lower energies, say about 5 Gev or so, and making high statistics measurements. For example, one can measure the transparency around 5 Gev in two ways: using the Fermi smearing as we did here, and varying the beam energy through the same region, selecting only the events in the narrow central region of the Fermi momentum. The ratio of the two is the spectral function. In this way the cross section factors and some of the systematic errors cancel out. Thus, one should have a more accurate measurement of the spectral functions. The signal to background ratio can be improved by measuring the momenta of both particles, or by building a better veto system to catch the π^{\pm} 's. For example, one can build a fine segmented veto package behind the side arm. This, in principle, should reduce the background by about 50%. Other technical improvements, such as improving the detector to handle further higher flux, will also be very important. It would also be very useful to understanding the systematic errors to measure the transparency of deuterium.

Hopefully systematic measurement of the transparencies at different energies and different momentum transfers, up to highest energies possible, will provide us with more information on the structure of the short distance hadronic interactions. In addition more accurate measurement on the pion transparency would also be very useful in helping us to understand the expansion mechanism, which hopefully will provide us with more information on the evolution of the short distance hadronic wave functions.

The experiment was first of its kind. Hopefully it will provide enough excitement to spur more of these type of experiments. Some day tests on Quantum Chromodynamics will be as mature as that of Quantum Electrodynamics.

Appendices

Appendix 1 Perturbation theory in the infinite momentum frame (IMF)

In order to probe the internal motions of a composite system of elementary quanta such as a hadron, which moves with a speed of light, the time scale of the probe has to be much smaller than those characteristic of the internal motions. This is not possible for a normal hadron. However, if we boost the reference frame with a speed of light, the dilation factor of time could be as large as one likes, thus rendering the detailed prob possible. This is one of the main reasons that the perturbation theory in the infinite momentum frame (IMF), or it's equivalent, the light cone quantum theory was introduced. Furthermore, if the time dilation factor is large enough the internal motions appear like non relativistic particles. When used in a bound system the light cone quantization has many advantages over the conventional equal time quantization theory. Most of all, it is not possible, in general, to represent a bound system with a single wave function in relativistic quantum field theory because the number of constituents is indefinite due to vacuum fluctuations by which new quanta can be created and existent quanta can be destroyed. In the light cone quantization the vacuum is an eigenstate of the Hamitonian. Physical states can be represented by Fock space column vectors so the cross sections are naturally expressed in terms of the light cone wave

functions. This is extremely useful at short distances because there the space time structure is clear and approximations for the wave functions can be inferred from information from particle interactions at lower energies. Another advantage of the light cone quantization is that the intermediate states are on mass shell so the physical picture of a process is straightforward. Properties such as unitarity are directly visible. In the following we will outline the procedures of the light cone quantization and the Feynman rules for QCD. To be specific let's consider a composite system of n quanta. Let the system moving in the positive z direction with a total momentum p which approaches infinity. Denote the fraction of the longitudinal momentum carried by each quantum by x_i and the transverse momentum by k_i . We have from momentum conservation:

$$\sum x_i = 1. \quad \sum k_i = 0 \quad (\text{A.1})$$

Define new time and energy by

$$\tau = t+z \quad (\text{A.2})$$

$$E = E + P_z \quad (\text{A.3})$$

$$H = E - P_z$$

$$\begin{aligned} &= \sqrt{m^2 + k^2 + P_z^2} - P_z \\ &= P_z \left(1 + \frac{m^2 + k^2}{P_z^2} \right) - P_z \\ &= \frac{m^2 + k^2}{2P_z} \end{aligned} \tag{A.4}$$

where τ is the new time called light cone time because $\tau = \text{const}$ corresponds to different points on the light cone in the usual four dimension coordinate system and H is the energy associated with the transverse motion. The Schödinger equation becomes:

$$i \frac{\partial}{\partial \tau} \Psi = H \Psi \tag{A.5}$$

where Ψ describes the state of the system at equal time $\tau = t + z$.

The procedures in going from the equation of motion to perturbative expansion of the transition amplitude parallel the conventional quantum field theories with one difference, i.e., instead of taking time-ordered operator product we now take τ -ordered products.

It has been shown that the time-ordered perturbation expansion in IMF, or its equivalent, light cone quantization is equivalent to the conventional quantum theory. (ref. 9 in Bro Quantum electrodynamics paper). Renormalization scheme has been developed and their applications to physical problems have been demonstrated. The Feynman rules for QCD are:

1) Draw all the time ordered diagrams with $x > 0$. that corresponding to a given process. Assign a momentum k_μ to each line such that (a) x are conserved at each vertex (b) $k^2 = m^2$, i.e., k_μ is on mass shell

2) Include a factor $\theta(x)$ for each line-all quanta are forward moving, i.e. P_z are positive in IMF.

3) For each vector boson line include a polarization sum $d_{\mu\nu}/x$ where $d_{\mu\nu}$ is gauge dependent. In Feynman gauge $d_{\mu\nu} = -g_{\mu\nu}$ while in light cone gauge which is defined as $\eta \cdot A = A^+ = 0$

$$d_{\mu\nu} = \sum_{\lambda=1,2} \epsilon_\mu(k,\lambda) \epsilon_\nu(k,\lambda)$$

$$= -g_{\mu\nu} + \frac{\eta_\mu k_\nu + \eta_\nu k_\mu}{\eta \cdot k}$$

4) The gluon-fermion vertices are

$$e_0 \frac{\bar{u}(k)}{(k^+)^{1/2}} \gamma^\mu \frac{\bar{u}(1)}{(1^+)^{1/2}}, \quad e_0 \frac{\bar{u}(k)}{(k^+)^{1/2}} \gamma^\mu \frac{\bar{v}(1)}{(1^+)^{1/2}},$$

$$-e_0 \frac{\bar{v}(k)}{(k^+)^{1/2}} \gamma^\mu \frac{\bar{u}(1)}{(1^+)^{1/2}}, \quad e_0 \frac{\bar{v}(k)}{(k^+)^{1/2}} \gamma^\mu \frac{\bar{v}(1)}{(1^+)^{1/2}}$$

The factors $1/(k^+)^{1/2}$, $1/(1^+)^{1/2}$ are omitted for external fermions in a scattering amplitude.

5) The trigluon vertex is

$$-e_0 [(p-q)^\mu g^{\mu\nu} + (q-p)^\nu g^{\mu\nu}]$$

and the four gluon vertex is

$$e_0^2 (g^{\mu\rho} g^{\nu\sigma} - g^{\mu\sigma} g^{\nu\rho})$$

6) for each intermediate state there is a factor

$$\frac{1}{\sum_{\text{inc}} k^- - \sum_{\text{int}} k^- + i\epsilon}$$

where the summations in the "energy denominator" are over the light-cone "energies" k^- of the incident and intermediate particles.

7) In Feynman gauge ghost loops occur. for each ghost line include a factor $-\theta(k^+)/k^+$. The gluon-ghost vertex is $e_0 k^\nu$. There are no ghost lines in light-cone gauge.

8) The fermion propagator has an instantaneous part $[\gamma^+/2k^+]$, as does the gluon propagator $[\eta^\mu \eta^\nu / k^{+2}]$. The ghost propagator can be absorbed into the regular propagator by replacing k , the momentum associated with the line by

$$\bar{k} = (k^+, \sum_{inc} k^-, \sum'_{int} k^-, k)$$

in the numerator for the diagrams in which the fermion, gluon and ghost propagates only over a single time interval. The summation over the intermediate state exclude the particle of interest. Thus in light-cone gauge, \bar{k} replaces k in the polarization summation $d_{\mu\nu}(k)$, as well as in the tri-gluon coupling for the gluons that appear in single intermediate state. Similarly, $\sum_{spins} u(k)\bar{u}(k)$ is replaced by $\bar{k} + m$ and

$$\sum_{spins} v(k)\bar{v}(k) \text{ by } \bar{k} - m.$$

- 9) Integrate $\int_0 dk^+ \int dk^2 / 16\pi^3$ over each independent k and sum over internal spins and polarizations.
- 10) color factors are computed in the same way as for covariant diagrams.

Appendix 2 The Monte Carlo simulations

Monte Carlo simulations were used quite extensively in the off line analysis for E834 including: the spectrum simulation in which the measured hadron proton cross section modulated by the model Fermi distribution was generated to derive the correction factors for the transparency; the inclusive background simulation in which the dominant background process $pp \rightarrow p\Delta$ was generated and traced through the detector to investigate the nature and the extent of the bias as a result of the incomplete coverage of the veto counters; and the simulation of the absorptions by the nuclear media to obtain the A dependence of the transparency. In this appendix we will describe the procedures that the Monte Carlo simulations were done in some detail.

A.2.1 The cross section simulation

The transparency was related to the cross section and the Fermi distribution by:

$$T(s) \int dp_f f(p) (dN/dt) \frac{(d\sigma/dt)_H [s]}{H(d\sigma/dt)_H [s_0]} = \epsilon \frac{n_H}{n_N} \int dp_f f(p_f) (dN/dt)_N [s] \quad (A.6)$$

To derive the correction factor we need to integrate the expression over the p_{fz} interval for which the transparency was to be calculated, and the p_{fx} and p_{fy} intervals in accordance with the cuts imposed on the real data in the event selection. From the operational point of view what we need to do is to compute the integral

$$I = \int_a^b y dp_{fy} \int_a^b x dp_{fx} \int_a^b z dp_{fz} f(p_f) \frac{d\sigma/dt[s]}{d\sigma/dt [s_0]} \quad (A.7)$$

with Monte Carlo simulations. In this way the effects of the detector can be included automatically. To simplify the simulation, only the power function factor of the cross section was included in the Monte Carlo generations. Furthermore, as we have pointed out earlier that the tail affects only the overall normalizations of the transparency from the way the events were counted, only the central region of the spectrum was simulated. A commonly used procedure, called rejection method, was used in the Monte Carlo generation because of the complexity of the functions. At each incident energy and for each target the maximum and the minimum probabilities corresponding to $p_{fz} = k_f$ and $p_{fz} = -k_f$ respectively were first calculated. Let the interval be $P_0 = P_{ma} - P_{mi}$. Points (p_{fx}, p_{fy}, p_{fz}) in the Fermi sphere were then randomly selected such that $\sqrt{(p_{fx}^2 + p_{fy}^2 + p_{fz}^2)} \leq k_f$ where k_f is the

Fermi momentum for the medium. The probability P that corresponds to the momentum selected was calculated and the ratio $r = (P - P_{mi}) / P_0$ was then compared with a randomly drawn number r' . If $r < r'$ the point was kept, otherwise it was rejected.

Let the total number of event generated without the cross section factor be N_0 , the number of event fallen into the concerned region, generated with the cross section factor, be N . Then,

$$N = \int_a^b f(p) \frac{d\sigma}{dt}(s) / \frac{d\sigma}{dt}(s_0) dp \quad (\text{A.8})$$

$$N_0 = \int_{\text{vol}} f(p) dp \quad (\text{A.9})$$

and we then have:

$$\gamma = \frac{N}{N_0} \quad (\text{A.10})$$

A.2.2 The simulation of background process $pp \rightarrow p\Delta$

The dominant background process in the pp elastic scattering is probably $pp \rightarrow p\Delta$ where $\Delta \rightarrow p\pi^0$ and the photons from the π^0 decay escaped from the detector. Because of the limited solid angle coverage it is possible that bias be introduced in the event identifications. For example, π^0 's produced almost colinearly with the protons from the Δ decay are more likely to escape from the veto counters than those produced at large angles. Thus, there could be enhancement to the fake elastic events in the central region because the small opening angle decay of the Δ will most likely produce fake events with small Fermi momentum. The steps that the events are generated are as follows: first a two body interaction $pp \rightarrow p\Delta$ was generated isotropically in the center of mass frame of the incoming and the target protons. The target proton was required to carry a Fermi momentum randomly selected from the available phase space. Next the Δ was allowed to decay isotropically in its rest frame immediately, followed by an isotropic decay of the π^0 in its rest frame. The photons were then traced through the detector. The conversion efficiency of the veto counter was assumed to be 1, which should be a pretty good approximation since there is no reason to believe that the inefficiencies should produce bias in whatever way. The results was shown in fig. 5.10. We note that there is no appreciable bias from the veto counters.

A.2.3 The simulations of the absorptions by the nuclear matter

To simulate the nuclear absorptions we consider a process where the incoming proton interacts with one of the protons inside the target nucleus randomly chosen. The incoming momentum was assumed to be along the z direction, the scattering angle was assumed to be 90 degrees in the CMS frame, and the azimuthal angle was chosen at random. For convenience let me write down the definition of the transparency again:

$$\frac{A_{\text{eff}}}{A} = \frac{1}{A} \int dr \rho_A(r) P_1(p_1, r) P_2(p_2, r) P_3(p_3, r) \quad (\text{A.11})$$

where P_i 's is the probability that proton i, carrying momentum p_i , travel through the nucleus without suffering an inelastic interaction, starting at point r inside the nucleus.

$$P_i(p_i, r) = \exp\left(-\int_s dz \sigma^{\text{eff}}(p_i, z) \rho_A(z)\right) \quad (\text{A.12})$$

$$\sigma_h^{\text{eff}} = \sigma_{hN}^{\text{tot}} \left(\left[\left(\frac{z}{l_h}\right)^\Delta + \frac{\langle n^2 k^2 \rangle}{t} \left(1 - \left(\frac{z}{l_h}\right)^\tau\right) \right] \theta(l_h - z) - \theta(z - l_h) \right) \quad (\text{A.13})$$

Choose the frame in which the nucleus is at rest. Let the center of the nucleus be the origin and the beam direction be positive z axis.

The simulation begins with the selection of the interaction point C inside the nucleus. Each of the three protons has a probability P_i going out of the nucleus so the total number of proton that contribute to the elastic scattering at C within a volume dv is :

$$dA_{\text{eff}} = P_1(p_1, r_c) P_2(p_2, r_c) P_3(p_3, r_c) \rho_A(r_c) dv \quad (\text{A.14})$$

where r_c is position vector of point C, p_1 is the incoming momentum, p_2 and p_3 are the momenta of the outgoing protons. Using the universally accepted nuclear density distribution Wood-Saxon formula

$$\rho(r) = \frac{c}{1 + e^{-(r-R)/b}} \quad (\text{A.15})$$

where $R = 1.1 \cdot A^{1/3}$ fm

$$b = 0.57 \text{ fm}$$

c is a normalization constant such that $\int dv \rho_A(r) = A$ within the nuclear volume. In the simulation nucleus volume was cut off at a maximum radius $r_m = 3R$ and normalization was taken care of by choosing c appropriately. r_m was then divided into N equal intervals $dr = r_m/N$.

Points within the shell were selected by choosing the angular coordinates randomly. The initial and final state protons were then traced through the nuclear volume. It is clear that the transparency depends on the polar angle of the interaction point within each shell. Therefore, multi points were generated within each shell and the resulted transparencies were averaged.

Let the interaction point be C (x,y,z) in the nucleus frame. For convenience we defined a new frame in which C is the origin and the three axes are parallel to the axes of the nucleus frame. We are now ready to trace the particles. Start with the incoming proton. Let the coordinates of a point D on the particle path in the new frame be (0,0,z'). The probability that the incoming proton survived after traveling a infinitesimal distance from D is then:

$$\begin{aligned} P(z') &= P(z) \exp(-dz \rho_A(r(z)) \sigma^{\text{eff}}(z)) \\ &= P(z) (1 - dz \rho_A(r(z)) \sigma^{\text{eff}}(z)) \end{aligned} \quad (\text{A.16})$$

where z is the z coordinate in the new frame, i.e., the distance the incoming proton traveled after the hard collision, and r is the radial coordinate in the nucleus frame. σ^{eff} is given by the expansion model eq. A.13, and $\sigma_{\text{pN}}^{\text{tot}} = 40 \text{ mb.}$

For simplicity we consider only 90 degree scattering in the center of mass frame so the outgoing protons are symmetric with respect to the beam axis. The azimuthal angles in the new frame were randomly chosen. Similarly to the incoming proton, at point $E(x',y',z')$ the probability that say, particle 2 survives after traveling a distance ds from E is:

$$\begin{aligned}
 P(x'+dx',y'+dy',z'+dz') & \\
 &= P(x',y',z',) \exp(-ds\rho_A(r(x',y',z'))\sigma^{\text{eff}}(x',y',z')) \\
 &= P(x',y',z')(1-ds\rho_A(r)\sigma^{\text{eff}}(x',y',z')) \quad (\text{A.17})
 \end{aligned}$$

where s is the distance from the point of collision and r is the distance from the origin in the nucleus frame,

$$s = \sqrt{(x')^2 + (y')^2 + (z')^2} \quad (\text{A.18})$$

$$r = \sqrt{((x+x')^2 + (y+y')^2 + (z+z')^2)} \quad (\text{A.19})$$

The effective cross section is again given by the expansion model with z replaced by s . The tracing continues until $r \geq r_m$, i.e., until the particles are all outside the nucleus. The transparency is then simply the sum over all shells, divided by A , the mass number of the nucleus concerned.

Bibliography

- [Bal 1987] B. Baller, Ph. D. Thesis, University of Minnesota (1987).
- [Bal 1988] B. Baller et al., Phys. Rev. Lett. 60, 1118 (1988).
- [Bla 1985] J. Blazey et al., Phys. Rev. Lett. 55, 1820 (1985).
- [Bla 1986] J. Blazey, Ph. D. Thesis, University of Minnesota (1986).
- [Bod 1981] A. Bodek and J.L. Ritchie, Phys. Rev. D23, 1070 (1981).
- [Bro 1973] S.J. Brodsky, G.R. Farrar, Phys. Rev. Lett. 31, 1153
(1973).
- [Bro 1975] S.J. Brodsky, G. R. Farrar, Phys. Rev. D11, 1309 (1975).
- [Bro 1981] S.J. Brodsky and G.P. Lepage, Phys. Rev. D24, 1808 (1981).
- [Bro 1987] S.J. Brodsky, SLAC publication SLAC-PUB-4387 (1987).
- [Bro 1988] S.J. Brodsky and G.F. de Teramond, Phys. Rev. Lett. 60,
1924 (1988).
- [Bro 1989] S.J. Brodsky, Private communication (1989).
- [Car 1988] A.C. Carroll et al., Phys. Rev. Lett. 61, 1698 (1988).
- [Far 1984] G.R. Farrar, Phys. Rev. Lett. 53, 298 (1984).
- [Far 1988] G.R. Farrar et al., Rutgers University Preprint RU-88-03
(1988).
- [Fis 1973] P. Fishbane and C. Quigg, Nucl. Phys. B61, 469 (1973).
- [Fra 1980] L.L. Frankfurt and M.I. Strikman, Phys. Lett. 94B, 216
(1980).
- [Fra 1988] L.L. Frankfurt and M.I. Strikman, Phys. Report 160, 236
(1988).

- [Fru 1984] S. Frullani and J. Mougey, Advances in Nuclear Physics, eds. J.W. Negele and F. Vogt, Plenum Press, New York and London, Vol. 14 (1984).
- [Gun 1973] J. Gunion et al., Phys. Rev. D8, 287 (1973).
- [Hep 1985] S. Heppelman et al., Phys. Rev. Lett. 55, 1824 (1985).
- [Isg 1984] N. Isgur and C.H. Llewellyn Smith, Phys. Rev. Lett. 52, 1080 (1984).
- [Jac 1986] O.C. Jacob and L.S. Kisslinger, Phys. Rev. Lett. 56, 225 (1986).
- [Jen 1980] K. A. Jenkins et al., Phys. Rev. D21, 2445 (1980)
- [Lan 1974] V. Landshoff, Phys. Rev. D10, 1024 (1974).
- [Lep 1980] G.P. Lepage and S.J. Brodsky, Phys. Rev. D22, 2157 (1980).
- [Mat 1973] V. Matveev et al., Lett. Nuovo Cimento 5, 719 (1973).
- [Mue 1981] A.H. Mueller, Phys. Report 73, 237 (1981).
- [Mue 1982] A.H. Mueller, Proceedings of the XVII Recontre de Moriond, eds. J. Tran Thah Van, Editions Frontieres, Gif-sur-Yvette, France (1982).
- [Pir 1983] B. Pire and J. Ralston, Proceedings of High Energy Spin Physic-1982, eds. G. Bunce, AIP Conference Proceedings No. 95, 347 (AIP, New York 1983).
- [Pir 1982] B. Pire and J. Ralston, Phys. Lett. 117B, 233 (1982).
- [Ral 1988] J. Ralston and B. Pire, Phys. Rev. Lett. 61, 1823 (1988).
- [Wah 1985] D.S. Wahl, Ph. D. Thesis, University of Minnesota (1985).